



**HAL**  
open science

# Revisiting deflagration-to-detonation transition in the context of carbon-free energy

Hassan Tofaili

► **To cite this version:**

Hassan Tofaili. Revisiting deflagration-to-detonation transition in the context of carbon-free energy. Fluid mechanics [physics.class-ph]. Normandie Université, 2022. English. NNT : 2022NORMIR28 . tel-04050689

**HAL Id: tel-04050689**

**<https://theses.hal.science/tel-04050689>**

Submitted on 29 Mar 2023

**HAL** is a multi-disciplinary open access archive for the deposit and dissemination of scientific research documents, whether they are published or not. The documents may come from teaching and research institutions in France or abroad, or from public or private research centers.

L'archive ouverte pluridisciplinaire **HAL**, est destinée au dépôt et à la diffusion de documents scientifiques de niveau recherche, publiés ou non, émanant des établissements d'enseignement et de recherche français ou étrangers, des laboratoires publics ou privés.



Normandie Université

## THÈSE

**Pour obtenir le diplôme de doctorat**

**Spécialité Energétique**

**Préparée à l'INSA de Rouen Normandie**

### REVISITING DEFLAGRATION-TO-DETONATION TRANSITION IN THE CONTEXT OF CARBON-FREE ENERGY

présentée et soutenue par

**HASSAN TOFAILI**

**Thèse soutenue publiquement le 29 Novembre 2022  
devant le jury composé de**

B. DENET	Professeur à l'Université d'Aix-Marseille	Rapporteur
J. MELGUIZO-GAVILANES	Chargé de Recherche CNRS	Rapporteur
L. GLANGETAS	Professeur à l'Université de Rouen Normandie	Examineur
K. TRUFFIN	Dr. Ing. Chercheuse à IFPEN - Chef de Projet	Examinatrice
P. CLAVIN	Professeur Emerite à l'Université d'Aix-Marseille	Invité
G. LODATO	Maître de Conférence à l'INSA Rouen Normandie	Co-encadrant
L. VERVISCH	Professeur à l'INSA Rouen Normandie	Directeur de thèse

■ Thèse dirigée par Luc VERVISCH et Guido LODATO, laboratoire CORIA (UMR 6614 CNRS)





# Abstract

With the transition to carbon-free fuels such as hydrogen, new challenges arise relating to the safe storage and transportation as well as efficient combustion of these fuels. These challenges can be better addressed by improving our understanding of the fundamental physical mechanisms controlling the dynamics of relevant combustion waves as well as the complex phenomenon of deflagration-to-detonation transition (DDT) of hydrogen-air mixtures. This thesis represents a contribution in addressing two pertinent problems in the combustion of energetic hydrogen-air mixtures. The first problem addressed concerns the driving mechanisms for the instability of detonation waves, which is a matter of interest in a number of industrial applications. The theoretical model suggested by Clavin and Williams (2002), which explains the one-dimensional instability of gaseous detonations as a result of the interaction of acoustic and entropy waves travelling between the leading shock and the reaction zone, is revisited and studied analytically in the asymptotic limit of low heat release, where an integral equation describing oscillations in shock velocity is obtained. The theoretical findings are validated against a set of high-order direct numerical simulations carried out in the same asymptotic limit, and the results show a good agreement between the theory and the numerics, thus validating the Clavin-Williams model. The second problem addressed is the deflagration-to-detonation transition of an elongated laminar flame, which might be relevant to the understanding of the super-knock effect in hydrogen-fuel engines, and to the DDT of energetic cellular flames. A new theoretical model is proposed to explain this DDT phenomenon, which involves a double-feedback mechanism driving the flame acceleration. The two elements constituting the double-feedback mechanism are the heating of the fresh gas by compression waves propagating upstream of the flame, which increases the laminar flame speed, and the back-flow of burnt gas from the lateral wings of the flame towards the flame tip. We demonstrate that these two effects accelerate the flame tip, finally leading to a singularity of flame acceleration and the development of a shock wave on the flame tip, which causes the transition to a detonation.

# Resumé

Avec la transition vers des carburants sans carbone tels que l'hydrogène, de nouveaux défis se posent concernant le stockage et le transport sûrs ainsi que la combustion efficace de ces carburants. Ces défis peuvent être mieux relevés en améliorant notre compréhension des mécanismes physiques fondamentaux contrôlant la dynamique des ondes de combustion pertinentes ainsi que le phénomène complexe de transition déflagration-détonation (DDT) des mélanges hydrogène-air. Cette thèse représente une contribution à la résolution de deux problèmes pertinents dans la combustion de mélanges énergétiques hydrogène-air. Le premier problème abordé concerne les mécanismes moteurs de l'instabilité des ondes de détonation, qui intéressent de nombreuses applications industrielles. Le modèle théorique proposé par Clavin et Williams (2002), qui explique l'instabilité unidimensionnelle des détonations gazeuses à la suite de l'interaction des ondes acoustiques et d'entropie se déplaçant entre le choc en amont et la zone de réaction, est revisité et étudié analytiquement dans la limite asymptotique de faible dégagement de chaleur, où une équation intégrale décrivant les oscillations de la vitesse de choc est obtenue. Ces résultats théoriques sont validés par un ensemble de simulations numériques directes d'ordre élevé réalisées dans la même limite asymptotique. Les résultats montrent un bon accord entre la théorie et les numériques, validant ainsi le modèle de Clavin-Williams. Le deuxième problème abordé est la transition déflagration-détonation d'une flamme laminaire allongée, qui pourrait être pertinente pour la compréhension de l'effet de super-cliquetis dans les moteurs à hydrogène et pour le DDT des flammes cellulaires énergétiques. Un nouveau modèle théorique est proposé pour expliquer ce phénomène DDT, qui implique un mécanisme à double rétroaction pilotant l'accélération de la flamme. Les deux éléments constitutifs du mécanisme à double rétroaction sont le chauffage des gaz frais par ondes de compression en amont de la flamme, ce qui augmente la vitesse laminaire de la flamme, et le reflux des gaz brûlés des ailes latérales de la flamme vers le bout de flamme. Nous démontrons que ces deux effets accélèrent le bout de flamme, conduisant finalement à une singularité d'accélération de flamme et au développement d'une onde de choc sur le bout de flamme, qui provoque le passage à une détonation.



# Acknowledgment

First of all, I would like to express my gratitude to my thesis advisors prof. Luc Vervisch and Guido Lodato, for their continuous help and support throughout my work on this thesis. I would also like to extend my thanks to prof. Paul Clavin for his continuous guidance and all the enlightening discussions he provided during this research work.

I am also grateful to all the jury members of my thesis: Bruno Denet, Josue Melguizo-Gavilanes, Leo Glangetas, and Karine Truffin for having accepted to take the time to evaluate this work.

I would also like to thank my colleagues at INSA for the great memories and the good company they provided over the last three years: Cleante, Huu-Tri, les Florians, Emilie, Louis, Niccolo and everyone else, and also my colleague from Marseille, Raul.

Finally, I should express my very profound gratitude to my parents and to my siblings for providing me with unfailing support and continuous encouragement throughout my years of study at home and abroad.

This little accomplishment would not have been possible without them. Thank you.

Hassan Tofaili

*To go beyond all knowledge is to find  
That comprehension which eludes the mind,  
And you can never gain the longed-for goal  
Until you first outsoar both flesh and soul*

— Attar,  
*The moths and the flame*

# Contents

<b>1</b>	<b>Introduction</b>	<b>15</b>
1.1	Motivation . . . . .	15
1.2	Objectives . . . . .	17
1.2.1	One-dimensional dynamics of detonations . . . . .	17
1.2.2	Deflagration-to-detonation transition . . . . .	17
1.2.3	High-order numerical methods . . . . .	18
<b>2</b>	<b>Detonation and deflagration waves</b>	<b>21</b>
2.1	Phenomenological description of 1D deflagrations and detonations . . . . .	21
2.1.1	Detonation wave . . . . .	21
2.1.2	Deflagration wave . . . . .	23
2.2	Gasdynamic theory of steady combustion waves . . . . .	23
2.2.1	The Navier-Stokes equations . . . . .	23
2.2.2	The Rayleigh line and the Hugoniot curve . . . . .	24
2.2.3	Rankine-Hugoniot relations . . . . .	27
2.2.4	The Chapman-Jouguet criterion and the ZND detonation structure . . . . .	28
2.3	The ZFK flame theory . . . . .	30
2.3.1	Problem formulation . . . . .	30
2.3.2	The reaction rate . . . . .	32
2.3.3	Solution for unity Lewis number . . . . .	34
2.3.4	Solution for non-unity Lewis number . . . . .	37
<b>3</b>	<b>The spectral difference method</b>	<b>40</b>
3.1	The one-dimensional spectral difference scheme . . . . .	40
3.1.1	Interpolation inside the element . . . . .	41
3.1.2	The Riemann solver of Roe . . . . .	43
3.1.2.1	Calculation of $\tilde{\mathbf{A}}$ . . . . .	44
3.1.2.2	Calculation of the intermediate flux . . . . .	46
3.1.3	Time marching . . . . .	46
3.1.4	Shock capturing . . . . .	47
3.1.5	Scalar limiter . . . . .	49
3.2	Moving reference frame . . . . .	49
3.2.1	Conservation equations . . . . .	50
3.2.2	Modification to the Roe solver . . . . .	51
3.2.3	Boundary conditions on the moving piston . . . . .	52

---

3.3	Flame stabilization . . . . .	53
<b>4</b>	<b>One-dimensional dynamics of gaseous detonations</b>	<b>56</b>
4.1	Introduction . . . . .	56
4.2	Flow configuration and theoretical formulation . . . . .	62
4.2.1	Primitive balance equations . . . . .	62
4.2.2	Characteristic equations in the moving frame . . . . .	63
4.3	Asymptotic analysis . . . . .	64
4.3.1	Asymptotic limit and the two-timescale dynamics . . . . .	65
4.3.2	Unsteady distribution of heat release and scaling law . . . . .	66
4.3.3	Integral equation . . . . .	68
4.3.4	Instability threshold for the scaling law . . . . .	70
4.4	Framework for the parametric analysis . . . . .	71
4.4.1	Model of reaction rate . . . . .	71
4.4.2	Parameters formulation . . . . .	72
4.5	Numerical analysis . . . . .	73
4.5.1	Problem formulation . . . . .	73
4.5.2	Numerical implementation . . . . .	74
4.5.2.1	Measurement of $T_N$ . . . . .	74
4.5.3	Steady CJ detonation . . . . .	74
4.6	Comparison of theory against simulations . . . . .	75
4.7	Conclusion . . . . .	78
<b>5</b>	<b>Deflagration-to-detonation transition at the tip of an elongated flame</b>	<b>82</b>
5.1	Introduction . . . . .	82
5.2	Piston model for the back-flow of burned gas . . . . .	84
5.2.1	Self-accelerating flame . . . . .	84
5.2.2	Thermal sensitivity of the flame speed in very energetic mixtures . . . . .	87
5.3	Self-similar solutions . . . . .	89
5.3.1	Quasi-steady approximation and nonlinear equation . . . . .	89
5.3.2	Solution of the piston model using the DJ approximation . . . . .	89
5.3.3	Critical condition for very energetic elongated flames . . . . .	91
5.4	Comparison with the experimental data . . . . .	92
5.5	Finite-time singularity . . . . .	93
5.6	Beyond self-similarity: formation of a shock on the flame front . . . . .	94
5.6.1	Theoretical analysis . . . . .	95
5.6.2	Numerical validation . . . . .	98
5.7	Conclusion . . . . .	98
<b>6</b>	<b>Conclusions and perspectives</b>	<b>102</b>
6.1	One-dimensional dynamics of detonations . . . . .	102
6.2	Deflagration-to-detonation transition of an elongated flame . . . . .	103
	<b>Bibliography</b>	<b>106</b>
	<b>French summary</b>	<b>113</b>

# Nomenclature

## Abbreviations

Symbol	Description
AV	artificial viscosity
CFL	Courant-Friedrichs-Lewy
CJ	Chapman-Jouguet
CS	Clanet and Searby
DDT	deflagration-to-detonation transition
DJ	Deshaies and Joulin
DNS	direct numerical simulation
RK45-SSP	fourth-order, five-stages, strong-stability-preserving Runge-Kutta method
SD	spectral difference
ZFK	Zel'dovich-Frank Kamenetskii
ZND	Zel'dovich, von Neumann and Döring

## Roman letters

Symbol	Description	Unit
$A$	flux Jacobian	multiple
$\tilde{A}$	Roe's approximate flux Jacobian	multiple
$a$	speed of sound	$\text{m} \cdot \text{s}^{-1}$
$b$	Arrhenius pre-exponential factor	-
	reduced activation energy (Chapter 4)	-
$c$	reactant concentration	$\text{mol} \cdot \text{m}^{-3}$
$c_p$	specific heat capacity at constant pressure	$\text{J} \cdot \text{kg}^{-1} \cdot \text{K}^{-1}$
$c_v$	specific heat capacity at constant volume	$\text{J} \cdot \text{kg}^{-1} \cdot \text{K}^{-1}$
$D$	mass diffusivity	$\text{m}^2 \cdot \text{s}^{-1}$
$\mathcal{D}$	propagation speed of detonation wave	$\text{m} \cdot \text{s}^{-1}$
$d_L$	preheat zone thickness	m
$d_r$	reaction zone thickness	m

$E$	total energy per unit mass	$\text{J} \cdot \text{kg}^{-1}$
$E_a$	Arrhenius activation energy	J
$E_T$	induction-zone activation energy (Chapter 4)	J
$\mathbf{F}$	total flux vector	multiple
$\mathbf{F}_a$	advective flux vector	multiple
$\mathbf{F}_v$	viscous flux vector	multiple
$H$	total (stagnation) enthalpy per unit mass	$\text{J} \cdot \text{kg}^{-1}$
$h$	specific enthalpy	$\text{J} \cdot \text{kg}^{-1}$
$\mathbf{K}$	eigenvector of flux Jacobian	multiple
$\tilde{\mathbf{K}}$	eigenvector of Roe's approximate Jacobian	multiple
$k_B$	Boltzmann constant	$\text{J} \cdot \text{K}^{-1}$
$L$	Length of the elongated flame	m
$M$	Mach number of the combustion wave / shock wave	-
$M_r$	reactant molar mass	$\text{kg} \cdot \text{mol}^{-1}$
$m$	reduced flame speed (Chapter 5)	-
$n$	simulation order	-
$P_i$	$i$ -th degree Legendre polynomial	-
$P / p$	pressure	Pa
$Q$	reduced heat release	-
$q$	reduced heat release (Chapter 5)	-
$q_m$	total heat release per unit mass	$\text{J} \cdot \text{kg}^{-1}$
$R$	specific gas constant	$\text{J} \cdot \text{kg}^{-1} \cdot \text{K}^{-1}$
	tube radius (Chapter 5)	m
$\mathbf{S}$	source vector	multiple
$s$	specific entropy	$\text{J} \cdot \text{kg}^{-1} \cdot \text{K}^{-1}$
	instability growth rate (Chapter 4)	-
$s_e$	artificial viscosity sensor parameter	-
$T$	temperature	K
$t$	time	s
$t_{coll}$	elastic collision time scale	s
$t_e$	flame elongation time scale	s
$t_r$	reaction time scale	s
$\mathbf{U}$	vector of conservative variables	multiple
$U_f$	flame speed in lab frame (Chapter 5)	$\text{m} \cdot \text{s}^{-1}$
$u$	flow velocity	$\text{m} \cdot \text{s}^{-1}$
$v$	specific volume	$\text{m}^3 \cdot \text{kg}^{-1}$

$W$	reaction rate	$s^{-1}$
$w$	reduced reaction rate	-
$X_p$	piston position in lab frame	m
$x$	spatial coordinate	m
$Y$	reaction progress variable	-
$y$	reduced fresh gas temperature (Chapter 5)	-

## Greek letters

Symbol	Description	Unit
$\dot{\alpha}_\tau$	reduced shock velocity	-
$\beta$	Zel'dovich number	-
	reduced induction-zone activation energy (Chapter 4)	-
$\gamma$	ratio of specific heats	-
$\epsilon$	reduced heat release (Chapter 4)	-
$\varepsilon$	artificial viscosity	$m^2 \cdot s^{-1}$
$\zeta$	reduced spatial coordinate	-
$\theta$	reduced temperature	-
$\Lambda$	flame elongation parameter	-
$\lambda$	thermal conductivity	$W \cdot m^{-1} \cdot K^{-1}$
$\lambda_i$	eigenvector of the flux Jacobian	$m \cdot s^{-1}$
$\tilde{\lambda}_i$	eigenvector of Roe's approximate Jacobian	$m \cdot s^{-1}$
$\mu$	reduced mass flux / flow velocity	-
	dynamic viscosity (§2.2)	$Pa \cdot s$
$\nu$	reaction order	-
	non-dimensional flow velocity (§5.6)	-
$\xi$	reduced spatial coordinate	-
$\pi$	reduced pressure	-
$\rho$	density	$kg \cdot m^{-3}$
$\sigma$	flame elongation parameter	-
$\tau$	reduced time variable	-
$\tau_{coll}$	elastic collision timescale	s
$\tau_{ev}$	flame evolution time scale	s
$\tau_r$	reaction time scale	s
$\psi$	sensor variable	variable
$\omega$	reduced oscillation frequency	-

## Non-dimensional numbers

Symbol	Description
Le	Lewis number
Pr	Prandtl number
$\beta$	Zel'dovich number



# Chapter 1

## Introduction

### Sommaire

---

<b>1.1 Motivation</b> . . . . .	<b>15</b>
<b>1.2 Objectives</b> . . . . .	<b>17</b>
1.2.1 One-dimensional dynamics of detonations . . . . .	17
1.2.2 Deflagration-to-detonation transition . . . . .	17
1.2.3 High-order numerical methods . . . . .	18

---

In this introductory chapter, we introduce the motivations of the study and the challenges addressed in this work.

### 1.1 Motivation

Since it was first discovered by Berthelot and Vieille [1] back in 1883, the detonation phenomenon has been subject to extensive research encompassing experimental, theoretical and numerical studies (see [2,3] and references therein). These studies of detonations have been motivated by a large number of factors, ranging from the improvement of safety measures in fuel storage and transport facilities (Figure 1.1), to various industrial applications such as internal combustion engines [4–6] or rotating detonation engines [7–12], to some peculiar natural phenomena such as the explosions of stars (Figure 1.2).

Performing multiple and detailed experimental studies on such problems is often prohibitively expensive. Therefore, actual safety regulation, optimization and design mostly rely on global correlations and numerical simulations. To be relevant, such simulations should accurately describe the strongly transient behaviors characterizing the initiation and the propagation of detonation waves. However, because of the wide range of time and length scales involved, in both chemical kinetics and flow physics, actual computer capabilities do not allow, for complex practical systems, to precisely capture the unsteadiness of the inner structure of the wave together with the large scale flow motions. Since this inner structure actually controls the initiation and the dynamics of detonation waves at the largest flow scales, the prediction capabilities of the numerical simulations have stayed so far limited. Thus, there exists a need for new theoretical models of the dynamics of detonations, which include the effect of the inner structure of these waves, to assist numerical simulations.



Figure 1.1: Aftermath of the Buncefield fire that took place at a fuel storage facility in the UK in 2005. According to the final investigative report [13], the fire was started by a detonation of a gaseous fuel-air mixture in one of the tanks.

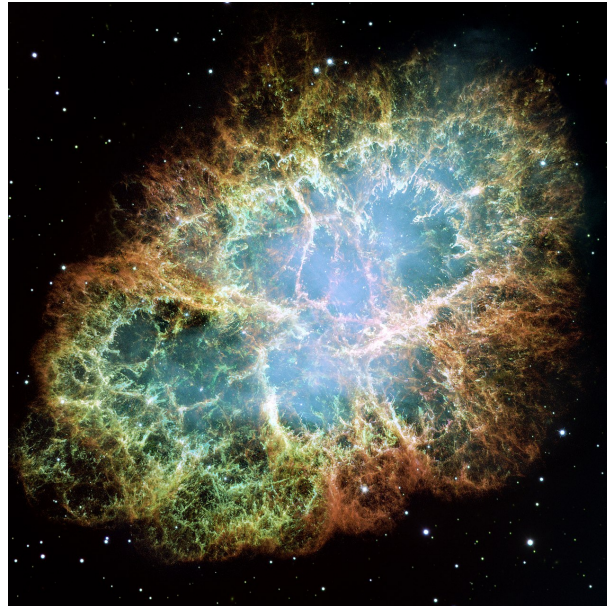


Figure 1.2: A picture mosaic of the Crab Nebula taken by the Hubble Space Telescope [14]. The nebula is the remnant of a supernova that was observed from Earth in the year 1054 A.D, as reported by Chinese astronomers and Arab chroniclers of the time. The mechanisms of deflagration-to-detonation transition of supernovae are still an active topic of research [15–17].

The objective of the present work is therefore to set up theoretical models by asymptotic analyses, representing accurately the dynamics of detonations in hydrogen-air mixtures. The mathematical formulation will be useful to guide in the physical analysis and shed more insight into the key parameters to better control carbon-free combustion systems and also improve safety regulation. The developed analytical models will be validated by carefully controlled direct numerical simulation (DNS) using the most advanced high-order algorithms. In the next section, we present a brief overview of the specific problems studied in this work and the approaches followed in the studies.

## 1.2 Objectives

Attention is focused on two main problems, which are the stability of one-dimensional detonations, and the deflagration-to-detonation transition (DDT) of laminar flames in tubes. In the following, we provide an introduction for the two problems studied, as well as a brief discussion of the use of high-order numerical methods.

### 1.2.1 One-dimensional dynamics of detonations

Since the 1960s, it's been known that the steady-state theory for the propagation of detonation waves, advanced by Zeldovich, von Neumann and Döring, does not provide an accurate description of real detonations, which are usually strongly unsteady, exhibiting longitudinal pulsations as well as transverse waves traveling across the detonation front [18, 19]. Despite many decades of research, the physical mechanisms driving detonation instabilities are still largely unknown. Studies based on linear stability analysis were performed to analyze detonation dynamics since the 1960s [20, 21], however, the mathematical complexity of these studies makes it difficult to observe the physical mechanisms at play.

A new trend that gained popularity in the last three decades in the study of this kind of problems is the use of asymptotic analysis [22–24]. In asymptotic analysis, the problem formulation is simplified systematically by taking extreme limiting values for some predetermined flow parameters. The purpose is to clarify the physics of the problem by retaining the key physical mechanisms at play, at the expense of others which are expected to be less influential.

In 2002, Clavin & Williams [23] presented an analytical study of the stability of one-dimensional detonations, in which they suggested that the instability of one-dimensional detonations is controlled by a positive feedback loop of acoustic and entropy waves traveling between the leading shock wave and the reaction zone. In Chapter 4, we revisit the Clavin & Williams analysis in the asymptotic limit of weak heat release and a ratio of specific heats close to unity, which allows us to simplify the problem and obtain an integral equation of the flow describing the detonation dynamics and instability. The results are compared against high-order spectral-difference numerical simulations performed in the same asymptotic limit and theory is validated.

### 1.2.2 Deflagration-to-detonation transition

Numerous mechanisms have been discussed in the literature to explain the transition between deflagration and detonation. However, despite many years of research, there is still no complete understanding of all possible DDT mechanisms [3, 25, 26]. In the context of a hydrogen-air mixture, possible DDT mechanisms include acceleration by turbulence [27], interaction of the flame with obstacles [28], the increase of the flame surface by intrinsic or thermo-acoustic instabilities and the so-called spontaneous Zeldovich ignition due to thermal gradients [29], specifically in boundary layers (see Clavin & Searby [3] for a recent review).

It is likely that a fundamental mechanism for DDT may be grounded in the analysis of Deshaies & Joulin (DJ) [27] concerning the self-similar solution constituted by the flame and the flame-driven precursor shock, both fronts propagating at constant velocity (subsonic for the flame and supersonic for the shock). An upper bound of the flame velocity corresponding to a turning point of the self-similar solution in the phase-space has been identified in [27]. The strongly nonlinear thermal dependence of the flame speed on the temperature of the fresh mixture, controlled by the strength of the precursor shock propagating upstream of the flame, is the key mechanism responsible for the existence of this turning

point associated to DDT. A limitation for the DJ analysis however was that it was only carried out in the limit of a weak leading shock, which doesn't correspond to realistic DDT phenomena. In Chapter 5, we revisit the DJ analysis applying it to an elongated laminar flame propagating from the closed end of a tube. We show that a self-similar solution exhibits a turning point for a moderate Mach number of the leading shock, leading to a divergence of the flame acceleration and the formation of a shock wave on the flame. This could lead to a DDT under conditions consistent with previous experiments and numerical simulations [30].

The findings presented in this part of the work provide a possible mechanism for the DDT of cellular flames in very energetic mixtures. In addition, they might provide a reliable criterion for the apparition of the undesirable super-knock in future engines powered by the combustion of hydrogen, and also more generic rules pertaining to safety issues.

### 1.2.3 High-order numerical methods

It is common place for researchers in industry and also in academia to use 2nd-order finite difference or finite volume methods in order to discretize the derivative terms in the Navier-Stokes equations [31] (Figure 1.3). Of these approaches, finite volume methods are the most popular, as they can be most conveniently implemented on the unstructured meshes which are frequently used in complex geometries for practical applications. The use of a 2nd-order formulation in conjunction with an appropriate numerical flux ensures a compact stencil in which the degrees of freedom in a cell are coupled to (at most) the degrees of freedom in the nearest neighboring cells. Moreover, 2nd-order methods produce a significant amount of numerical dissipation which tends to dampen out spurious oscillations in the solution, thereby enhancing the robustness of the method.

However, this robustness comes at the cost of accuracy. In particular, the excess dissipation tends to obscure physical features (sound waves, vortices, etc.) that are evolving in time, and as a result, 2nd-order methods are inefficient for obtaining solutions to unsteady problems with low-error tolerances. It has been shown that, as the error tolerance decreases, using a 2nd-order method with a finer grid becomes significantly more computationally expensive than using a high-order method (greater than 2nd-order) with a coarser grid [31]. Furthermore, it has been shown that, for the same number of degrees of freedom, a high-order method can sometimes achieve *super convergence*, thus leading to significantly lower errors. Although the increasing availability in computational power can permit a reduction of numerical error and dissipation by increasing grid resolution, there are still many flow problems for which the use of low-order methods would be too expensive, unsuitable or even impractical [32].

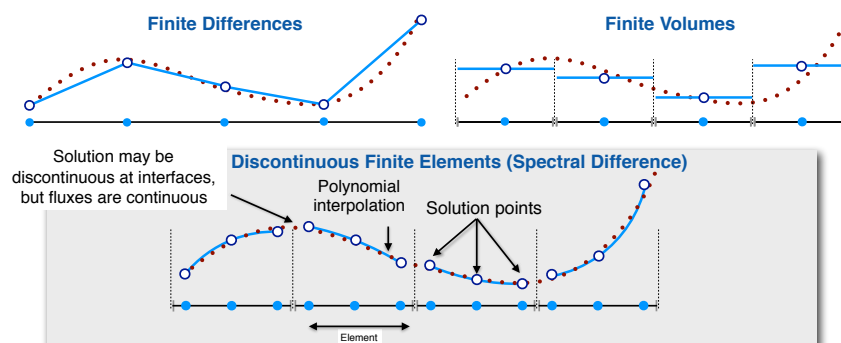


Figure 1.3: Schematic of three major numerical approaches.

High-order methods provide an obvious solution to many of the above mentioned problems. However, high order finite volume and finite difference methods require large stencils that are (frequently) non-compact. Furthermore, it is difficult to reliably and robustly create a high-order reconstruction procedure for finite volume or finite difference schemes on unstructured meshes, and thus, such methods are generally impractical for complex geometries in real-world applications.

In order to overcome these limitations, high-order discontinuous finite element methods (see Figure 1.3) for solving the compressible Navier-Stokes equations on unstructured grids have been extensively studied during the last decade. By far the most mature and widely used of these schemes are based on the discontinuous Galerkin method [31, 33, 34]. Recently, however, several alternative high-order methods have been proposed, including spectral difference [35–37] and flux reconstruction [38–40] type schemes, which potentially offer increased efficiency and reduced algorithmic complexity compared to discontinuous Galerkin methods. These methods allow for one to obtain an arbitrary order of accuracy with a compact stencil on unstructured grids and are extremely well suited for parallel environments. Hence the growing interest toward these family of schemes for high-fidelity simulations of practical flows.

The numerical study of detonation stability typically requires running simulations for extremely long time (thousands of reaction times) to achieve convergence. In addition, high spacial resolution is needed for a good characterization of stability thresholds, formation of shock waves, etc. . . . Therefore, in this work we take advantage of high-order methods for the numerical solution of the Navier-Stokes equations, and we adopt the spectral difference scheme given its relative simplicity and high efficiency. The details of the numerical scheme are presented in Chapter 3.



# Chapter 2

## Detonation and deflagration waves

### Sommaire

---

<b>2.1</b>	<b>Phenomenological description of 1D deflagrations and detonations . . . . .</b>	<b>21</b>
2.1.1	Detonation wave . . . . .	21
2.1.2	Deflagration wave . . . . .	23
<b>2.2</b>	<b>Gasdynamic theory of steady combustion waves . . . . .</b>	<b>23</b>
2.2.1	The Navier-Stokes equations . . . . .	23
2.2.2	The Rayleigh line and the Hugoniot curve . . . . .	24
2.2.3	Rankine-Hugoniot relations . . . . .	27
2.2.4	The Chapman-Jouguet criterion and the ZND detonation structure . . . . .	28
<b>2.3</b>	<b>The ZFK flame theory . . . . .</b>	<b>30</b>
2.3.1	Problem formulation . . . . .	30
2.3.2	The reaction rate . . . . .	32
2.3.3	Solution for unity Lewis number . . . . .	34
2.3.4	Solution for non-unity Lewis number . . . . .	37

---

In this chapter, we review the basic theories of detonations and deflagrations, focusing mainly on the aspects relevant to forthcoming developments in subsequent chapters. A phenomenological description of detonations and deflagrations is provided in §2.1. Then, in §2.2 we discuss the gasdynamic theory of detonations and deflagrations, which allows us to obtain the jump relations across a combustion wave and to fully resolve the inner structure of a detonation wave and obtain its propagation velocity. Finally, in §2.3 we review the Zel'dovich-Frank Kamenetskii flame theory which allows us to resolve the inner structure of a deflagration wave and compute its propagation velocity.

### 2.1 Phenomenological description of 1D deflagrations and detonations

In this section, we present a brief qualitative description of detonation and deflagration waves. More complete discussions can be found in dedicated textbooks such as Williams [41] and Clavin & Searby [3].

#### 2.1.1 Detonation wave

A detonation is a combustion wave that propagates through a reactive mixture at supersonic speeds. The inner structure of a detonation wave is shown schematically in Figure 2.1. This structure is known

as the ZND structure (after the three 20<sup>th</sup> century scientists Zel'dovich, von Neumann and Döring), and it consists of a *leading shock wave* followed by an *induction zone* then a *reaction zone*. The fresh gas is compressed as it crosses the leading shock wave; its temperature increases, and its flow velocity decreases to a subsonic value. Just downstream of the shock, the gas is said to be in the *Neumann state*. The increase in temperature causes the reaction to start after a short induction period. Reactants are thus consumed in the reaction zone, and the mixture expands and accelerates again towards the exit of the reaction zone.

In the case of a self-supported detonation traveling at a relatively constant velocity, known as a *Chapman-Jouguet (CJ) detonation*, the reaction products reach a sonic velocity at the exit of the reaction zone. We call the point at which the reactants achieve a sonic speed the *CJ point*. The sonic-flow condition at the exit of the reaction zone implies that such a detonation is in effect a “choked flow”, meaning that any rarefaction waves propagating in the burnt gases can not penetrate into the inner structure of the detonation. This protects the wave from getting dissipated and allows it to keep propagating steadily. In §2.2 we shall justify this sonic-flow condition and obtain the jump relations for flow properties across a CJ detonation.

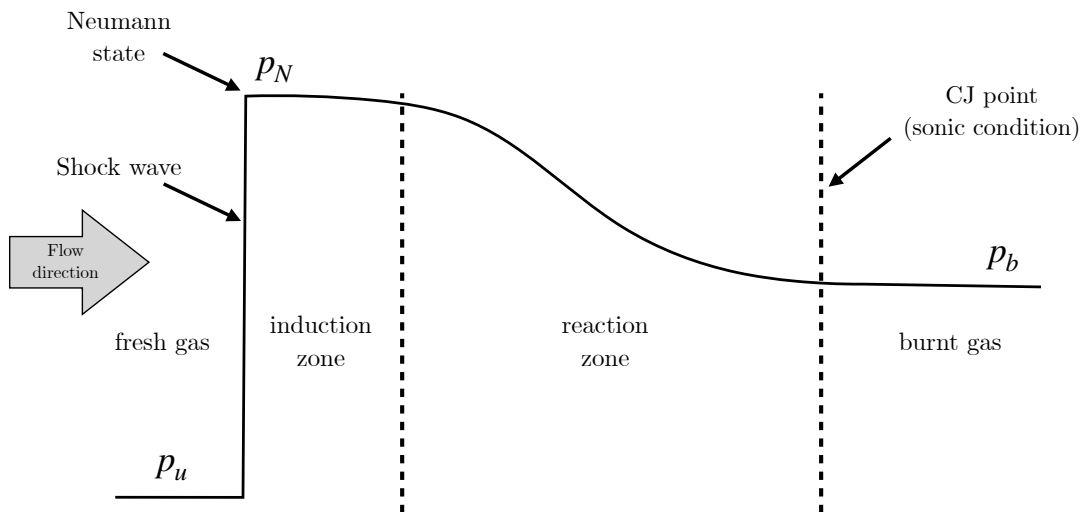


Figure 2.1: Schematic diagram of pressure variation across a detonation wave. The diagram shows the inner structure of the detonation wave (ZND structure) characterized by an inert shock wave, followed by an induction zone, then a reaction zone.

The ignition delay of the shocked gases (in the induction zone) is due to the separation of time scales between the elastic collisions which control the inner structure of the shock on the one hand, and the non-elastic collisions which control the reaction rate on the other hand [3]. Elastic collisions between the gas molecules occur at a very short time scale, while the more energetic non-elastic collisions involved in the chemical reactions are less frequent and take place at a longer time scale. For this reason, fresh gases remain inert inside the leading shock and in the induction zone, and the reaction only takes place later in the reaction zone.

One can show with dimensional analysis, however, that the reaction time scale in detonations is typically much smaller than diffusion time scales [3], so that diffusive effects have no time to affect the dynamics of a detonation wave. We shall see in §2.2 that this simplifies the treatment of detonations as compared to deflagrations, and it allows us to resolve the inner structure of a detonation and obtain the propagation speed purely in gasdynamic terms.

### 2.1.2 Deflagration wave

Contrary to a detonation, a deflagration is a slow subsonic combustion wave that is driven mainly by diffusion. The inner structure of a deflagration wave is shown in Figure 2.2, where we can see that it consists of a *preheat zone* followed by a *reaction zone*.

As fresh gases enter the preheat zone, their temperature increases due to heat conduction from the reaction zone. The temperature however remains sufficiently small so that the reaction rate is negligible in the preheat zone. Nonetheless, the reactant mass fraction decreases significantly due to mass diffusion between the preheat and reaction zones. The gases then enter the reaction zone where their temperature becomes large enough for combustion to take place.

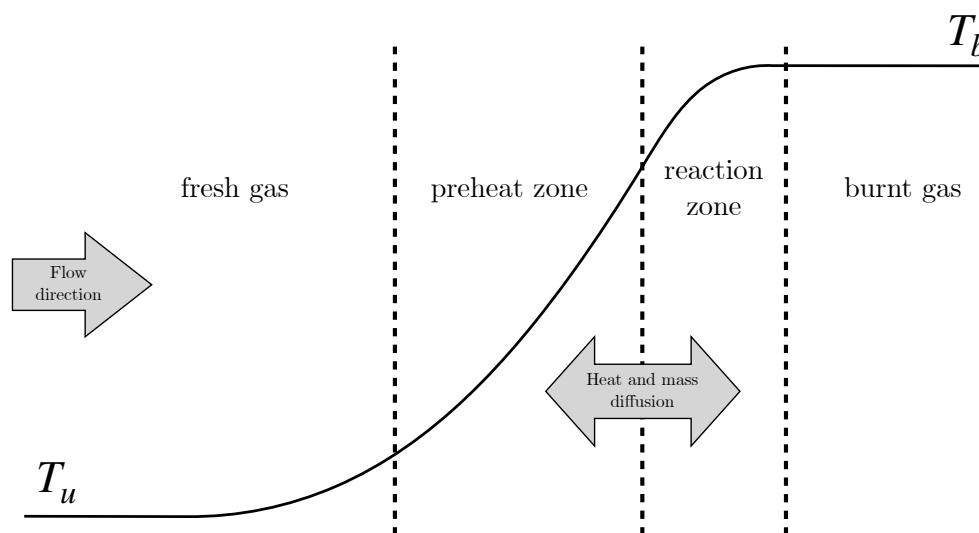


Figure 2.2: Sketch of the temperature profile across a deflagration wave (a premixed flame). The wave propagation is controlled by heat and mass diffusion between the reaction and preheat zones.

As shall be illustrated in detail in §2.3, the inner structure of a deflagration wave and its propagation velocity are controlled by a balance between advection, diffusion, and reaction kinetics. In the preheat zone, the reaction rate is negligible and the flame structure is governed by a balance between heat advection downstream due to flow velocity and heat conduction upstream due to temperature gradient (Figure 2.2). In the reaction zone, advection transport is negligible, and the flame is governed by the balance between heat production by the chemical reaction and upstream heat conduction.

Finally, due to the very low Mach number of a deflagration wave, pressure variation across the wave is negligible, and the treatment of the problem is often simplified by assuming the flow to be isobaric.

## 2.2 Gasdynamic theory of steady combustion waves

### 2.2.1 The Navier-Stokes equations

All flows treated in this text are described by the one-dimensional reactive Navier-Stokes equations, which embody the principles of conservation of mass, momentum, energy and chemical species. In their conservative form, the equations are expressed as

$$\frac{\partial \mathbf{U}}{\partial t} + \frac{\partial \mathbf{F}}{\partial x} = \mathbf{S} \quad (2.1)$$

where  $\mathbf{U}$  is the vector of conservative variables,  $\mathbf{F}$  is the vector sum of advective and diffusive fluxes,  $\mathbf{F} = \mathbf{F}_a + \mathbf{F}_v$ , and  $\mathbf{S}$  is the source vector:

$$\mathbf{U} = \begin{pmatrix} \rho \\ \rho u \\ \rho E \\ \rho Y \end{pmatrix}, \quad \mathbf{F}_a = \begin{pmatrix} \rho u \\ \rho u^2 + p \\ \rho u E + up \\ \rho u Y \end{pmatrix}, \quad \mathbf{F}_v = \begin{pmatrix} 0 \\ -\mu \frac{\partial u}{\partial x} \\ -\mu u \frac{\partial u}{\partial x} - \lambda \frac{\partial T}{\partial x} \\ -\rho D \frac{\partial Y}{\partial x} \end{pmatrix}, \quad \mathbf{S} = \begin{pmatrix} 0 \\ 0 \\ \rho q_m W \\ \rho W \end{pmatrix}. \quad (2.2)$$

In the above equations,  $\rho$  denotes the mass density,  $u$  the flow velocity,  $p$  the pressure and  $T$  the temperature.  $E$  is the total energy per unit mass (internal + kinetic) and  $Y$  is the reaction progress variable, which goes from 0 in the reactants to 1 in the products.  $\mu$  is the dynamic viscosity,  $\lambda$  is the thermal conductivity and  $D$  is mass diffusivity. The derivation of these equations from fundamental principles can be found in standard textbooks [42, 43].

Throughout this text, to simplify the theoretical analyses, the flow is assumed to be an ideal gas with constant heat capacities, and an irreversible single-step reaction model is used whose rate  $W$  is determined by an Arrhenius law. The heat release per unit mass  $q_m$  is also a known constant, and so are  $\mu$ ,  $\lambda$  and  $\rho D$ .

### 2.2.2 The Rayleigh line and the Hugoniot curve

In this section, we treat a steady one-dimensional combustion wave, as illustrated in Figure 2.3. Applying the steady flow condition  $\frac{\partial}{\partial t}(\cdot) = 0$  to equations (2.1), one obtains for mass conservation:

$$\frac{d\rho u}{dx} = 0 \quad (2.3)$$

and for the conservation of momentum:

$$\frac{d}{dx} \left( \rho u^2 + p - \mu \frac{du}{dx} \right) = 0. \quad (2.4)$$

Combining the conservation of energy and chemical species equations by eliminating  $\rho W$  from both equations gives

$$\frac{d}{dx} \left[ \rho u E + up - \mu u \frac{du}{dx} - \lambda \frac{dT}{dx} - q_m \left( \rho u Y - \rho D \frac{dY}{dx} \right) \right] = 0. \quad (2.5)$$

Integrating equations (2.3-2.5) with respect to  $x$  between two stations 1 and 2 far upstream and downstream from the wave respectively, and assuming gradients are negligible at these two stations, i.e.  $\frac{d}{dx}(\cdot) = 0$ , one obtains

$$\rho_u u_u = \rho_b u_b \quad (2.6)$$

$$\rho_u u_u^2 + p_u = \rho_b u_b^2 + p_b \quad (2.7)$$

$$h_u + \frac{u_u^2}{2} + q_m = h_b + \frac{u_b^2}{2} \quad (2.8)$$

where in the last equation we used  $E = c_v T + \frac{u^2}{2} = h - \frac{p}{\rho} + \frac{u^2}{2}$  with  $h = c_p T$  being the specific (sensible) enthalpy. In the above equations, the subscript  $_u$  denotes fresh (unburnt) gas at station 1, and subscript  $_b$  denotes burnt gas at station 2. Equations (2.6-2.8) in addition to the equation of state (2.18) represent a system of four equations in five unknowns ( $\rho_b$ ,  $u_b$ ,  $p_b$ ,  $h_b$  and  $u_u$ ). Thus, the system can only be solved up to a single free parameter.

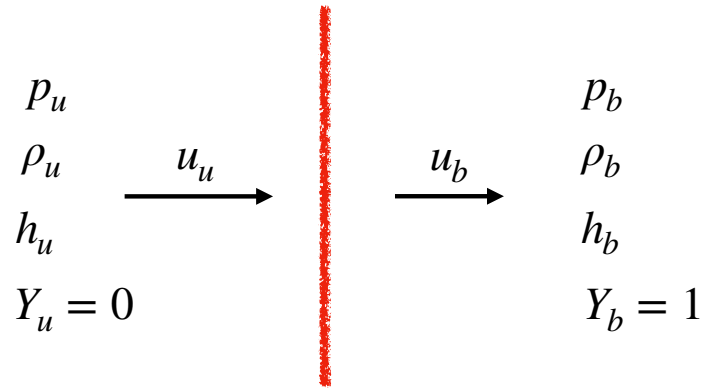


Figure 2.3: Sketch of a steady 1D combustion wave.

Using equations (2.6) and (2.7), the mass flux across the wave can be expressed as

$$m = \rho_u u_u = \rho_b u_b = \sqrt{\frac{p_b - p_u}{v_u - v_b}} \quad (2.9)$$

where  $v \equiv 1/\rho$  is the specific volume. Therefore  $m$  is real only if  $p_b > p_u$  and  $v_b < v_u$ , which corresponds to a compression wave (detonation) or if  $p_b < p_u$  and  $v_b > v_u$  which corresponds to an expansion wave (deflagration). These two regions are illustrated in Figure 2.4, in which the normalized variables  $x$  and  $y$  are defined as

$$x \equiv \frac{v}{v_u}, \quad y \equiv \frac{p}{p_u}. \quad (2.10)$$

Introducing the speed of sound in the fresh mixture  $a_u$  and the Mach number  $M_u$  defined as

$$a_u \equiv \sqrt{\gamma \frac{p_u}{\rho_u}}, \quad M_u \equiv \frac{u_u}{a_u}, \quad (2.11)$$

where  $\gamma$  is the ratio of specific heats, equation (2.9) can be rewritten as

$$\gamma M_u^2 = \frac{y_b - 1}{1 - x_b} \quad (2.12)$$

or

$$y_b = -\gamma M_u^2 x_b + \gamma M_u^2 + 1. \quad (2.13)$$

Equation (2.13) remains valid at any intermediate station between 1 and 2 as long as diffusive phenomena are negligible at that station. As discussed in the previous section, this is not usually the case for a deflagration wave which is dominated by diffusive effects, however, for a detonation this is generally true everywhere in the inner structure of the wave except for the thin shock region. Therefore, one can write in general for intermediate points of a detonation

$$y = -\gamma M_u^2 x + \gamma M_u^2 + 1. \quad (2.14)$$

Introducing the notation

$$\mathcal{P} \equiv \frac{\gamma + 1}{2\gamma}(y - 1), \quad \mathcal{V} \equiv \frac{\gamma + 1}{2}(x - 1), \quad (2.15)$$

equation (2.14) can be written in the simpler form

$$\mathcal{P} = -M_u^2 \mathcal{V}. \quad (2.16)$$

Equation (2.16) describes the thermodynamic path followed by a fluid element from station 1 to 2, which is called the *Rayleigh line* or the *Mikhelson-Rayleigh line*. It is shown as the dashed line in Figure 2.4.

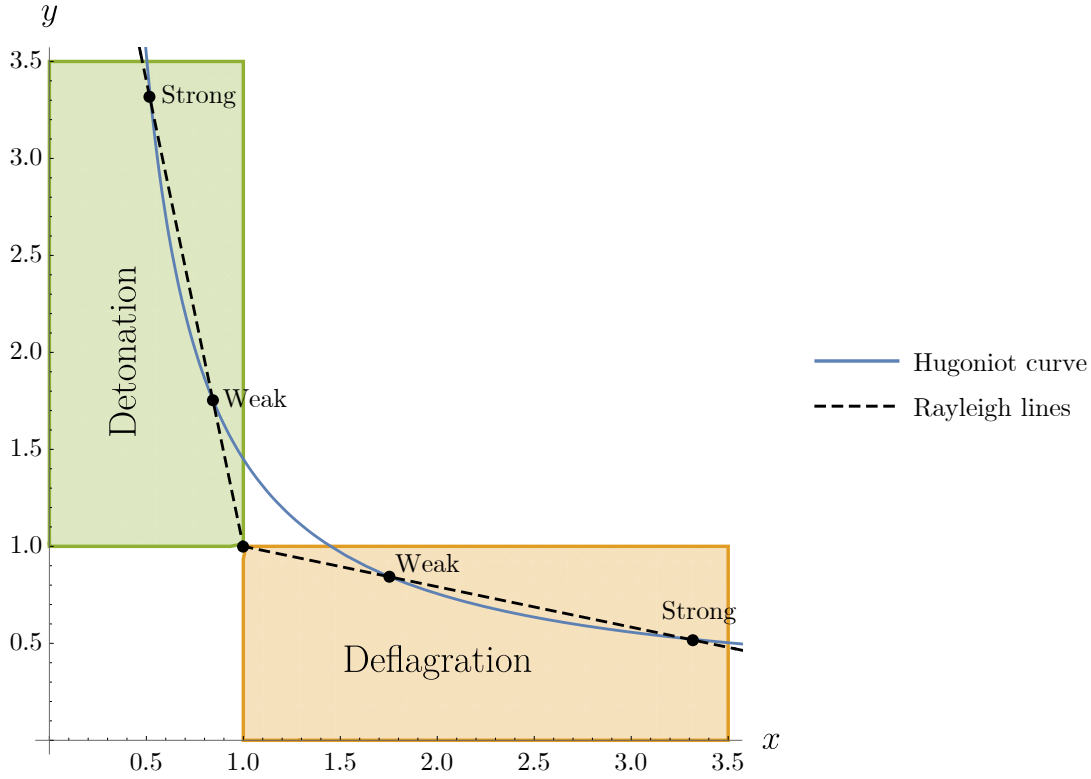


Figure 2.4:  $p$ - $v$  plot for a stationary combustion wave. Shaded regions denote the detonation and deflagration regimes.

Solving equations (2.9) for  $u_u^2$  and  $u_b^2$  as functions of  $p$  and  $v$ , and substituting the result in equation (2.8), one obtains

$$h_b - h_u - \frac{1}{2}(p_b - p_u)(v_b + v_u) = q_m. \quad (2.17)$$

Then, using the equation of state

$$h = c_p T = \frac{\gamma}{\gamma - 1} p v \quad (2.18)$$

and multiplying equation (2.17) by  $(\gamma^2 - 1)/(2\gamma p v)$  gives

$$\mathcal{P}\mathcal{V} + \mathcal{P} + \mathcal{V} = \mathcal{Q}, \quad \text{where} \quad \mathcal{Q} \equiv \frac{\gamma + 1}{2} \frac{q_m}{c_p T_u}. \quad (2.19)$$

which is an equation for an equilateral hyperbola in the  $\mathcal{P}$ - $\mathcal{V}$  plane:

$$(\mathcal{P} + 1)(\mathcal{V} + 1) = 1 + \mathcal{Q}. \quad (2.20)$$

This hyperbola is called the *Hugoniot curve*, and is shown as the solid curve in Figure 2.4. It represents the locus of the burnt-gas state downstream of the combustion wave corresponding to the initial state ( $x = 1, y = 1$ ).

### 2.2.3 Rankine-Hugoniot relations

The exact location of the burnt-gas state is determined by the intersection of the Rayleigh line and the Hugoniot curve. Considering  $M_u$  to be the free parameter in our problem, and substituting equation (2.16) into (2.20), one obtains a quadratic equation for  $\mathcal{P}$

$$\mathcal{P}^2 - (M_u^2 - 1)\mathcal{P} + M_u^2\mathcal{Q} = 0 \quad (2.21)$$

which has two real roots if the discriminant is positive:

$$\Delta \equiv (M_u^2 - 1)^2 - 4M_u^2\mathcal{Q} > 0 \quad (2.22)$$

On the detonation branch (in Figure 2.4), there exists a minimum value for  $M_u$  above which two real roots exist for  $\mathcal{P}$ . One of these roots corresponds to the so-called *strong* (or *overdriven*) detonation, and the other to the *weak* detonation. This minimum value for  $M_u$  is called the Chapman-Jouguet detonation Mach number, and is given by

$$M_{u_{CJ}} = \sqrt{\mathcal{Q}} + \sqrt{\mathcal{Q} + 1} > 1. \quad (2.23)$$

On the deflagration branch (in Figure 2.4), there exists a maximum value for  $M_u$  below which two real roots exist for  $\mathcal{P}$  corresponding to *strong* and *weak* deflagrations. This maximum value for  $M_u$  is called the Chapman-Jouguet deflagration Mach number, and is given by

$$M_{u_{CJ}} = \sqrt{\mathcal{Q} + 1} - \sqrt{\mathcal{Q}} < 1. \quad (2.24)$$

As such, a steady detonation is always supersonic, while a steady deflagration is always subsonic.

Solving the quadratic equation (2.21) and using (2.15), one obtains the pressure ratio across the combustion wave

$$\frac{p_b}{p_u} = \frac{\gamma \left( M_u^2 \pm \sqrt{\Delta} \right) + 1}{\gamma + 1}, \quad (2.25)$$

and substituting into equation (2.16), one obtains the density ratio

$$\frac{v_b}{v_u} = \frac{\rho_u}{\rho_b} = \frac{\gamma M_u^2 + 1 \mp \sqrt{\Delta}}{(\gamma + 1)M_u^2}. \quad (2.26)$$

Using the continuity equation (2.6), we get the velocity ratio

$$\frac{u_b}{u_u} = \frac{\gamma M_u^2 + 1 \mp \sqrt{\Delta}}{(\gamma + 1)M_u^2}. \quad (2.27)$$

Equations (2.25-2.27) are known as the Rankine-Hugoniot relations for a combustion wave. The upper plus-minus sign in these equations corresponds to the strong detonation (or weak deflagration), and the lower plus-minus sign corresponds to the weak detonation (or strong deflagration). Rankine-Hugoniot relations for an inert shock are obtained from equations (2.25-2.27) by setting  $\mathcal{Q} = 0$  in equation (2.22):

$$\frac{p_2}{p_1} = \frac{2\gamma M^2 - \gamma + 1}{\gamma + 1}, \quad (2.28)$$

$$\frac{\rho_2}{\rho_1} = \frac{(\gamma + 1)M^2}{(\gamma - 1)M^2 + 2}, \quad (2.29)$$

$$\frac{u_2}{u_1} = \frac{(\gamma - 1)M^2 + 2}{(\gamma + 1)M^2}. \quad (2.30)$$

For the Chapman-Jouguet wave, we set  $\Delta = 0$  to obtain:

$$\frac{p_b}{p_u} = \frac{\gamma M_u^2 + 1}{\gamma + 1}, \quad (2.31)$$

$$\frac{\rho_b}{\rho_u} = \frac{(\gamma + 1)M_u^2}{\gamma M_u^2 + 1}, \quad (2.32)$$

$$\frac{u_b}{u_u} = \frac{\gamma M_u^2 + 1}{(\gamma + 1)M_u^2}. \quad (2.33)$$

In the reference frame of the fresh gases, we can denote the propagation velocity of the detonation wave by  $\mathcal{D} = u_u$ . The burnt gas velocity in this frame would then be  $u'_b = \mathcal{D} - u_b$ . Substituting this into equation (2.27), we get

$$\frac{u'_b}{\mathcal{D}} = \frac{M_u^2 - 1 \mp \sqrt{\Delta}}{(\gamma + 1)M_u^2}. \quad (2.34)$$

On the detonation branch ( $M_u > 1$ ),  $\sqrt{\Delta}$  is always less than  $M_u^2 - 1$  (see equation (2.22)), and thus  $u'_b$  is always in the same direction as  $\mathcal{D}$ . On the deflagration branch ( $M_u < 1$ ),  $\sqrt{\Delta}$  is always less than  $1 - M_u^2$ , and thus  $u'_b$  is always in the opposite direction to that of  $\mathcal{D}$ .

The flow Mach number in the burnt gas  $M_b$  (in the reference frame of the wave) can be obtained from equations (2.25-2.27) as

$$M_b^2 = \frac{\gamma M_u^2 + 1 \mp \sqrt{\Delta}}{\gamma(M_u^2 \pm \sqrt{\Delta}) + 1}, \quad (2.35)$$

where it can be easily seen that for a strong detonation, the numerator is less than the denominator, and thus  $M_b < 1$ , while the opposite is true for a weak detonation ( $M_b > 1$ ). For a Chapman-Jouguet detonation ( $\Delta = 0$ ), the burnt gas Mach number is unity:

$$M_{bCJ} = 1, \quad (2.36)$$

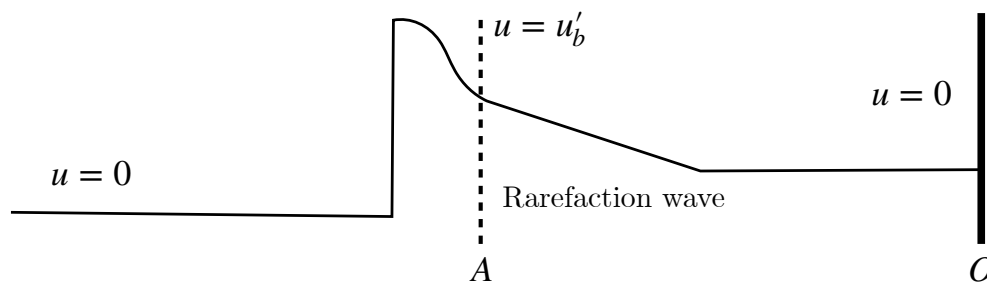
and we get a sonic flow condition downstream of the wave.

## 2.2.4 The Chapman-Jouguet criterion and the ZND detonation structure

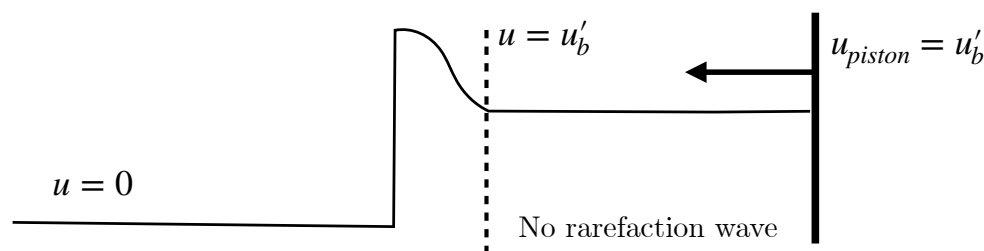
Since the early investigations by V. A. Mikhelson [44], David Chapman [45] and Émile Jouguet [46] around the turn of the 20-th century, it has been known that the propagation velocity of a detonation obtained by the tangency condition between the Hugoniot curve and the Rayleigh line is usually in good agreement with experiments. However, no theoretical justification for this agreement was given by these early investigators, thus efforts have been made in the following years and decades to provide a rigorous justification for the choice of the Chapman-Jouguet condition.

Considering a detonation wave propagating from the closed end of a tube (Figure 2.5), one can easily rule out the possibility that it is a strong detonation. This is because the flow velocity at point  $A$  just downstream of the detonation needs to be matched with the zero flow velocity at point  $O$  at the closed end of the tube, which means a rarefaction wave should exist between points  $A$  and  $O$ . However, since the flow velocity downstream of a strong detonation is subsonic with respect to the wave (equation (2.35)), the rarefaction wave will propagate into the detonation and attenuate it.

In fact, a strong detonation can only be maintained if the rarefaction wave is prevented from forming, which is achieved by moving a piston from the end of the tube at the same velocity as that of the burnt gas  $u'_b$ . The piston provides an overdriving force for the detonation, and that's why a strong detonation is also termed "overdriven".



(a) Point  $O$  at the closed end of the tube has zero velocity. A rarefaction wave exists between points  $A$  and  $O$ .



(b) A piston at the closed end is moving with velocity  $u'_b$ , overdriving the detonation.

Figure 2.5: Pressure profile across a detonation wave propagating from the closed end of a tube. A strong detonation cannot be maintained in (a) because the rarefaction wave would penetrate into the detonation and attenuate it.

Weak detonations on the other hand, were a bit more difficult to dismiss by investigators, as that required the consideration of the inner structure of detonations, called the ZND structure (after Zel'dovich, von Neumann and Döring). In his work [47] in 1942, von Neumann introduced intermediate Hugoniot curves corresponding to partially-reacted states with partial heat releases  $q \in [0, q_m]$ . von Neumann demonstrated that weak detonations can be excluded in the case where these partial Hugoniots do not intersect, which is shown in Figure 2.6.

The demonstration is carried out by constructing the thermodynamic path followed by a fluid element in the inner structure of the detonation. As stated in §2.2.2, in regions where viscous effects are negligible the fluid element is restricted to move along the Rayleigh line, so the problem is to determine which Rayleigh line the fluid element follows, and how does it move along it. Indeed, the Rayleigh line which the fluid element follows must intersect all the partial Hugoniots, and in the case of non-intersecting Hugoniots, the line with the minimum Mach number which satisfies this condition is the one tangent to the full Hugoniot at the CJ point as shown in Figure 2.6. One can observe in the figure that two solution points exist at any given value of  $q$ , corresponding to the strong and weak detonation branches (points  $A$  and  $B$  respectively). Now if we consider an irreversible exothermic reaction occurring at a finite rate in time, then the fluid element can only move continuously from one partial Hugoniot to the next, in the direction of increasing  $q$ . Thus, the fluid element can either move up starting from point  $U$  or down starting from  $N$ . However, at any given value of  $q$ , the conservation laws do not prevent the fluid element from jumping instantaneously from the strong detonation point  $A$  to the weak detonation point  $B$ , or vice-versa.

These possible jumps undergone by the fluid element can be examined more closely from a thermodynamics point of view. As we have seen from the Rankine-Hugoniot relations obtained in §2.2.3, the

flow is subsonic at point  $A$ , while it is supersonic at point  $B$ . Moreover, the flow at point  $B$  has a lower pressure and density than at point  $A$ . Therefore, a jump from point  $B$  to  $A$  that is consistent with the conservation equations can only be a shock wave, while a jump from  $A$  to  $B$  can only be a rarefaction shock. As a result, and since rarefaction shocks entail a decrease in entropy which is prohibited by the second law of thermodynamics, only jumps from  $B$  to  $A$  are possible.

Thus, we can state that the fluid element moves continuously in the inner structure of the detonation along the Rayleigh line from one partial Hugoniot to the next, except for a unique possible jump from the weak-detonation branch to the strong-detonation branch. The final piece for the construction of the thermodynamic path of the fluid element is provided by considering the initial state. Indeed, we know that a detonation wave exhibits a very rapid reaction rate, so that the fluid element goes from  $q = 0$  to  $q = q_m$  in a very short time as it crosses the detonation structure. In such case, the reaction cannot start from the initial state  $U$  since this state is characterized by a very low temperature at which the mixture is frozen far away from chemical equilibrium. In the words of von Neumann : “. . . the reaction cannot start in this region. If it did – for any reason whatever – it should a fortiori have done so in the intact explosive (i.e before the arrival of the detonation wave). There was much more time available there, and yet, by assumption, no reaction!”. Therefore, for the reaction to set in, the fluid element first needs to jump from point  $U$  to point  $N$  where the temperature is much larger and can sustain a rapid reaction rate.

Thus, a shock wave exists at the leading edge of the detonation taking the fluid element from  $U$  to  $N$ . From there, the fluid element moves down the Rayleigh line passing through the strong solution points of the partial Hugoniots. The fluid element cannot jump to a weak-solution point by a rarefaction shock, and all possible Rayleigh lines with  $M > M_{CJ}$  would lead the fluid element to reach the full Hugoniot on the strong-detonation branch, which as discussed above cannot be the case for a self-supported detonation. Therefore, the Rayleigh line with  $M = M_{CJ}$ , intersecting the full Hugoniot at the CJ point, is the only valid thermodynamic path for the fluid element to follow, and the Chapman-Jouguet condition is verified.

However, von Neumann also showed that in the case of intersecting Hugoniots, one might have a Rayleigh line which would take the fluid element *continuously* from the strong-detonation to the weak-detonation branch, so that the fluid element arrives at the weak solution point of the full Hugoniot. Such detonations with intersecting Hugoniot curves are referred to as pathological detonations. A detonation driven by a two-step reaction, an exothermic step followed by an endothermic step, would be an example of such pathological detonations [48, 49].

## 2.3 The ZFK flame theory

In this section, we review the asymptotic analysis by Zeldovich and Frank-Kamenetskii (abbreviated ZFK) for the thermal propagation of flames [50]. In this analysis, our goal is to resolve the internal structure of a one-dimensional laminar premixed flame, and to calculate the laminar flame speed in terms of flow parameters. A more extensive treatment can be found in [3]. The ZFK analysis is carried out in the asymptotic limit of a large Zeldovich number (to be defined later in this section).

### 2.3.1 Problem formulation

We consider a one-dimensional flame steadily propagating in a reactive mixture with a laminar flame speed  $U_L$  that is much less than the speed of sound

$$\frac{U_L}{a_u} \ll 1. \quad (2.37)$$

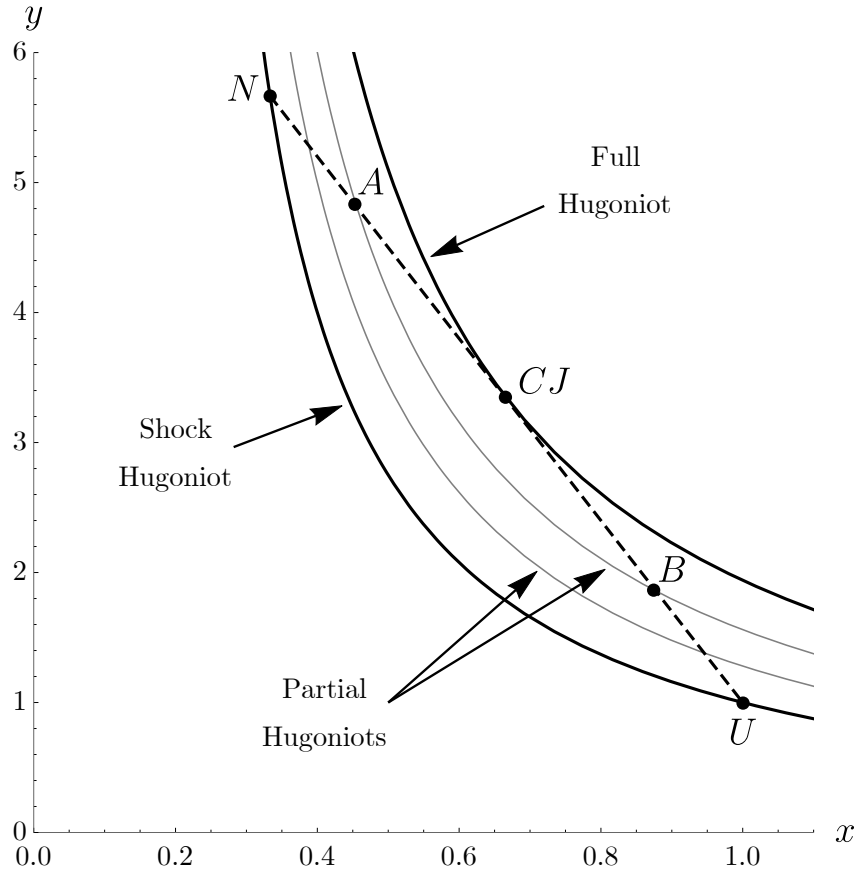


Figure 2.6: The path of a fluid element across the non-intersecting partially reacted Hugoniot curves.

Under these conditions, one can show that pressure variation across the flame is negligible so that the flow is quasi-isobaric [3]. Also, for this low Mach number, one has in the reference frame of the flame

$$u^2 \ll a^2 = RT \propto c_v T \quad (2.38)$$

so that the kinetic energy of the flow is negligible compared to its internal energy.

We consider the energy and species equations in (2.1). Imposing the assumptions of steady flow  $\frac{\partial}{\partial t}(\cdot) = 0$  along with the isobaric approximation  $\frac{dp}{dx} = 0$  and neglecting terms in the energy equation proportional to  $u^2$ , one arrives at the simplified forms of the conservation equations of energy and species:

$$m c_p \frac{dT}{dx} - \lambda \frac{d^2 T}{dx^2} = \rho q_m W \quad (2.39)$$

$$m \frac{dY}{dx} - \rho D \frac{d^2 Y}{dx^2} = \rho W \quad (2.40)$$

where we have introduced the constant mass flux  $m \equiv \rho u = \text{constant}$ , and we assumed that  $c_p$  and  $\lambda$  are constant as well. The following boundary conditions apply far upstream and downstream of our flame:

$$x \rightarrow -\infty : \quad T = T_u, \quad Y = 0, \quad \frac{dT}{dx} = 0, \quad \frac{dY}{dx} = 0 \quad (2.41)$$

$$x \rightarrow +\infty : \quad T = T_b, \quad Y = 1, \quad \frac{dT}{dx} = 0, \quad \frac{dY}{dx} = 0. \quad (2.42)$$

The burnt gas temperature  $T_b$  is not known a priori. However, it can be easily calculated by eliminating  $\rho W$  from equation (2.39) using equation (2.40) then integrating from  $-\infty$  to  $+\infty$  to obtain

$$c_p(T_b - T_u) = q_m \quad \Rightarrow \quad T_b = T_u + \frac{q_m}{c_p}. \quad (2.43)$$

Our goal now is to solve the system (2.39-2.42) to obtain the temperature and progress variable profiles  $T(x)$  and  $Y(x)$  and the laminar flame speed  $U_L$ . The problem can be simplified by introducing the reduced temperature

$$\theta \equiv \frac{T - T_u}{T_b - T_u} \quad (2.44)$$

along with the thermal diffusivity  $D_T$  and the Lewis number  $Le$  defined as

$$D_T \equiv \frac{\lambda}{\rho c_p}, \quad Le \equiv \frac{D_T}{D}. \quad (2.45)$$

Then, equations (2.39-2.40) can be written as

$$m \frac{d\theta}{dx} - \rho D_T \frac{d^2\theta}{dx^2} = \rho W \quad (2.46)$$

$$m \frac{dY}{dx} - \rho \frac{D_T}{Le} \frac{d^2Y}{dx^2} = \rho W \quad (2.47)$$

with the boundary conditions

$$x \rightarrow -\infty : \quad \theta = 0, \quad Y = 0, \quad \frac{d\theta}{dx} = 0, \quad \frac{dY}{dx} = 0 \quad (2.48)$$

$$x \rightarrow +\infty : \quad \theta = 1, \quad Y = 1, \quad \frac{d\theta}{dx} = 0, \quad \frac{dY}{dx} = 0. \quad (2.49)$$

### 2.3.2 The reaction rate

In order to solve the system (2.46-2.49) and resolve the inner structure of the flame, one needs to know the reaction rate  $W$  as a function of  $Y$  and  $\theta$ . The reaction rate  $W$  is given by Arrhenius law. If we denote the reactant concentration by  $c$ , Arrhenius law states for a reaction of order  $\nu$  in a homogeneous medium:

$$\frac{dc}{dt} = -\frac{c^\nu}{c_u^{\nu-1}} \frac{b}{\tau_{coll}} e^{-E_a/k_B T} \quad (2.50)$$

where  $E_a$  is the activation energy,  $k_B$  is the Boltzmann constant, and  $\tau_{coll}$  is the time scale of elastic collisions between molecules. The factor  $1/c_u^{\nu-1}$  has been introduced to make the prefactor  $b$  dimensionless and of order unity. The product mass fraction  $Y$  is related to  $c$  by the following equation:

$$1 - Y = \frac{M_r}{\rho} c, \quad (2.51)$$

where  $M_r$  is the molar mass of the reactant. Thus, the reaction rate  $W$  is given by

$$W \equiv \frac{dY}{dt} = \left( \frac{\rho}{\rho_u} \right)^{\nu-1} (1 - Y)^\nu \frac{b}{\tau_{coll}} e^{-E_a/k_B T}. \quad (2.52)$$

It is useful to introduce the reaction time  $\tau_r(T)$  as

$$\frac{1}{\tau_r(T)} \equiv \left( \frac{\rho_b}{\rho_u} \right)^{\nu-1} \frac{b}{\tau_{coll}} e^{-E_a/k_B T}, \quad (2.53)$$

so that  $\rho W$  can be written as

$$\rho W = \rho(1 - Y)^\nu \left( \frac{\rho}{\rho_b} \right)^{\nu-1} \frac{1}{\tau_r(T)}. \quad (2.54)$$

For  $T = T_b$ , one obtains the characteristic reaction time  $\tau_{rb}$  defined as

$$\frac{1}{\tau_{rb}} \equiv \frac{1}{\tau_r(T_b)} = \left( \frac{\rho_b}{\rho_u} \right)^{\nu-1} \frac{b}{\tau_{coll}} e^{-E_a/k_B T_b}, \quad (2.55)$$

and one can then express  $\tau_r$  as a function of  $\tau_{rb}$  given by

$$\frac{1}{\tau_r} = \frac{1}{\tau_{rb}} \exp \left[ -\frac{E_a}{k_B} \left( \frac{1}{T} - \frac{1}{T_b} \right) \right]. \quad (2.56)$$

We would like to express  $W$  as a function of the reduced temperature  $\theta$ . Thus, using the identity

$$\frac{T}{T_b} = 1 - \left( 1 - \frac{T_u}{T_b} \right) (1 - \theta), \quad (2.57)$$

equation (2.56) can be written as

$$\frac{1}{\tau_r} = \frac{1}{\tau_{rb}} \exp \left[ -\frac{\beta(1 - \theta)}{1 - (1 - T_u/T_b)(1 - \theta)} \right], \quad (2.58)$$

where  $\beta$  is called the Zeldovich number and is defined as

$$\beta \equiv \frac{E_a}{k_B T_b} (1 - T_u/T_b). \quad (2.59)$$

Then, using equation (2.58), equation (2.54) can be rewritten as

$$\rho W = \rho(1 - Y)^\nu \left( \frac{\rho}{\rho_b} \right)^{\nu-1} \frac{1}{\tau_{rb}} \exp \left[ -\frac{\beta(1 - \theta)}{1 - (1 - T_u/T_b)(1 - \theta)} \right]. \quad (2.60)$$

We then introduce the reduced reaction rate  $w(Y, \theta)$  defined as

$$w(Y, \theta) \equiv \frac{\rho}{\rho_b} \tau_{rb} W \quad \implies \quad \rho W = \frac{\rho_b}{\tau_{rb}} w, \quad (2.61)$$

which from (2.60) can be expressed as

$$w(Y, \theta) = \left( \frac{\rho}{\rho_b} \right)^\nu (1 - Y)^\nu \exp \left[ -\frac{\beta(1 - \theta)}{1 - (1 - T_u/T_b)(1 - \theta)} \right]. \quad (2.62)$$

Using the equation of state (2.18), the isobaric condition ( $p = \text{constant}$ ) implies that

$$\frac{\rho}{\rho_b} = \frac{T_b}{T}, \quad (2.63)$$

then, using equation (2.57),  $w$  can be written as

$$w(Y, \theta) = \frac{(1 - Y)^\nu}{[1 - (1 - T_u/T_b)(1 - \theta)]^\nu} \exp \left[ -\frac{\beta(1 - \theta)}{1 - (1 - T_u/T_b)(1 - \theta)} \right]. \quad (2.64)$$

### 2.3.3 Solution for unity Lewis number

If we assume a unity Lewis number, then equations (2.46) and (2.47) would have the same form. Since the boundary conditions (2.48) and (2.49) are also the same for  $\theta$  and  $Y$ , then one has  $\theta = Y$  and the system reduces to a single equation

$$m \frac{d\theta}{dx} - \rho D_T \frac{d^2\theta}{dx^2} = \frac{\rho_b}{\tau_{rb}} w(\theta) \quad (2.65)$$

where we have used equation (2.61). In the asymptotic limit  $\beta \rightarrow \infty$  and for temperatures very close to the burnt gas temperature,  $\beta(1 - \theta) = \mathcal{O}(1)$ , the expression for  $w$  in equation (2.64) reduces to

$$w(\theta) = (1 - \theta)^\nu e^{-\beta(1-\theta)}. \quad (2.66)$$

As can be seen in Figure 2.7, in the limit  $\beta \rightarrow \infty$  the reaction rate is negligible everywhere except for temperatures very close to that of burnt gas where  $\beta(1 - \theta) = \mathcal{O}(1)$ . This is due to the presence of the exponential term  $e^{-\beta(1-\theta)}$  which goes to zero as soon as  $\theta$  is much less than unity, and the prefactor term  $(1 - \theta)^\nu$  which is zero at  $\theta = 1$ . As a result, the simplified expression in equation (2.66), which is strictly valid for  $\beta(1 - \theta) = \mathcal{O}(1)$ , can actually be used to express  $w$  everywhere with no significant loss in accuracy.

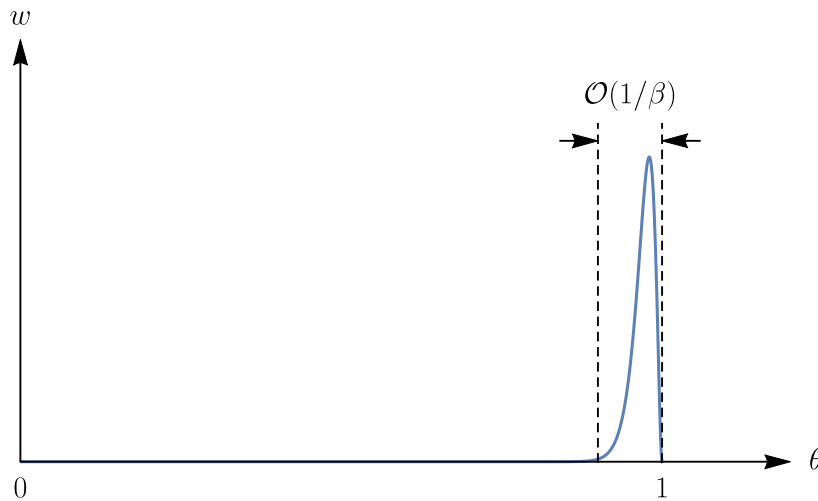


Figure 2.7: Sketch of the reaction rate  $w$  as a function of  $\theta$  as given in equation (2.66) for a large value of  $\beta$ . The bulk of the reaction rate takes place in a small region close to  $\theta = 1$ , with a thickness in the order of  $1/\beta$ .

Now one can see that the reaction rate given by equation (2.66) isn't equal to zero in the fresh gases ( $\theta = 0$ ), and is instead given by  $w(0) = e^{-\beta}$ . Therefore, the flame described by this reaction rate cannot propagate at a steady velocity, and no solution can be found for equation (2.65). This problem is known as *the cold-boundary difficulty*. However, this is only a formal problem since in practice, the reaction rate in fresh gas is very small and is characterized by a much longer time scale than that of flame propagation. Thus, the reaction rate can be neglected in the fresh gas, and to keep the problem mathematically well-posed, we can insert a cut-off temperature for the reaction rate larger than  $T_u$  but much smaller than  $T_b$ , so that  $w = 0$  below this cut-off temperature. For very large  $\beta$ , the solution is independent of the exact value of this cut-off temperature.

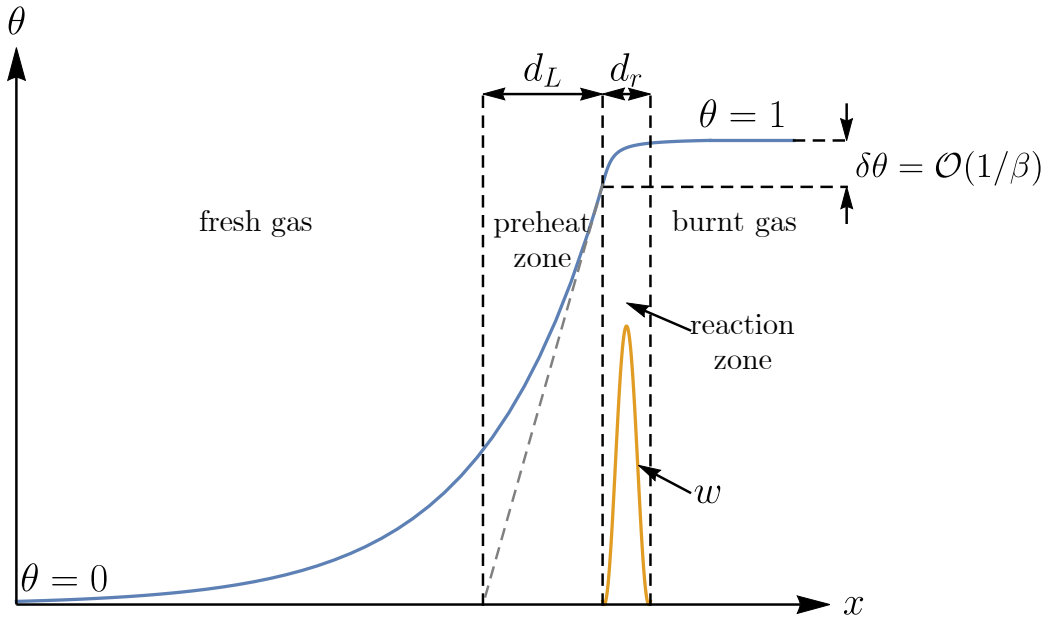


Figure 2.8: Schematic representation of the temperature profile as a function of  $x$  for the flame with large  $\beta$ .

As shown in Figure 2.8, the flame can be divided into two zones: the preheat zone and the reaction zone. In the reaction zone the gas temperature is very close to that of burnt gas,  $\beta(1 - \theta) = \mathcal{O}(1)$ , and the reaction rate is finite. In the preheat zone, the temperature is much less than that of burnt gas  $\beta(1 - \theta) > \mathcal{O}(1)$ , and the reaction rate is practically zero. However, temperature  $\theta$  and progress variable  $Y$  both increase in this zone due to heat and mass diffusion from the reaction zone.

Equation (2.65) shall be solved separately in each of these two zones. In the preheat zone, since the reaction rate is zero, equation (2.65) reduces to

$$m \frac{d\theta}{dx} - \rho D_T \frac{d^2\theta}{dx^2} = 0. \quad (2.67)$$

Integrating this equation with respect to  $x$  and using the boundary conditions (2.48), one obtains

$$m\theta - \rho D_T \frac{d\theta}{dx} = 0. \quad (2.68)$$

Equation (2.68) describes the thermal flux balance in the preheat zone, where the convective flux  $m\theta$  is compensated everywhere by the conductive flux  $\rho D_T \frac{d\theta}{dx}$ . Solving this equation gives the temperature profile in the preheat zone as

$$\theta(x) = e^{\frac{m}{\rho D_T} x}, \quad (2.69)$$

where we have placed the origin  $x = 0$  at the interface of preheat and reaction zones (where  $\theta \approx 1$ ). Equation (2.69) gives the preheat zone thickness as

$$d_L = \frac{\rho D_T}{m} = \frac{D_{T_u}}{U_L} = \frac{D_{T_b}}{U_b}, \quad (2.70)$$

from which one obtains the mass flux  $m$  as

$$m = \frac{\rho D_T}{d_L} = \frac{\rho_u D_{T_u}}{d_L} = \frac{\rho_b D_{T_b}}{d_L}. \quad (2.71)$$

Equation (2.69) also gives the temperature gradient at the interface  $x = 0$  as

$$\left. \frac{d\theta}{dx} \right|_{x=0} = \frac{m}{\rho_b D_{T_b}} = \frac{1}{d_L}. \quad (2.72)$$

We now solve equation (2.65) in the reaction zone. We denote the thickness of the reaction zone by  $d_r$  and the temperature change across this zone by  $\delta\theta$  which is in the order of  $1/\beta$ , as shown in Figure 2.8. Then in the reaction zone, the orders of magnitude of the three terms in equation (2.65) are given by

$$m \frac{d\theta}{dx} \sim m \frac{\delta\theta}{d_r} \sim \frac{\rho_b D_{T_b}}{d_L d_r \beta} \quad (2.73)$$

$$\rho D_T \frac{d^2\theta}{dx^2} \sim \frac{\rho_b D_{T_b}}{d_r} \delta \left( \frac{d\theta}{dx} \right) \sim \frac{\rho_b D_{T_b}}{d_r d_L} \quad (2.74)$$

$$\frac{\rho_b}{\tau_{rb}} w(\theta) \sim \frac{\rho_b}{\tau_{rb}} (\delta\theta)^\nu \sim \frac{\rho_b}{\tau_{rb} \beta^\nu}. \quad (2.75)$$

where in equation (2.74) we have used equation (2.72) and the boundary condition (2.49) to calculate the jump in temperature gradient across the reaction zone. We can see that the conductive term in (2.74) is larger than the advective term in (2.73) by a factor of  $\beta$ . Therefore, the advective term can be neglected in the reaction zone and equation (2.65) simplifies to

$$D_{T_b} \frac{d^2\theta}{dx^2} = -\frac{w(\theta)}{\tau_{rb}}, \quad (2.76)$$

which states that in the reaction zone, heat production by the source term is balanced by heat conduction into the preheat zone. Multiplying the above equation by  $\frac{d\theta}{dx}$  yields

$$\frac{D_{T_b}}{2} \frac{d}{dx} \left( \frac{d\theta}{dx} \right)^2 = -\frac{1}{\tau_{rb}} (1-\theta)^\nu e^{-\beta(1-\theta)} \frac{d\theta}{dx}. \quad (2.77)$$

Integrating the above equation from  $x = 0$  at the interface of preheat and reaction zones to  $x = +\infty$  and using the boundary condition (2.49), one obtains

$$\left. \frac{D_{T_b}}{2} \left( \frac{d\theta}{dx} \right)^2 \right|_{x=0} = \frac{1}{\tau_{rb}} \int_{\theta_i}^1 (1-\theta)^\nu e^{-\beta(1-\theta)} d\theta \quad (2.78)$$

where  $\theta_i$  is the temperature at the interface. Knowing that the integrand in equation (2.78) goes to zero for  $\theta < \theta_i$  (Figure 2.7), one can rewrite the above equation as

$$\left. \frac{D_{T_b}}{2} \left( \frac{d\theta}{dx} \right)^2 \right|_{x=0} = \frac{1}{\tau_{rb}} \int_0^1 (1-\theta)^\nu e^{-\beta(1-\theta)} d\theta. \quad (2.79)$$

Using the change of variable

$$\Theta \equiv \beta(1-\theta), \quad d\Theta = -\beta d\theta, \quad (2.80)$$

equation (2.78) yields

$$\left. \frac{D_{T_b}}{2} \left( \frac{d\theta}{dx} \right)^2 \right|_{x=0} = \frac{1}{\beta^{\nu+1} \tau_{rb}} \int_0^\beta \Theta^\nu e^{-\Theta} d\Theta. \quad (2.81)$$

As  $\beta \rightarrow \infty$ , the above equation yields

$$\left. \frac{D_{T_b}}{2} \left( \frac{d\theta}{dx} \right)^2 \right|_{x=0} = \frac{1}{\beta^{\nu+1} \tau_{rb}} \int_0^\infty \Theta^\nu e^{-\Theta} d\Theta = \frac{\Gamma(\nu+1)}{\beta^{\nu+1} \tau_{rb}} = \frac{\nu!}{\beta^{\nu+1} \tau_{rb}} \quad (2.82)$$

where  $\Gamma$  is the gamma function. Therefore, the temperature gradient at the interface is given by

$$\left. \frac{d\theta}{dx} \right|_{x=0} = \sqrt{\frac{2\nu!}{D_{T_b} \beta^{\nu+1} \tau_{rb}}}. \quad (2.83)$$

Finally, comparing equations (2.72) and (2.83), one obtains the mass flux across the flame as

$$m = \rho_b \sqrt{\frac{2\nu! D_{T_b}}{\beta^{\nu+1} \tau_{rb}}} \quad (2.84)$$

from which the flame speed is obtained as

$$U_L = \frac{m}{\rho_u} = \frac{\rho_b}{\rho_u} \sqrt{\frac{2\nu! D_{T_b}}{\beta^{\nu+1} \tau_{rb}}}, \quad U_b = \frac{m}{\rho_b} = \sqrt{\frac{2\nu! D_{T_b}}{\beta^{\nu+1} \tau_{rb}}}. \quad (2.85)$$

### 2.3.4 Solution for non-unity Lewis number

The solution obtained in the previous section can be easily extended to the more general case with  $Le \neq 1$ . The problem is solved the same way as in the previous section, i.e by solving the equations separately in the preheat and reaction zones, then equating the temperature gradient on both sides at the interface of the two zones in order to obtain the mass flux.

We proceed by the following. Denoting the preheat zone thickness and mass flux for the case with  $Le = 1$  by  $d_{L1}$  and  $m_1$  respectively, one can define the non-dimensional parameters

$$\xi \equiv \frac{x}{d_{L1}} \quad \text{and} \quad \mu \equiv \frac{m}{m_1}. \quad (2.86)$$

Then, multiplying equations (2.46-2.47) by  $d_{L1}/m_1$ , one obtains

$$\mu \frac{d\theta}{d\xi} - \frac{d^2\theta}{d\xi^2} = \frac{1}{\tau_n} w(Y, \theta) \quad (2.87)$$

$$\mu \frac{dY}{d\xi} - \frac{1}{Le} \frac{d^2Y}{d\xi^2} = \frac{1}{\tau_n} w(Y, \theta) \quad (2.88)$$

where we have introduced the non-dimensional time parameter

$$\tau_n \equiv \frac{\tau_{rb} m_1}{\rho_b d_{L1}}, \quad (2.89)$$

and where  $w$  is given by

$$w(Y, \theta) = (1 - Y)^\nu e^{-\beta(1-\theta)}. \quad (2.90)$$

Again, we solve the system separately in the preheat and reaction zones. In the preheat zone, as before the reaction rate  $w$  is negligible, and the equations simplify to

$$\mu \frac{d\theta}{d\xi} - \frac{d^2\theta}{d\xi^2} = 0 \quad (2.91)$$

$$\mu \frac{dY}{d\xi} - \frac{1}{Le} \frac{d^2Y}{d\xi^2} = 0 \quad (2.92)$$

which can be solved to obtain  $\theta$  and  $Y$  as

$$\theta = e^{\mu\xi} \quad (2.93)$$

$$Y = e^{\mu Le \xi}. \quad (2.94)$$

Thus, the temperature gradient at  $\xi = 0$  is given by

$$\left. \frac{d\theta}{dx} \right|_{\xi=0} = \mu. \quad (2.95)$$

In the reaction zone, convective terms are negligible just as before as well. Therefore, equations (2.87-2.88) reduce to

$$-\frac{d^2\theta}{d\xi^2} = \frac{1}{\tau_n} w(Y, \theta) \quad (2.96)$$

$$-\frac{1}{Le} \frac{d^2Y}{d\xi^2} = \frac{1}{\tau_n} w(Y, \theta). \quad (2.97)$$

Eliminating  $w$  from the above equations yields

$$\frac{d^2\theta}{d\xi^2} = \frac{1}{Le} \frac{d^2Y}{d\xi^2}. \quad (2.98)$$

Integrating equation (2.98) twice and using the boundary conditions (2.49), one obtains the relation

$$1 - Y = Le(1 - \theta), \quad (2.99)$$

which can be substituted into equation (2.90) to yield the reaction rate as a function of  $\theta$  alone

$$w(Y, \theta) = Le^\nu (1 - \theta)^\nu e^{-\beta(1-\theta)}. \quad (2.100)$$

The above expression for the reaction rate can then be substituted into equation (2.96) to obtain the second-order equation

$$-\frac{d^2\theta}{d\xi^2} = \frac{1}{\tau_n} Le^\nu (1 - \theta)^\nu e^{-\beta(1-\theta)} \quad (2.101)$$

which is solved in the same way as (2.76) to yield

$$\left. \frac{d\theta}{d\xi} \right|_{\xi=0} = \sqrt{\frac{2\nu! Le^\nu}{\beta^{\nu+1} \tau_n}} = Le^{\nu/2} \quad (2.102)$$

where we have used equations (2.89) and (2.84).

Finally, comparing equations (2.95) and (2.102), one obtains

$$\mu = Le^{\nu/2} \quad (2.103)$$

which gives the mass flux across the flame as

$$m = \rho_b \sqrt{\frac{2\nu! D_{T_b} Le^\nu}{\beta^{\nu+1} \tau_{rb}}} \quad (2.104)$$

and the flame speeds

$$U_L = \frac{\rho_b}{\rho_u} \sqrt{\frac{2\nu! D_{T_b} Le^\nu}{\beta^{\nu+1} \tau_{rb}}}, \quad U_b = \sqrt{\frac{2\nu! D_{T_b} Le^\nu}{\beta^{\nu+1} \tau_{rb}}}. \quad (2.105)$$



## Chapter 3

# The spectral difference method

### Sommaire

---

<b>3.1 The one-dimensional spectral difference scheme . . . . .</b>	<b>40</b>
3.1.1 Interpolation inside the element . . . . .	41
3.1.2 The Riemann solver of Roe . . . . .	43
3.1.3 Time marching . . . . .	46
3.1.4 Shock capturing . . . . .	47
3.1.5 Scalar limiter . . . . .	49
<b>3.2 Moving reference frame . . . . .</b>	<b>49</b>
3.2.1 Conservation equations . . . . .	50
3.2.2 Modification to the Roe solver . . . . .	51
3.2.3 Boundary conditions on the moving piston . . . . .	52
<b>3.3 Flame stabilization . . . . .</b>	<b>53</b>

---

In the current work, the compressible reactive Navier-Stokes equations in (2.1) are solved numerically using the high-order spectral difference (SD) method [35, 37, 51]. The SD scheme allows an arbitrary order of accuracy with a compact stencil on unstructured meshes, and provides a fine resolution of the flow with minimal numerical dissipation. In this chapter, we present the details of the SD numerical scheme. Since our work is mainly focused on one-dimensional simulations, only the one-dimensional scheme is presented. Generalization to multiple dimensions is relatively straightforward, and it can be found in dedicated studies [35, 51].

### 3.1 The one-dimensional spectral difference scheme

The computational domain is divided into a series of cells, called elements (Figure 3.1). The solution is represented over each element by a high-order polynomial. These interpolation polynomials are usually discontinuous between neighboring elements, but the flux is made continuous using a Riemann solver at the cell boundary in order to ensure conservation. These points are elaborated in the following sections.

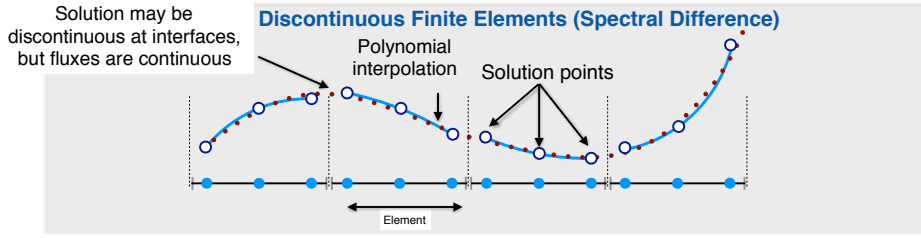


Figure 3.1: The spectral difference scheme.

### 3.1.1 Interpolation inside the element

To achieve an efficient implementation of the solution method, each element in physical space is transformed into a standard element in the computational space described by the local coordinate  $\xi \in [-1, 1]$ , as illustrated in Figure 3.2. The relevant coordinate transformation is formalized using shape functions as

$$x(\xi) = \frac{1}{2}(1 - \xi)x_L^k + \frac{1}{2}(1 + \xi)x_R^k \quad (3.1)$$

where  $x$  is the physical space coordinate and  $x_L^k$  and  $x_R^k$  are the two values of  $x$  defining the boundaries of the  $k$ -th element.

The governing equations (2.1) are then transferred into the computational space, in which they take the form

$$\frac{\partial \mathbf{Q}}{\partial t} + \frac{\partial \mathbf{G}}{\partial \xi} = \mathbf{H} \quad (3.2)$$

where

$$\mathbf{Q} \equiv \frac{h^k}{2} \mathbf{U}, \quad \mathbf{G} \equiv \mathbf{F}, \quad \mathbf{H} \equiv \frac{h^k}{2} \mathbf{S} \quad (3.3)$$

where  $h^k \equiv x_R^k - x_L^k$  is the size of the  $k$ -th element.

Two sets of points are defined within each standard element: the solution points and flux points, as illustrated in Figure 3.2. In order to construct an interpolating polynomial for the solution of order  $n - 1$ ,  $n$  solution points are needed. These points are chosen to be the Gauss-Legendre quadrature points in the interval  $[-1, 1]$ . The flux points, in turn, are chosen as the quadrature points of order  $n - 1$  plus the two end points  $\xi = -1$  and  $\xi = 1$ . Therefore, the  $n$  solution points are obtained as the roots of the Legendre polynomial

$$P_n(\xi) = \frac{2n - 1}{n} \xi P_{n-1}(\xi) - \frac{n - 1}{n} P_{n-2}(\xi) \quad (3.4)$$

$$P_0(\xi) = 1 \quad (3.5)$$

$$P_{-1}(\xi) = 0. \quad (3.6)$$

Let the index  $i$  denote solution points and  $i + 1/2$  denote flux points. From the  $n$  solution points and  $n + 1$  flux points, interpolation polynomials of degree  $n - 1$  and  $n$  respectively can be constructed using

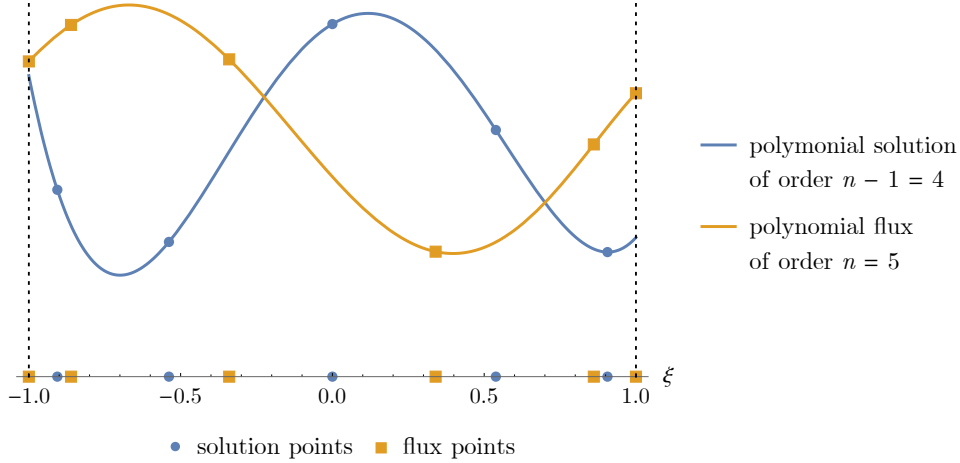


Figure 3.2: Schematic representation of the solution and flux polynomials in a standard element for a solution of order  $n = 5$ .

the Lagrange polynomial bases defined as

$$l_i(\xi) = \prod_{\substack{s=1 \\ s \neq i}}^n \left( \frac{\xi - \xi_s}{\xi_i - \xi_s} \right) \quad (3.7)$$

$$l_{i+1/2}(\xi) = \prod_{\substack{s=0 \\ s \neq i}}^n \left( \frac{\xi - \xi_{s+1/2}}{\xi_{i+1/2} - \xi_{s+1/2}} \right). \quad (3.8)$$

The solution vector  $\mathbf{U}$  is then obtained as the linear combination

$$\mathbf{U}(\xi) = \sum_{i=1}^n 2 \frac{\mathbf{Q}_i}{h^k} l_i(\xi). \quad (3.9)$$

$\mathbf{U}$  is then used to compute the flux vector  $\mathbf{F}$  at the flux points, from which the numerical flux vector  $\mathbf{G}$  is then reconstructed as

$$\mathbf{G}(\xi) = \sum_{i=0}^n \mathbf{F}_{i+1/2} l_{i+1/2}(\xi). \quad (3.10)$$

The reconstructed flux is element-wise continuous, but is discontinuous at the cell interfaces. A common flux needs to be computed at the interface to ensure conservation and stability. To that end, advective and viscous fluxes are treated separately. A Riemann solver is used to compute a common advective flux at the interface. A Roe solver with entropy fix is adopted in the current study (see 3.1.2). The viscous flux is made continuous by simply computing it as a function of the average interface solution and solution gradients [52].

Then, the reconstructed flux is made continuous across the elements by replacing the interface fluxes  $\mathbf{F}_{1/2}$  and  $\mathbf{F}_{n+1/2}$  by the common flux values at the left and right interfaces  $\mathbf{F}_L^C$  and  $\mathbf{F}_R^C$ , so that the continuous flux would be given as

$$\mathbf{G}^C(\xi) = \mathbf{F}_L^C l_{1/2}(\xi) + \mathbf{F}_R^C l_{n+1/2}(\xi) + \sum_{i=1}^{n-1} \mathbf{F}_{i+1/2} l_{i+1/2}(\xi). \quad (3.11)$$

The relevant derivative of  $\mathbf{G}^C$  with respect to  $\xi$  (of degree  $n - 1$ ) is readily obtained as

$$\frac{\partial \mathbf{G}^C(\xi)}{\partial \xi} = \mathbf{F}_L^C \frac{dl_{1/2}(\xi)}{d\xi} + \mathbf{F}_R^C \frac{dl_{n+1/2}(\xi)}{d\xi} + \sum_{i=1}^{n-1} \mathbf{F}_{i+1/2} \frac{dl_{i+1/2}(\xi)}{d\xi} \quad (3.12)$$

which can be evaluated at the solution points

$$\frac{\partial \mathbf{G}_i^C}{\partial \xi} = \left. \frac{\partial \mathbf{G}^C(\xi)}{\partial \xi} \right|_{\xi=\xi_i}, \quad (3.13)$$

therefore allowing for time marching.

### 3.1.2 The Riemann solver of Roe

To obtain the advective flux at the cell interface, the Riemann problem is solved using the approximate Roe solver [53, 54]. Viscous fluxes and source terms are neglected, and equations (2.1) reduce to the Euler equations (with a scalar transport equation):

$$\frac{\partial \mathbf{U}}{\partial t} + \frac{\partial \mathbf{F}}{\partial x} = \mathbf{0}, \quad (3.14)$$

where  $\mathbf{F} = \mathbf{F}_a$  is the advective flux in equation (2.2). Equations (3.14) have to be solved at the cell interface  $x = 0$  in Figure 3.3 to obtain the intermediate flux. The initial conditions  $\mathbf{U}_L$  for  $x < 0$  and  $\mathbf{U}_R$  for  $x > 0$  are known.

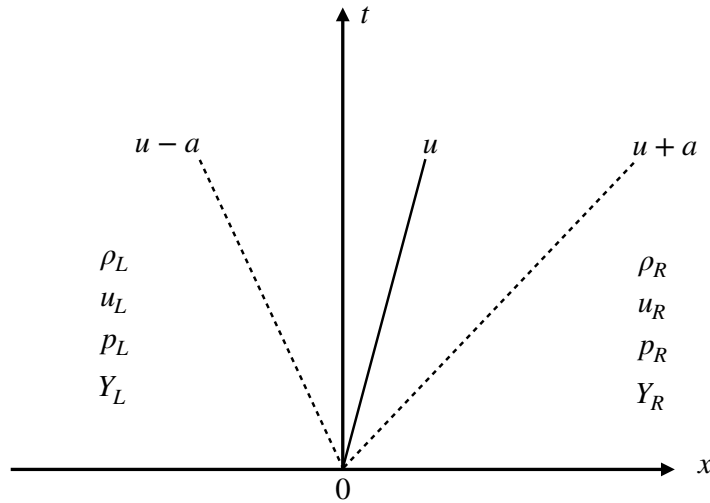


Figure 3.3: Sketch of the Riemann problem to be solved at the cell interface.

To proceed, we first define the flux Jacobian  $\mathbf{A}(\mathbf{U})$  as

$$\mathbf{A}(\mathbf{U}) \equiv \frac{\partial \mathbf{F}}{\partial \mathbf{U}}, \quad (3.15)$$

then using the chain rule, equations (3.14) are written as

$$\frac{\partial \mathbf{U}}{\partial t} + \mathbf{A}(\mathbf{U}) \frac{\partial \mathbf{U}}{\partial x} = \mathbf{0}. \quad (3.16)$$

Roe's method to solving the Riemann problem relies on replacing the Jacobian  $\mathbf{A}(\mathbf{U})$  with a constant Jacobian  $\tilde{\mathbf{A}}(\mathbf{U}_L, \mathbf{U}_R)$ , thus making equation (3.16) linear in  $\mathbf{U}$ . The Riemann problem then simplifies into

$$\frac{\partial \mathbf{U}}{\partial t} + \tilde{\mathbf{A}}(\mathbf{U}) \frac{\partial \mathbf{U}}{\partial x} = \mathbf{0}, \quad (3.17)$$

with initial conditions

$$\mathbf{U}(x, 0) = \mathbf{U}_L \quad \text{for } x < 0, \quad (3.18)$$

$$\mathbf{U}(x, 0) = \mathbf{U}_R \quad \text{for } x > 0. \quad (3.19)$$

The approximate Jacobian  $\tilde{\mathbf{A}}$  needs to satisfy the following three properties:

- It needs to be hyperbolic, meaning that it has a complete set of real eigenvalues

$$\tilde{\lambda}_i = \tilde{\lambda}_i(\mathbf{U}_L, \mathbf{U}_R) \in \mathbb{R}, \quad (3.20)$$

and a complete set of linearly independent eigenvectors  $\tilde{\mathbf{K}}_i$ .

- It needs to be consistent with the exact Jacobian, meaning that

$$\tilde{\mathbf{A}}(\mathbf{U}, \mathbf{U}) = \mathbf{A}(\mathbf{U}). \quad (3.21)$$

- It needs to ensure conservation across discontinuities:

$$\mathbf{F}(\mathbf{U}_R) - \mathbf{F}(\mathbf{U}_L) = \tilde{\mathbf{A}}(\mathbf{U}_R - \mathbf{U}_L). \quad (3.22)$$

If the Jacobian  $\tilde{\mathbf{A}}$ , its eigenvalues  $\tilde{\lambda}_i$  and eigenvectors  $\tilde{\mathbf{K}}_i$  are known, then the intermediate flux at  $x = 0$  can be computed as [54]

$$\mathbf{F}^C = \mathbf{F}(x = 0, t) = \frac{1}{2}(\mathbf{F}_L + \mathbf{F}_R) - \frac{1}{2} \sum_{i=1}^4 \tilde{\alpha}_i \left| \tilde{\lambda}_i \right| \tilde{\mathbf{K}}_i, \quad (3.23)$$

where the coefficients  $\tilde{\alpha}_i$  are the projections of the jump in  $\mathbf{U}$  on the eigenvectors  $\tilde{\mathbf{K}}_i$ :

$$\Delta \mathbf{U} \equiv \mathbf{U}_R - \mathbf{U}_L = \sum_{i=1}^4 \tilde{\alpha}_i \tilde{\mathbf{K}}_i. \quad (3.24)$$

In the following section, we see how to compute  $\tilde{\mathbf{A}}$  and thus its eigenvalues and eigenvectors.

### 3.1.2.1 Calculation of $\tilde{\mathbf{A}}$

The exact Jacobian  $\mathbf{A}$  of equations (3.14) is given by

$$\mathbf{A} = \begin{pmatrix} 0 & 1 & 0 & 0 \\ (\gamma - 1)H - u^2 - a^2 & (3 - \gamma)u & \gamma - 1 & 0 \\ u(\gamma - 2)H - ua^2 & H - (\gamma - 1)u^2 & \gamma u & 0 \\ -uY & Y & 0 & u \end{pmatrix}, \quad (3.25)$$

where  $a$  is the speed of sound and  $H \equiv E + \frac{p}{\rho}$  is the total enthalpy per unit mass. The eigenvalues of  $\mathbf{A}$  are found to be

$$\lambda_1 = u, \quad \lambda_2 = u - a, \quad \lambda_3 = u + a, \quad \lambda_4 = u, \quad (3.26)$$

where  $u$  is an eigenvalue with a multiplicity of two. A set of corresponding eigenvectors is

$$\mathbf{K}_1 = \begin{pmatrix} 1 \\ u \\ \frac{u^2}{2} \\ 0 \end{pmatrix}, \quad \mathbf{K}_2 = \begin{pmatrix} 1 \\ u - a \\ H - au \\ Y \end{pmatrix}, \quad \mathbf{K}_3 = \begin{pmatrix} 1 \\ u + a \\ H + au \\ Y \end{pmatrix}, \quad \mathbf{K}_4 = \begin{pmatrix} 0 \\ 0 \\ 0 \\ 1 \end{pmatrix}. \quad (3.27)$$

We would like to find an approximate Jacobian  $\tilde{\mathbf{A}}$  that satisfies the three conditions listed above (hyperbolicity, consistency and conservation). To do that, following the approach of Roe [53], we begin by defining the parameter vector  $\mathbf{P}$  as

$$\mathbf{P} = \mathbf{P}(\mathbf{U}) \equiv \sqrt{\rho} \begin{pmatrix} 1 \\ u \\ H \\ Y \end{pmatrix} = \begin{pmatrix} p_1 \\ p_2 \\ p_3 \\ p_4 \end{pmatrix}, \quad (3.28)$$

and we define the averaged parameter vector  $\tilde{\mathbf{P}}$  as

$$\tilde{\mathbf{P}} = \frac{1}{2} (\mathbf{P}_L + \mathbf{P}_R) = \frac{1}{2} \begin{pmatrix} \sqrt{\rho_L} + \sqrt{\rho_R} \\ \sqrt{\rho_L} u_L + \sqrt{\rho_R} u_R \\ \sqrt{\rho_L} H_L + \sqrt{\rho_R} H_R \\ \sqrt{\rho_L} Y_L + \sqrt{\rho_R} Y_R \end{pmatrix} = \begin{pmatrix} \tilde{p}_1 \\ \tilde{p}_2 \\ \tilde{p}_3 \\ \tilde{p}_4 \end{pmatrix}. \quad (3.29)$$

We then define the two matrices  $\tilde{\mathbf{B}}(\tilde{\mathbf{P}})$  and  $\tilde{\mathbf{C}}(\tilde{\mathbf{P}})$  as

$$\Delta \mathbf{U} \equiv \tilde{\mathbf{B}} \Delta \mathbf{P}, \quad \Delta \mathbf{F} \equiv \tilde{\mathbf{C}} \Delta \mathbf{P}. \quad (3.30)$$

Equations (3.30) can be combined to give

$$\Delta \mathbf{F} = \tilde{\mathbf{C}} \tilde{\mathbf{B}}^{-1} \Delta \mathbf{U} \quad (3.31)$$

which when compared to (3.22) gives

$$\tilde{\mathbf{A}} = \tilde{\mathbf{C}} \tilde{\mathbf{B}}^{-1}, \quad (3.32)$$

and the conservation condition is satisfied automatically. Matrices  $\tilde{\mathbf{B}}$  and  $\tilde{\mathbf{C}}$  that satisfy equations (3.30) are found to be

$$\tilde{\mathbf{B}} = \begin{pmatrix} 2\tilde{p}_1 & 0 & 0 & 0 \\ \tilde{p}_2 & \tilde{p}_1 & 0 & 0 \\ \frac{\tilde{p}_3}{\gamma} & \left(\frac{\gamma-1}{\gamma}\right)\tilde{p}_2 & \frac{\tilde{p}_1}{\gamma} & 0 \\ \tilde{p}_4 & 0 & 0 & \tilde{p}_1 \end{pmatrix}, \quad \tilde{\mathbf{C}} = \begin{pmatrix} \tilde{p}_2 & \tilde{p}_1 & 0 & 0 \\ \left(\frac{\gamma-1}{\gamma}\right)\tilde{p}_3 & \left(\frac{\gamma+1}{\gamma}\right)\tilde{p}_2 & \left(\frac{\gamma-1}{\gamma}\right)\tilde{p}_1 & 0 \\ 0 & \tilde{p}_3 & \tilde{p}_2 & 0 \\ 0 & \tilde{p}_4 & 0 & \tilde{p}_2 \end{pmatrix}, \quad (3.33)$$

then equation (3.32) gives  $\tilde{\mathbf{A}}$  as

$$\tilde{\mathbf{A}} = \begin{pmatrix} 0 & 1 & 0 & 0 \\ (\gamma-1)\tilde{H} - \tilde{u}^2 - \tilde{a}^2 & (3-\gamma)\tilde{u} & \gamma-1 & 0 \\ \tilde{u}(\gamma-2)\tilde{H} - \tilde{u}\tilde{a}^2 & \tilde{H} - (\gamma-1)\tilde{u}^2 & \gamma\tilde{u} & 0 \\ -\tilde{u}\tilde{Y} & \tilde{Y} & 0 & \tilde{u} \end{pmatrix}, \quad (3.34)$$

where we have defined the following *Roe-averaged* quantities

$$\tilde{u} \equiv \frac{\sqrt{\rho_L}u_L + \sqrt{\rho_R}u_R}{\sqrt{\rho_L} + \sqrt{\rho_R}}, \quad (3.35)$$

$$\tilde{H} \equiv \frac{\sqrt{\rho_L}H_L + \sqrt{\rho_R}H_R}{\sqrt{\rho_L} + \sqrt{\rho_R}}, \quad (3.36)$$

$$\tilde{Y} \equiv \frac{\sqrt{\rho_L}Y_L + \sqrt{\rho_R}Y_R}{\sqrt{\rho_L} + \sqrt{\rho_R}}, \quad (3.37)$$

$$\tilde{a} \equiv \sqrt{(\gamma - 1) \left( \tilde{H} - \frac{\tilde{u}^2}{2} \right)}. \quad (3.38)$$

Now that we have the approximate Jacobian, we can proceed to calculate the intermediate flux.

### 3.1.2.2 Calculation of the intermediate flux

Comparing equations (3.34) and (3.25), we can directly deduce the eigenvalues and eigenvectors of  $\tilde{\mathbf{A}}$  as

$$\tilde{\lambda}_1 = \tilde{u}, \quad \tilde{\lambda}_2 = \tilde{u} - \tilde{a}, \quad \tilde{\lambda}_3 = \tilde{u} + \tilde{a}, \quad \tilde{\lambda}_4 = \tilde{u}, \quad (3.39)$$

and

$$\tilde{\mathbf{K}}_1 = \begin{pmatrix} 1 \\ \tilde{u} \\ \frac{\tilde{u}^2}{2} \\ 0 \end{pmatrix}, \quad \tilde{\mathbf{K}}_2 = \begin{pmatrix} 1 \\ \tilde{u} - \tilde{a} \\ \tilde{H} - \tilde{a}\tilde{u} \\ \tilde{Y} \end{pmatrix}, \quad \tilde{\mathbf{K}}_3 = \begin{pmatrix} 1 \\ \tilde{u} + \tilde{a} \\ \tilde{H} + \tilde{a}\tilde{u} \\ \tilde{Y} \end{pmatrix}, \quad \tilde{\mathbf{K}}_4 = \begin{pmatrix} 0 \\ 0 \\ 0 \\ 1 \end{pmatrix}. \quad (3.40)$$

The coefficients  $\tilde{\alpha}_i$  are obtained from equation (3.24) as

$$\tilde{\alpha}_1 = \frac{\gamma - 1}{\tilde{a}^2} \left[ (\tilde{H} - \tilde{u}^2) \Delta u_1 + \tilde{u} \Delta u_2 - \Delta u_3 \right] \quad (3.41)$$

$$\tilde{\alpha}_2 = \frac{1}{2\tilde{a}} [(\tilde{u} + \tilde{a}) \Delta u_1 - \Delta u_2 - \tilde{a}\tilde{\alpha}_1] \quad (3.42)$$

$$\tilde{\alpha}_3 = \Delta u_1 - (\tilde{\alpha}_1 + \tilde{\alpha}_2) \quad (3.43)$$

$$\tilde{\alpha}_4 = \Delta u_4 - (\tilde{\alpha}_2 + \tilde{\alpha}_3) \tilde{Y}, \quad (3.44)$$

where  $\Delta u_i$  is the  $i$ -th component of  $\Delta \mathbf{U}$ . Therefore, to compute the intermediate flux  $\mathbf{F}(x = 0, t)$ , one first calculates the Roe-averaged quantities in equations (3.35-3.38), then uses these quantities to compute the eigenvalues and eigenvectors in equations (3.39) and (3.40) respectively and the coefficients in equations (3.41-3.44). Finally, one plugs everything into equation (3.23) to obtain the intermediate flux.

### 3.1.3 Time marching

After flux gradients are computed, time integration is performed using the Runge-Kutta method. In particular, the fourth-order, five-stages, strong stability preserving (RK45-SSP) scheme is adopted in the current study [55]. The Navier-Stokes equations (2.1) are first rewritten as

$$\frac{\partial \mathbf{U}}{\partial t} = \mathbf{S}(\mathbf{U}, t) - \frac{\partial \mathbf{F}(\mathbf{U}, t)}{\partial x} \equiv \mathcal{L}(\mathbf{U}, t) \quad (3.45)$$

where  $\mathcal{L}$  is the residual. The equations are then discretized in time according to the following scheme [31, 55]:

$$\begin{aligned}
\mathbf{V}_1 &= \mathbf{U}_n + 0.39175222700392\Delta t\mathcal{L}(\mathbf{U}_n, t_n) \\
\mathbf{V}_2 &= 0.44437049406734\mathbf{U}_n + 0.55562950593266\mathbf{V}_1 \\
&\quad + 0.36841059262959\Delta t\mathcal{L}(\mathbf{V}_1, t_n + 0.39175222700392\Delta t) \\
\mathbf{V}_3 &= 0.62010185138540\mathbf{U}_n + 0.37989814861460\mathbf{V}_2 \\
&\quad + 0.25189177424738\Delta t\mathcal{L}(\mathbf{V}_2, t_n + 0.58607968896780\Delta t) \\
\mathbf{V}_4 &= 0.17807995410773\mathbf{U}_n + 0.82192004589227\mathbf{V}_3 \\
&\quad + 0.54497475021237\Delta t\mathcal{L}(\mathbf{V}_3, t_n + 0.47454236302687\Delta t) \\
\mathbf{U}_{n+1} &= 0.00683325884039\mathbf{U}_n + 0.51723167208978\mathbf{V}_2 \\
&\quad + 0.12759831133288\mathbf{V}_3 + 0.34833675773694\mathbf{V}_4 \\
&\quad + 0.08460416338212\Delta t\mathcal{L}(\mathbf{V}_3, t_n + 0.47454236302687\Delta t) \\
&\quad + 0.22600748319395\Delta t\mathcal{L}(\mathbf{V}_4, t_n + 0.93501063100924\Delta t)
\end{aligned}$$

where  $\mathbf{U}_n$  is the solution vector at time step  $t_n$ . This strong-stability-preserving scheme allows for a high-order time resolution of the flow, while also reducing computational cost by permitting time steps 50% larger than a forward Euler method.

The maximum time step is set to satisfy Courant-Friedrichs-Lewy (CFL) and Fourier (FOU) conditions for advective and viscous fluxes respectively. The maximum time step is computed as the minimum value within the computational domain of

$$\Delta t = \frac{1}{\Delta t_{CFL}^{-1} + \Delta t_{FOU}^{-1}} \quad (3.46)$$

where  $\Delta t_{CFL}$  and  $\Delta t_{FOU}$  are defined as

$$\Delta t_{CFL} = \alpha_{CFL} \frac{\xi_{s1} h}{\lambda_m} \quad \Delta t_{FOU} = \alpha_{FOU} \frac{(\xi_{f2} h)^2}{2\nu_{tot}} \quad (3.47)$$

where  $h$  is the element width,  $\xi_{s1}$  and  $\xi_{f2}$  represent the smallest distance of solution and flux points, respectively to the element boundary,  $\lambda_m \equiv |u| + a$  is the spectral radius (maximum eigenvalue) of the flux Jacobian, and  $\nu_{tot}$  is the total kinetic viscosity coming from molecular viscosity and also the artificial viscosity from the shock capturing method (see §3.1.4). The coefficients  $\alpha_{CFL}$  and  $\alpha_{FOU}$  set the margin of the time step to the relevant estimated limit of stability.

### 3.1.4 Shock capturing

Although shock capturing procedures based on physical viscosity have been shown to better preserve flow properties across shock discontinuities [56], a Laplacian-based approach is adopted in the current work due to its better robustness. Accordingly, equation (2.1) is augmented with a Laplacian diffusion term,

$$\frac{\partial \mathbf{U}}{\partial t} + \frac{\partial \mathbf{F}}{\partial x} = \frac{\partial}{\partial x} \left( \varepsilon \frac{\partial \mathbf{U}}{\partial x} \right) + \mathbf{S} \quad (3.48)$$

where  $\varepsilon$  is the artificial viscosity (AV) introduced in under-resolved regions of the flow. In order to sense under-resolved regions, the level of smoothness of a selected flow variable  $\psi$ , hereafter referred to as the

sensor variable, is measured by calculating the rate of decay of its modal coefficients in an orthogonal polynomial basis. In our study, normalized Legendre polynomials are used as the basis of choice, and the sensor variable is written as

$$\psi(\xi) = \sum_{i=1}^n \hat{\psi}_i P_{i-1}^*(\xi), \quad (3.49)$$

where  $n$  is the order of the simulation,  $P_i^*(\xi)$  is the  $i$ -th degree normalized Legendre polynomial,

$$P_i^*(\xi) = P_i(\xi) \sqrt{\frac{2i+1}{2}}, \quad (3.50)$$

and the  $\hat{\psi}_i$ s are the modes of the sensor variable, which can be obtained from its nodal values by multiplication with the inverse Vandermonde matrix constructed using the selected polynomial basis. We introduce the truncated expansion

$$\bar{\psi}(\xi) = \sum_{i=1}^{n-1} \hat{\psi}_i P_{i-1}^*(\xi), \quad (3.51)$$

and the sensor parameter is then defined for each element as

$$s_e(\psi) = \log \left[ \frac{\langle \psi - \bar{\psi}, \psi - \bar{\psi} \rangle_e}{\langle \psi, \psi \rangle_e} \right], \quad (3.52)$$

where  $\langle \cdot, \cdot \rangle_e$  is the  $L^2$  inner product in the element. Orthonormality of the  $P_i^*$ s leads to simplified expressions for the inner products in equation (3.52),

$$\langle \psi - \bar{\psi}, \psi - \bar{\psi} \rangle_e = \int_{-1}^1 \hat{\psi}_n^2 P_{n-1}^*(\xi) P_{n-1}^*(\xi) d\xi = \hat{\psi}_n^2, \quad (3.53)$$

$$\langle \psi, \psi \rangle_e = \int_{-1}^1 \sum_{i=1}^n \sum_{j=1}^n \hat{\psi}_i \hat{\psi}_j P_{i-1}^*(\xi) P_{j-1}^*(\xi) d\xi = \sum_{i=1}^n \hat{\psi}_i^2. \quad (3.54)$$

The artificial viscosity is then calculated as

$$\varepsilon_e = \begin{cases} 0 & \text{for } s_e < s_0 - \kappa \\ \frac{\varepsilon_0}{2} \left[ 1 + \sin \frac{\pi(s_e - s_0)}{2\kappa} \right] & \text{for } s_0 - \kappa \leq s_e \leq s_0 + \kappa \\ \varepsilon_0 & \text{for } s_e > s_0 + \kappa \end{cases} \quad (3.55)$$

where  $\varepsilon_0$ ,  $s_0$  and  $\kappa$  are fixed parameters to be determined empirically. In our study,  $\varepsilon_0$  is calculated using the spectral radius and the element width as

$$\varepsilon_0 = C_\varepsilon \frac{\lambda_m h}{n-1}, \quad (3.56)$$

where  $C_\varepsilon$  is an additional parameter commonly set to unity.

The threshold  $s_0$  and sensor tolerance  $\kappa$  are computed via a self calibration algorithm which determines the optimal values for these parameters for an arbitrary value of the order  $n$  with the use of a manufactured solution  $\psi_{\text{m.f.}}(\xi)$ . In particular,  $s_0$  is calculated based on the value of the sensor when a relatively sharp hyperbolic tangent profile is assumed for the solution, such that the nodal values are given by

$$\psi_{\text{m.f.}}(\xi_i) = \frac{1}{2} \left\{ 1 + \tanh \left[ \frac{\text{tr}(i-1-n/2) + 1/2}{(n-1)/5} \right] \right\}, \quad i \in \{1, 2, \dots, n\} \quad (3.57)$$

where  $\text{tr}(\cdot)$  denotes the truncation to the lower integer, and is used to prevent the manufactured solution from being perfectly centered for odd values of  $n$ , and the threshold  $s_0$  from being too low in the case of low-order computations. Optimal values for  $s_0$  and  $\kappa$  have been found to be

$$s_0 = s_{\text{m.f.}} - 3, \quad \text{and} \quad \kappa = 1, \quad (3.58)$$

where  $s_{\text{m.f.}}$  is the value of the sensor for the manufactured solution, computed from equation (3.52).

In the present work, a compound sensor is adopted, making use of the density and acoustic characteristics (variables transported along  $u + a$  and  $u - a$ ) as the sensor variables [57]. Sensor values for the three variables are evaluated using equation (3.52), and the compound sensor is then evaluated as

$$s^{\text{ac}\rho} = \max(s^\rho, s^{u+a}, s^{u-a}), \quad (3.59)$$

in order to pick the most poorly resolved signal of the three. Artificial viscosity is then calculated for the element using equation (3.55). Finally, artificial viscosity is made  $C^0$  continuous across elements by linear interpolation of the common values of  $\varepsilon$  evaluated at element interfaces as was suggested by [58].

### 3.1.5 Scalar limiter

High-order methods are known to promote boundedness issues with scalar fields. Here, to secure perfect scalar boundedness, i.e.  $Y \in [0, 1]$ , a modified implementation of the positivity-preserving scheme introduced by Zhang & Shu [59] is adopted.<sup>1</sup>

Let the lower and upper bounds of  $Y$  be denoted as  $B_L = \epsilon_Y$  and  $B_U = 1 - \epsilon_Y$  respectively, where  $\epsilon_Y$  is a small number (for instance,  $\epsilon_Y = 10^{-13}$ ). Then, at each stage of the Runge-Kutta time-stepping process, we can define the parameter  $\theta_Y$  over a standard element (computational cell) as

$$\theta_Y = \min \left( 1, \frac{\bar{Y} - B_L}{\bar{Y} - Y_{\min}}, \frac{B_U - \bar{Y}}{Y_{\max} - \bar{Y}} \right), \quad (3.60)$$

where  $\bar{Y}$  is the mean value of  $Y$  inside the element, and  $Y_{\min}$  and  $Y_{\max}$  are the minimum and maximum values of  $Y$  in the element respectively. The corrected value of  $Y$  is then calculated as

$$\hat{Y} = \theta_Y(Y - \bar{Y}) + \bar{Y}, \quad (3.61)$$

which will always be between  $B_L$  and  $B_U$  provided that  $\bar{Y}$  is so.

It should be noted that we had to resort to limiting the non-conservative variable  $Y$  due to the limiting problem being ill-defined for the conservative variable  $\rho Y$  in the current implementation. As a consequence, the mean value of  $\rho Y$  will not be perfectly preserved over the element if  $\rho$  is not constant, and the limiter will act as a scalar source term. In practice, however, the contribution of this source term stays negligible (In the simulations carried out it represents on average around 0.021% of the total mass of a fluid element) and does not affect the overall quality of the solution.

## 3.2 Moving reference frame

In Chapter 5, we shall solve the inviscid and inert Navier-Stokes equations (also called inert Euler equations) in a reference frame of a piston moving with a variable velocity  $U_p(t)$ , as illustrated in Figure 3.4. In the following, we present the changes which need to be accounted for in the numerical solution of these equations.

<sup>1</sup>. Note that the high-order dissipation term is not triggered outside of the leading shock, therefore the reaction zone and the progress variable profile are free from additional dissipation.



Figure 3.4: Sketch of a one-dimensional inert, inviscid flow pushed by a moving piston.

### 3.2.1 Conservation equations

The material derivative is expressed in the piston's reference frame:

$$\frac{D}{Dt} = \frac{\partial}{\partial t} + (u - U_p) \frac{\partial}{\partial x}, \quad (3.62)$$

where  $u$  is the flow velocity in the lab frame. The inert Euler equations are thus written in non-conservative form as

$$\left[ \frac{\partial}{\partial t} + (u - U_p) \frac{\partial}{\partial x} \right] \rho = -\rho \frac{\partial u}{\partial x} \quad (3.63)$$

$$\left[ \frac{\partial}{\partial t} + (u - U_p) \frac{\partial}{\partial x} \right] u = -\frac{1}{\rho} \frac{\partial p}{\partial x} \quad (3.64)$$

$$\left[ \frac{\partial}{\partial t} + (u - U_p) \frac{\partial}{\partial x} \right] e = -\frac{p}{\rho} \frac{\partial u}{\partial x}. \quad (3.65)$$

where  $e$  is the internal energy per unit mass. When transformed into conservative form, the equations read

$$\frac{\partial \rho}{\partial t} + \frac{\partial \rho(u - U_p)}{\partial x} = 0 \quad (3.66)$$

$$\frac{\partial \rho u}{\partial t} + \frac{\partial}{\partial x} [\rho u(u - U_p) + p] = 0 \quad (3.67)$$

$$\frac{\partial \rho E}{\partial t} + \frac{\partial}{\partial x} [\rho E(u - U_p) + up] = 0, \quad (3.68)$$

where  $E = e + \frac{1}{2}u^2$  is the total energy per unit mass in the lab frame. Thus, we have

$$\mathbf{U} = \begin{pmatrix} \rho \\ \rho u \\ \rho E \end{pmatrix}, \quad \mathbf{F} = \begin{pmatrix} \rho(u - U_p) \\ \rho u(u - U_p) + p \\ \rho E(u - U_p) + up \end{pmatrix}. \quad (3.69)$$

Equations (3.66-3.68) can be readily solved using the SD method discussed in the previous section. However, the fact that the advective flux  $\mathbf{F}$  has changed while  $\mathbf{U}$  has remained the same as in (2.2) implies that Roe's Riemann solver needs to be changed when solving equations (3.66-3.68). This is discussed in the following section.

### 3.2.2 Modification to the Roe solver

Let's define the vectors  $\mathbf{U}_o$  and  $\mathbf{F}_o$  to be respectively the vector of conservative variables and the flux vector as given in the lab frame:

$$\mathbf{U}_o = \begin{pmatrix} \rho \\ \rho u \\ \rho E \end{pmatrix}, \quad \mathbf{F}_o = \begin{pmatrix} \rho u \\ \rho u^2 + p \\ \rho u E + up \end{pmatrix}, \quad (3.70)$$

Then,  $\mathbf{U}$  and  $\mathbf{F}$  in equation (3.69) can be written as

$$\mathbf{U} = \mathbf{U}_o, \quad \mathbf{F} = \mathbf{F}_o - U_p \mathbf{U}_o. \quad (3.71)$$

We want to solve the Riemann problem at the interface discontinuity of two cells and obtain the intermediate flux at the interface. As before, let's denote by  $\mathbf{U}_R$  and  $\mathbf{F}_R$  the solution and flux vectors to the right of the discontinuity and  $\mathbf{U}_L$  and  $\mathbf{F}_L$  those to the left. Then, the jumps across the discontinuity are given by

$$\Delta \mathbf{U} = \Delta \mathbf{U}_o, \quad \Delta \mathbf{F} = \Delta \mathbf{F}_o - U_p \Delta \mathbf{U}_o. \quad (3.72)$$

Again we choose the parameter vector to be

$$\mathbf{P} = \sqrt{\rho} \begin{pmatrix} 1 \\ u \\ H \end{pmatrix}, \quad (3.73)$$

and we define the two matrices  $\tilde{\mathbf{B}}$  and  $\tilde{\mathbf{C}}$  as

$$\Delta \mathbf{U} \equiv \tilde{\mathbf{B}} \Delta \mathbf{P}, \quad \Delta \mathbf{F} \equiv \tilde{\mathbf{C}} \Delta \mathbf{P}. \quad (3.74)$$

Then, substituting equation (3.72) into equation (3.74), we get

$$\tilde{\mathbf{B}} = \tilde{\mathbf{B}}_o, \quad \tilde{\mathbf{C}} = \tilde{\mathbf{C}}_o - U_p \tilde{\mathbf{B}}_o, \quad (3.75)$$

from which the flux Jacobian matrix is obtained as

$$\tilde{\mathbf{A}} = \tilde{\mathbf{C}} \tilde{\mathbf{B}}^{-1} \quad (3.76)$$

$$\tilde{\mathbf{A}} = \tilde{\mathbf{C}}_o \tilde{\mathbf{B}}_o^{-1} - U_p \tilde{\mathbf{B}}_o \tilde{\mathbf{B}}_o^{-1} \quad (3.77)$$

$$\tilde{\mathbf{A}} = \tilde{\mathbf{A}}_o - U_p \mathbf{I}. \quad (3.78)$$

Now, let  $\tilde{\mathbf{K}}_o^{(i)}$  be the  $i$ -th eigenvector of  $\tilde{\mathbf{A}}_o$  with an eigenvalue  $\tilde{\lambda}_{oi}$ , then

$$\tilde{\mathbf{A}} \tilde{\mathbf{K}}_o^{(i)} = \tilde{\mathbf{A}}_o \tilde{\mathbf{K}}_o^{(i)} - U_p \tilde{\mathbf{K}}_o^{(i)} \quad (3.79)$$

$$\tilde{\mathbf{A}} \tilde{\mathbf{K}}_o^{(i)} = (\tilde{\lambda}_{oi} - U_p) \tilde{\mathbf{K}}_o^{(i)}. \quad (3.80)$$

From equation (3.80), we can see that the eigenvectors of  $\tilde{\mathbf{A}}$  are the same as those of  $\tilde{\mathbf{A}}_o$ :

$$\tilde{\mathbf{K}}^{(i)} = \tilde{\mathbf{K}}_o^{(i)}, \quad (3.81)$$

and their eigenvalues are given by:

$$\tilde{\lambda}_i = \tilde{\lambda}_{oi} - U_p. \quad (3.82)$$

Equation (3.81) in addition to (3.72) ( $\Delta \mathbf{U} = \Delta \mathbf{U}_o$ ) imply that the projection coefficients are also the same as in the lab frame:

$$\tilde{\alpha}_i = \tilde{\alpha}_{oi}. \quad (3.83)$$

Therefore, the only change to the Roe solver is in the eigenvalues, as given by equation (3.82).

### 3.2.3 Boundary conditions on the moving piston

The boundary condition at the piston needs to be considered with care. The piston is considered to be an impermeable adiabatic wall. To obtain the advective flux on the boundary, we denote the flux point inside the domain by subscript  $L$  and we create a virtual flux point outside the domain denoted by  $R$ , at which the flow velocity is

$$u_R - U_p = -(u_L - U_p) \Rightarrow u_R = 2U_p - u_L \quad (3.84)$$

such that  $(u_L + u_R)/2 = U_p$ . Density and pressure are considered symmetric to those at point  $L$ :

$$\rho_R = \rho_L \quad (3.85)$$

$$p_R = p_L, \quad (3.86)$$

then we obtain the advective flux on the piston using the Roe solver discussed in the preceding section.

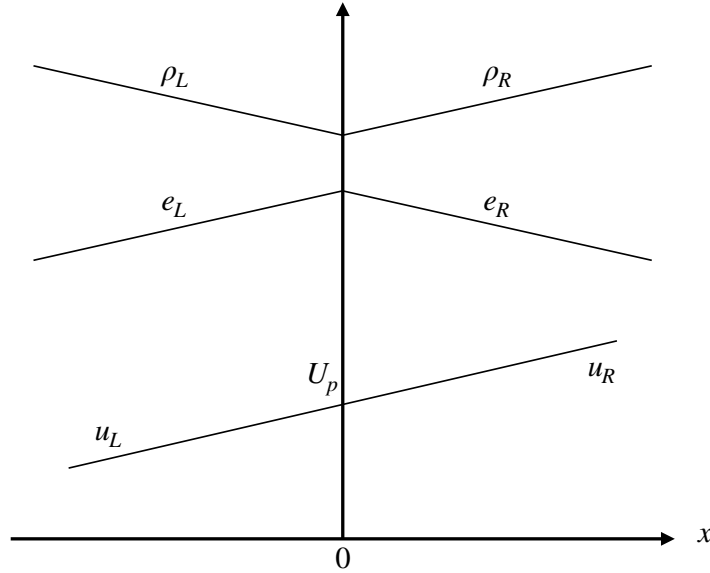


Figure 3.5: Sketch showing the variation of density, internal energy and velocity between physical  $L$  and ghost  $R$  cells at the piston boundary. Directions are flipped with respect to Figure 3.4, but this is only a matter of notation.

To evaluate viscous fluxes due to artificial viscosity (molecular viscosity is neglected), we need to know the gradients of conservative variables on the piston, since from equation (3.48):

$$\mathbf{F}_{AV} = \varepsilon \frac{\partial \mathbf{U}}{\partial x}. \quad (3.87)$$

To that end, we consider a ghost cell on the right-hand side of the interface with equal values of density and internal energy to the physical cell on the left, but reversed gradients, as illustrated in Figure 3.5:

$$\rho_R = \rho_L, \quad e_R = e_L, \quad (3.88)$$

$$\left( \frac{\partial \rho}{\partial x} \right)_R = - \left( \frac{\partial \rho}{\partial x} \right)_L, \quad \left( \frac{\partial e}{\partial x} \right)_R = - \left( \frac{\partial e}{\partial x} \right)_L, \quad (3.89)$$

so that the mean temperature gradient would be zero. Velocity is still considered to be symmetric with respect to the piston frame, and is thus given by:

$$u_R = 2U_p - u_L, \quad \left(\frac{\partial u}{\partial x}\right)_R = \left(\frac{\partial u}{\partial x}\right)_L. \quad (3.90)$$

We want to obtain the gradients for the conservative variables  $\rho$ ,  $\rho u$ , and  $\rho E$ . The density gradient is readily obtained in (3.89). For momentum, we have using the chain rule

$$\left(\frac{\partial \rho u}{\partial x}\right)_R = \rho_R \left(\frac{\partial u}{\partial x}\right)_R + u_R \left(\frac{\partial \rho}{\partial x}\right)_R, \quad (3.91)$$

which when using equations (3.88) through (3.90) reduces to

$$\left(\frac{\partial \rho u}{\partial x}\right)_R = \left(\frac{\partial \rho u}{\partial x}\right)_L - 2U_p \left(\frac{\partial \rho}{\partial x}\right)_L. \quad (3.92)$$

For total energy, we first write the gradient of internal energy as a function of conserved variables gradients:

$$\frac{\partial e}{\partial x} = \frac{1}{\rho} \left( \frac{\partial \rho E}{\partial x} - e \frac{\partial \rho}{\partial x} - u \frac{\partial \rho u}{\partial x} + \frac{1}{2} u^2 \frac{\partial \rho}{\partial x} \right), \quad (3.93)$$

and we substitute this into the second equation in (3.89):  $\left(\frac{\partial e}{\partial x}\right)_R = -\left(\frac{\partial e}{\partial x}\right)_L$ . Thus, we obtain an expression for the gradient of total energy, which reduces to

$$\left(\frac{\partial \rho E}{\partial x}\right)_R = U_p \left[ \left(\frac{\partial \rho u}{\partial x}\right)_R + \left(\frac{\partial \rho u}{\partial x}\right)_L \right] - \left(\frac{\partial \rho E}{\partial x}\right)_L. \quad (3.94)$$

Finally, viscous fluxes at the boundary are computed using the arithmetic average of left- and right-gradients.

### 3.3 Flame stabilization

A flame stabilization procedure has been implemented in the numerical code. Although this procedure is not utilized in the current study, it is still mentioned here for possible future reference.

We consider a one-dimensional flame propagating at a constant velocity in a combustible mixture in which inlet pressure and density are fixed (Figure 3.6). We want to simulate this flame in a reference frame moving with the same velocity as the flame, so that the flame remains at a fixed position in the computational domain. Since the flame velocity is not known a priori, a flame stabilization procedure, which automatically adjusts the speed of the reference frame to be the same as that of the flame, has to be employed.

The progress-variable profile (as well as profiles of density, pressure, etc ...) across the flame verifies the one-dimensional first-order wave equation:

$$\frac{\partial Y}{\partial t} + u_f \frac{\partial Y}{\partial x} = 0 \quad (3.95)$$

where  $u_f$  is the propagation velocity of the flame in the initial reference frame of the simulation. Thus,

$$u_f = - \left(\frac{\partial Y}{\partial t}\right) / \left(\frac{\partial Y}{\partial x}\right). \quad (3.96)$$

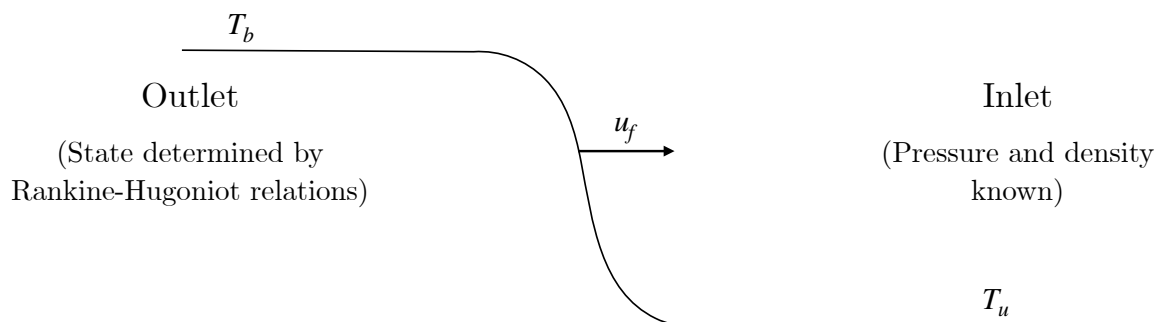


Figure 3.6: Sketch of the temperature profile across a steadily-propagating premixed flame.

The aim of the flame stabilization algorithm is to obtain a stationary flame with  $u_f = 0$ . To that end, we first initialize a flame in a reference frame moving at a low Mach number in the direction of propagation, and we allow the flame to evolve for a few time steps. Then, using equation (3.96),  $u_f$  is calculated at the position of maximum reaction rate, denoted by  $x^*$ . A change of reference frame is then applied by updating the velocity field according to the following relation:

$$u_{new}(x) = u_{old}(x) - \frac{\rho(x^*)}{\rho(x)} u_f(x^*). \quad (3.97)$$

The inlet velocity also updated to match the new flame velocity, and outlet conditions are updated accordingly through the Rankine-Hugoniot relations (2.25-2.27). The process is repeated every few time steps until the flame velocity converges to a fixed value, which usually occurs within a few hundred reaction times. The converged value is known as the one-dimensional laminar flame speed.



## Chapter 4

# One-dimensional dynamics of gaseous detonations

### Sommaire

---

<b>4.1</b>	<b>Introduction</b>	<b>56</b>
<b>4.2</b>	<b>Flow configuration and theoretical formulation</b>	<b>62</b>
4.2.1	Primitive balance equations	62
4.2.2	Characteristic equations in the moving frame	63
<b>4.3</b>	<b>Asymptotic analysis</b>	<b>64</b>
4.3.1	Asymptotic limit and the two-timescale dynamics	65
4.3.2	Unsteady distribution of heat release and scaling law	66
4.3.3	Integral equation	68
4.3.4	Instability threshold for the scaling law	70
<b>4.4</b>	<b>Framework for the parametric analysis</b>	<b>71</b>
4.4.1	Model of reaction rate	71
4.4.2	Parameters formulation	72
<b>4.5</b>	<b>Numerical analysis</b>	<b>73</b>
4.5.1	Problem formulation	73
4.5.2	Numerical implementation	74
4.5.3	Steady CJ detonation	74
<b>4.6</b>	<b>Comparison of theory against simulations</b>	<b>75</b>
<b>4.7</b>	<b>Conclusion</b>	<b>78</b>

---

## 4.1 Introduction

Since the early experimental and numerical works performed by Erpenbeck [18] and Fickett and Wood [19] back in the 1960s, it has been known that the detonation structure is not well described by steady state solution given by the ZND theory. Rather, detonations were found to be largely unsteady and characterized with a complex multi-dimensional structure. The dynamics of these waves has been subject to numerous experimental, theoretical and numerical studies [2, 60–66].

Numerical simulations elucidating the cellular structure of 2D detonations have been performed since the 1970s [67]. Figure 4.1 shows a density color map obtained from a direct numerical simulation (DNS)

of a 2D detonation using the high-order spectral difference method. The color map reveals the complex dynamics of the detonation, whose front is divided into alternating incident waves and Mach stems, with transverse waves propagating from the Mach stems towards incident waves.

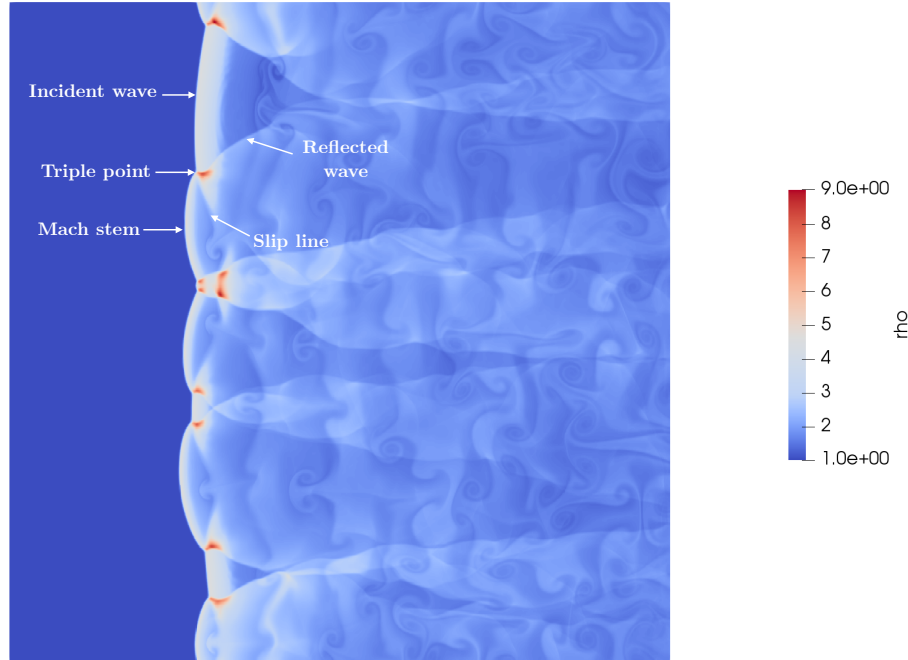


Figure 4.1: Density color map of a two-dimensional detonation, obtained from a 5th-order spectral-difference direct numerical simulation. The flow parameters are  $\gamma = 1.4$ ,  $q_m/c_p T_u = 5$ , and  $E_a/k_B \bar{T}_N = 6$ . The width and height of computational box are in the order of  $10^2$  times the detonation thickness. Density is normalized with respect to its upstream value. The color map reveals the complex dynamics of the flow and the complete cellular structure of the detonation, where the detonation front consists of alternating incident waves and Mach stems, with transverse waves propagating between the two. The triple point at the intersection of three waves is the point with highest temperature and reaction rate in the flow. A slip line trails behind the triple point denoting the boundary between the gases which crossed the Mach stem and those which crossed the reflected wave.

At the intersection of the three waves is the triple point, which is the point with highest temperature and reaction rate on the detonation front. Trailing behind the triple point is the slip line, which denotes the boundary between gases which have crossed Mach stem and those which have crossed the incident then the reflected waves. Gases on both sides of the slip line have an equal pressure, but their densities and temperatures are different. That's why slip lines can be observed in Figure 4.1, but not in the pressure map in Figure 4.2.

Mach stems propagate faster than incident waves, and exhibit a higher reaction rate. Though as triple points traverse the detonation front, they collide and get reflected off of one another, and as they do so, the wave front at each point alternates between being an incident wave and a Mach stem. Trajectories of the triple points are shown in Figure 4.3, which is a time-integrated maximum pressure map for the flow. The map reveals the diamond-shaped cells traced by the triple points of a 2D detonation.

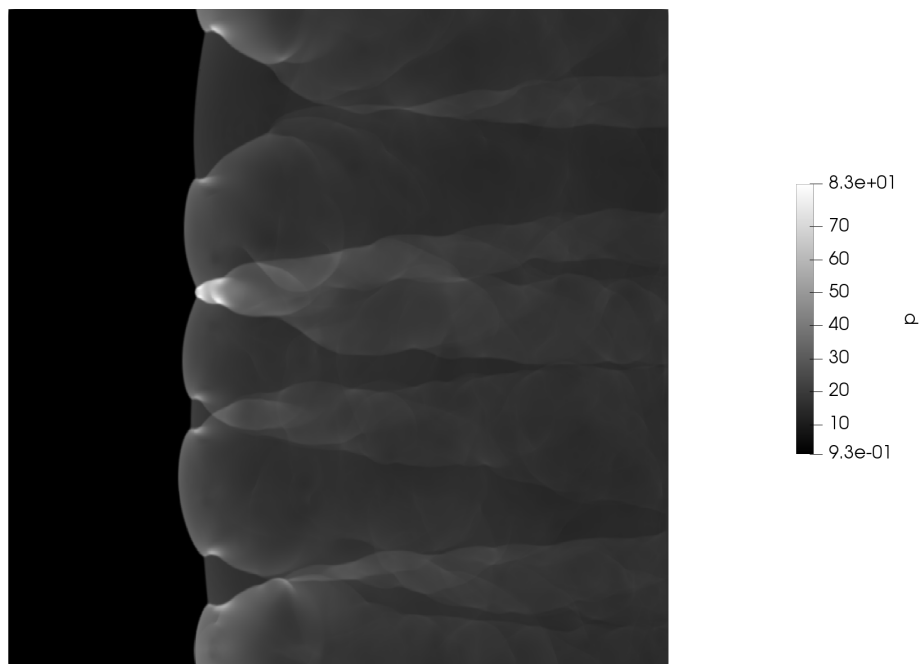


Figure 4.2: Pressure gray-scale map of the same detonation in Figure 4.1. Pressure is normalized with respect to its upstream value. Notice that slip lines are invisible on a pressure map, since pressure is continuous across these lines.

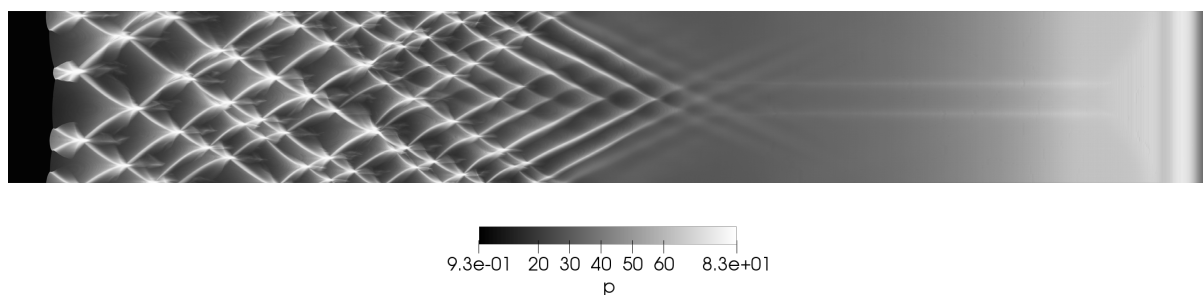


Figure 4.3: Time-integrated gray-scale map of maximum pressure across the detonation. The white lines denote the trajectories of the triple points as they trace the diamond structures characteristic of the cellular detonation. We can observe that soon after the instability sets in, the triple points start merging with one another, and the cell size increases with time.

However, instability is not strictly a multi-dimensional phenomenon, as even one-dimensional detonations exhibit unsteady dynamics characterized by longitudinal pulsations and oscillations in the propagation velocity and the strength of the leading shock wave. In 2005, Ng et al. [68] performed a parametric numerical study to describe the transition of 1D detonations from stable to unstable, and then their transition from periodic oscillations into chaotic oscillations via period-doubling bifurcations. The parameter used to control the dynamics was the Arrhenius activation energy, which describes the thermal sensitivity of the reaction rate.

In the following we present a set of 1D simulations reproducing similar results to those in [68]. A 5th-order spectral difference scheme has been used with  $\gamma = 1.4$  and  $q_m/c_p T_u = 6.69$ . The activation energy  $E_a/k_B \bar{T}_N$  was varied between 5 and 6.  $\bar{T}_N$  denotes the Neumann temperature of the steady state CJ detonation.

Figure 4.4 shows the Neumann pressure plotted a function of time for a detonation with  $E_a/k_B \bar{T}_N = 5$ . At this value of the activation energy, the detonation is still stable. Transition to instability occurs at  $E_a/k_B \bar{T}_N = 5.15$ . Figure 4.5 then shows a plot of Neumann pressure versus time for an activation energy higher than this threshold value, at  $E_a/k_B \bar{T}_N = 5.5$ , and we can observe a period-1 oscillation of the pressure with an oscillation period in the order of  $10\bar{t}_r$ . Increasing the activation energy further to  $E_a/k_B \bar{T}_N = 5.6$ , we can see in Figure 4.6 that a period-doubling bifurcation occurs, and the detonation exhibits a period-2 oscillation. Further period-doubling bifurcations then follow as the activation energy is increased, and at  $E_a/k_B \bar{T}_N = 6$ , we see that the oscillations have become completely chaotic (Figure 4.7).

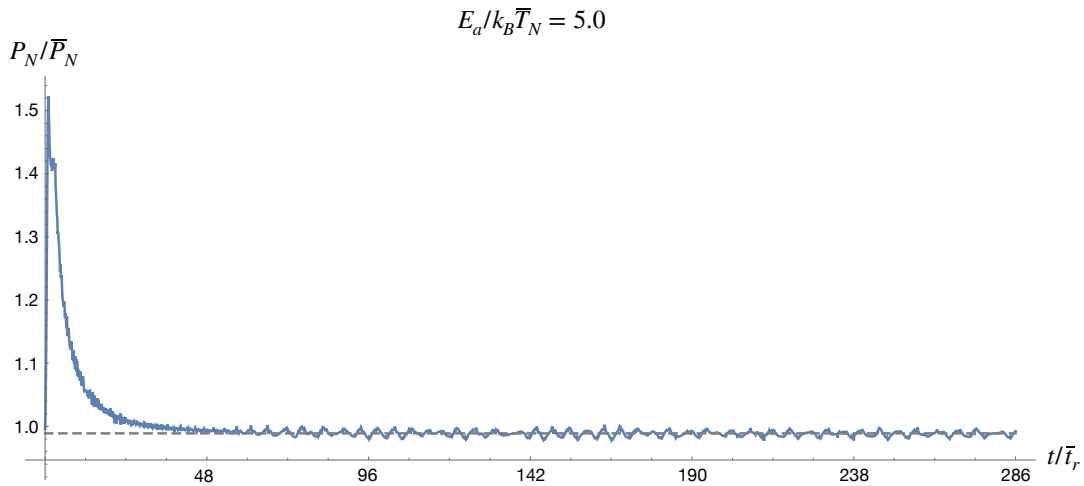


Figure 4.4: The Neumann pressure plotted as function of time for a detonation with  $E_a/k_B \bar{T}_N = 5$ . Pressure is normalized by its steady ZND value, and time is normalized by the steady-state reaction time  $\bar{t}_r$ . The detonation is still stable, and only tiny aberrations of the shock pressure are visible.

In this chapter, our aim is to elucidate the physical mechanisms driving the instability of one-dimensional detonations using asymptotic analysis and high-order numerical simulations. We shall only focus on weakly unstable detonations near the instability threshold.

Since the 1990s, significant advances toward the understanding of the strongly nonlinear dynamics of detonation fronts have been made by theoretical analyses (see [3, 69] and references therein). However, very few asymptotic analyses providing constitutive models describing the behavior of these unsteady supersonic combustion waves have been reported in the literature. Indeed, the unsteady coupling between the shock discontinuity and the combustion chemistry controlling the amount of heat release makes addressing the problem through analytical developments a quite challenging task. The most recent progress in this direction concerns the direct initiation of gaseous detonations for which theoretical analyses have been completed with success [24, 70].

This chapter revisits previous asymptotic developments [23] tackling the linear dynamics of weakly

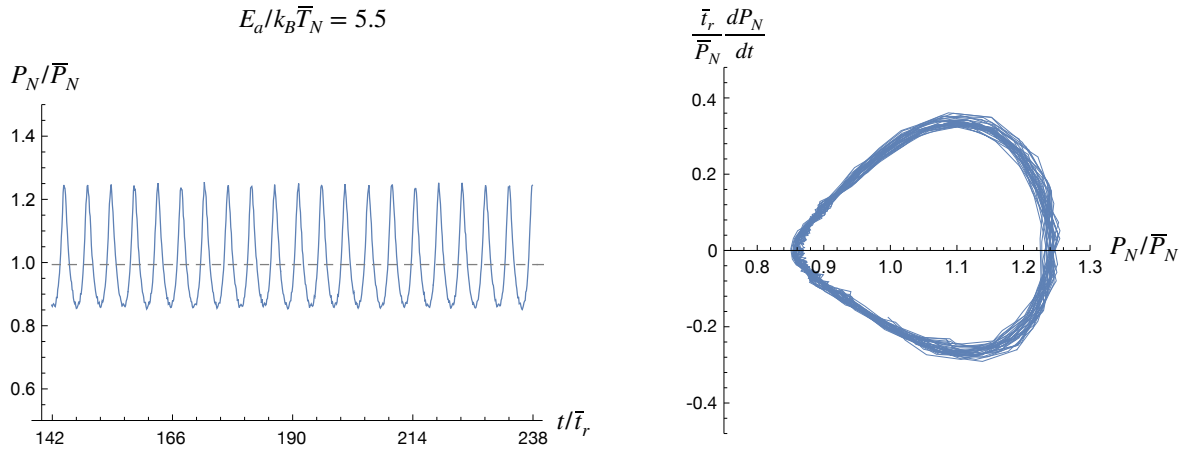


Figure 4.5: The Neumann pressure as function of time for a detonation with  $E_a/k_B\bar{T}_N = 5.5$ . The detonation is unstable, and it exhibits a period-1 oscillation.

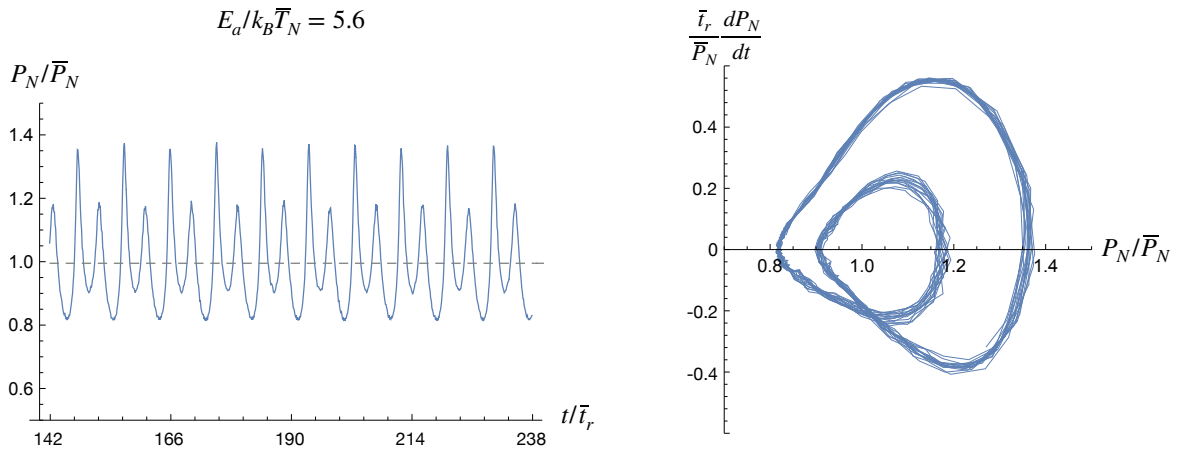


Figure 4.6: The Neumann pressure as function of time for a detonation with  $E_a/k_B\bar{T}_N = 5.6$ . A period doubling bifurcation has occurred and now the detonation exhibits a period-2 oscillation.

overdriven waves in the limit of small heat release and for a ratio of specific heats close to unity. Weakly unstable waves in the Chapman-Jouguet (CJ) regime are considered in the current work (cf. figure 4.8), and three major simplifications are formulated in the asymptotic analysis: firstly, compressional heating within the exothermal reaction zone of the detonation is considered as negligible in comparison to heating by combustion, which is a rather valid approximation for a generic gaseous detonation. Secondly, in association with the limit of small heat release, the variation of the speed of sound with temperature is negligible. Thirdly, a two-timescale dynamics is considered to control the response of heat release in the reaction zone to velocity fluctuations of the leading shock. The two time scales are associated to disturbances developing within the detonation and propagating upstream and downstream respectively,

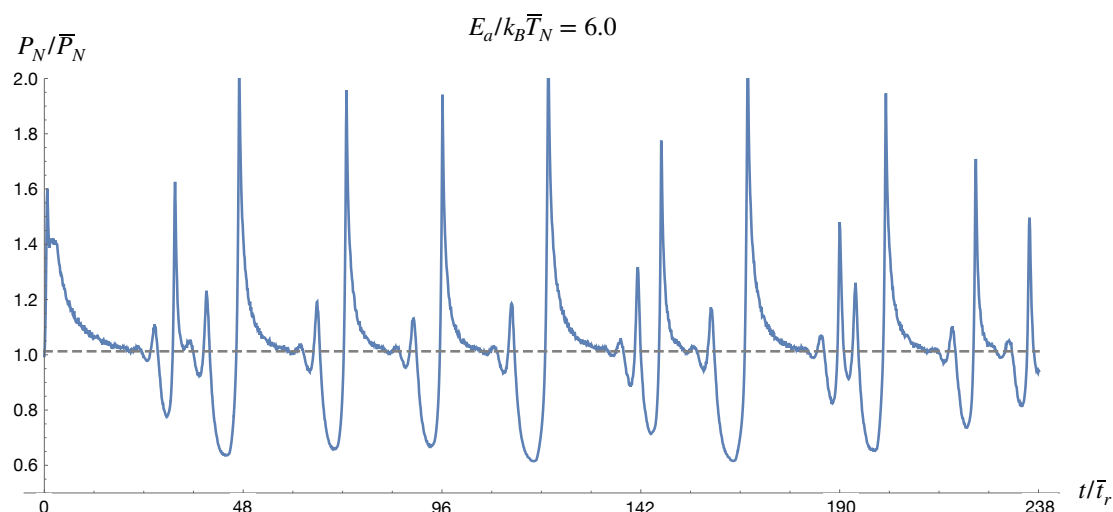


Figure 4.7: Neumann pressure as function of time for a detonation with  $E_a/k_B\bar{T}_N = 6$ . The detonation has now transitioned into the chaotic regime.

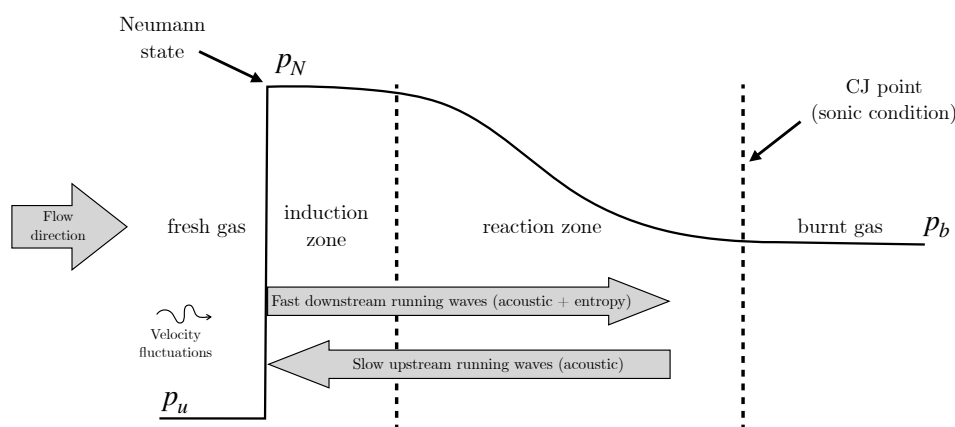


Figure 4.8: Schematic representation of the pressure distribution across a Chapman-Jouguet detonation with characteristics instability modes propagating between the shock and the reaction zone.

as illustrated in figure 4.8. Due to the transonic nature of the flow (Mach number close to unity) in the double limit of small heat release and unity ratio of specific heats, the disturbances propagating via the downstream modes can be considered to be quasi-instantaneous, and the dynamics of the unsteady detonation is only controlled by the upstream-running mode.

In the Chapman-Jouguet regime of real detonations (i.e. outside the asymptotic limits considered for the study), the flow relative to the lead shock is sonic at the end of the reaction zone, but is substantially subsonic at the Neumann state, so that the two-timescale nature of the dynamics is less pronounced. Even though the absolute values of the parameters characterizing the dynamics of these real detonations can be quantitatively different, the general trends reported in this study remain nonetheless qualitatively valid.

In the theoretical part of the current work, the time-dependent velocity of the lead shock is obtained as an eigenfunction of a single hyperbolic equation for the flow velocity with two boundary conditions,

one at the Neumann state using the shock Rankine-Hugoniot conditions, and the other in the burnt gas where a sonic condition is applied for the CJ regime. The flow is fed by an unsteady reaction rate whose time dependence is through the shock velocity only. The solution is then cast in the form of an integral equation for the time-dependent shock velocity of a weakly unstable detonation, just above the instability threshold.

Theoretical results are validated against direct numerical simulations. In the numerical study, the one-dimensional reactive Euler equations are solved using the high-order spectral difference (SD) method [35, 37, 52]. Numerical simulations resolving the oscillations in time are performed in the double limit of low heat release and specific heat ratios close to unity. A modified single-step Arrhenius chemistry whose time dependence follows a scaling law approximating heat-release profiles for real hydrogen-air detonations [22] is used. A recently proposed shock capturing approach for high-order methods based on characteristic waves is applied [57] in order to minimize post-shock numerical aberrations.

The chapter is organized as follows: the flow configuration under study and the theoretical formulation are presented in the subsequent section. Then, the asymptotic analysis leading to an integral equation for the shock velocity of the CJ detonation is presented. The specific framework of the parametric analysis for the comparison of numerical and theoretical results is then discussed. After that, the numerical analysis is presented and results are compared against the theoretical predictions, before concluding.

## 4.2 Flow configuration and theoretical formulation

### 4.2.1 Primitive balance equations

In a planar geometry, Euler's equations of a reactive gas flow take the form

$$\frac{1}{\rho} \left( \frac{\partial}{\partial t} + u \frac{\partial}{\partial x} \right) \rho + \frac{\partial u}{\partial x} = 0, \quad (4.1)$$

$$\rho \left( \frac{\partial}{\partial t} + u \frac{\partial}{\partial x} \right) u = -\frac{\partial p}{\partial x}, \quad (4.2)$$

$$\left( \frac{\partial}{\partial t} + u \frac{\partial}{\partial x} \right) \left[ \ln T - \frac{(\gamma - 1)}{\gamma} \ln p \right] = \frac{q_m}{c_p T} \frac{w(T, Y)}{t_r}, \quad (4.3)$$

$$\left( \frac{\partial}{\partial t} + u \frac{\partial}{\partial x} \right) Y = \frac{w(T, Y)}{t_r}, \quad (4.4)$$

where  $\rho$  is the density,  $p$  is the pressure,  $u$  is the flow velocity in the laboratory frame,  $\gamma = c_p/c_v$  is the constant ratio of specific heat,  $q_m$  denotes the chemical heat release per unit mass of the mixture,  $T$  is the temperature,  $Y$  is the progress variable ( $Y = 0$  in the initial mixture and  $Y = 1$  in the burned gas;  $1 - Y$  is the reduced mass fraction of the limiting component in a one-step reaction),  $t_r$  is the reaction time at the Neumann state of the planar CJ detonation and  $w$  denotes the non-dimensional heat-release rate.

Assuming the ideal gas law, the pressure  $p$  and the sound speed  $a$  may be written as

$$p = \frac{\gamma - 1}{\gamma} c_p \rho T, \quad a = \sqrt{\gamma \frac{p}{\rho}}. \quad (4.5)$$

Attention is focused on an irreversible exothermic reaction, whose rate

$$W(T, Y) = \frac{w(T, Y)}{t_r} \geq 0 \quad (4.6)$$

depends on the temperature  $T$  and the mass fraction of the species  $Y$ , the pressure dependence of the reaction rate being neglected for simplicity in comparison to its thermal sensitivity.

Equations (4.1-4.4) shall be solved in the inner structure of the detonation, with boundary conditions applied just downstream of the lead shock and at the exit of the reaction zone. We consider a propagation from right to left with an orientation of the axis towards the burnt gas, the gas flowing in the negative direction ( $u < 0$ ) in the laboratory frame, as is shown in Figure 4.8.

Denoting the fresh mixture at rest by the subscript  $(\cdot)_u$ , the initial mixture would then be frozen far away from chemical equilibrium at a cold temperature  $T_u$ , with  $Y = Y_u = 0$  and  $w(T_u, Y_u) = 0$ . The lead shock of the detonation is modeled as a discontinuity in the flow of the fresh gases, and denoting the gas in the Neumann state just downstream of the shock by the subscript  $(\cdot)_N$ , the boundary conditions on the shock are then given by the Rankine-Hugoniot jump relations (2.28-2.30), re-expressed here as

$$Y_N = Y_u, \quad (4.7)$$

$$\frac{p_N}{p_u} = 1 + \frac{2\gamma}{\gamma+1}(M^2 - 1), \quad (4.8)$$

$$\frac{\rho_N}{\rho_u} = \frac{1 + (M^2 - 1)}{1 + \frac{\gamma-1}{\gamma+1}(M^2 - 1)}, \quad (4.9)$$

$$\frac{u_N}{a_u} = - \left( 1 - \frac{\rho_u}{\rho_N} \right) M, \quad (4.10)$$

where  $M \equiv \mathcal{D}/a_u > 1$  is the propagation Mach number,  $\mathcal{D}$  being the propagation speed of the lead shock (a positive scalar). For a weak shock  $0 < M - 1 \ll 1$ , the system of equations (4.8-4.10) reads

$$\frac{T_N}{T_u} = 1 + 4 \frac{\gamma-1}{\gamma+1} (M-1) + \mathcal{O}[(M-1)^2], \quad (4.11)$$

$$\frac{p_N}{p_u} = 1 + 4 \frac{\gamma}{\gamma+1} (M-1) + \mathcal{O}[(M-1)^2], \quad (4.12)$$

$$\frac{u_N}{a_u} = - \frac{4}{\gamma+1} (M-1) + \frac{2}{\gamma+1} (M-1)^2 + \mathcal{O}[(M-1)^3], \quad (4.13)$$

$$\frac{U_N}{a_u} \equiv \frac{u_N}{a_u} + M = 1 - \frac{3-\gamma}{\gamma+1} (M-1) + \frac{2}{\gamma+1} (M-1)^2 + \mathcal{O}[(M-1)^3], \quad (4.14)$$

where  $U \equiv u + \mathcal{D}$  is the flow velocity in the shock frame. Considering a CJ detonation propagating in an infinite medium, the boundary condition at the exit of the reaction zone is a sonic condition, meaning that compressible waves in the flow of burnt gas cannot enter the reaction zone (i.e., radiation condition).

## 4.2.2 Characteristic equations in the moving frame

An alternative form of the energy equation (4.3) is expressed in terms of  $p$  and  $u$ , by using the ideal gas law (4.5) when  $\rho$  is eliminated from the mass conservation equation in (4.2),

$$\frac{1}{\gamma p} \left( \frac{\partial}{\partial t} + u \frac{\partial}{\partial x} \right) p + \frac{\partial u}{\partial x} = \frac{q_m}{c_p T} \frac{w(T, Y)}{t_r}. \quad (4.15)$$

The equations for the conservation of mass and momentum (4.1-4.2) can be put in the form of two hyperbolic equations for  $u$  and  $p$  when the equation for conservation of momentum (4.2) is multiplied by  $a/(\gamma p) = 1/(\rho a)$ , then added to and subtracted from (4.15):

$$\frac{1}{\gamma p} \left[ \frac{\partial}{\partial t} + (u \pm a) \frac{\partial}{\partial x} \right] p \pm \frac{1}{a} \left[ \frac{\partial}{\partial t} + (u \pm a) \frac{\partial}{\partial x} \right] u = \frac{q_m}{c_p T} \frac{w(T, Y)}{t_r}. \quad (4.16)$$

These equations, relating the propagation of the disturbances of pressure  $p$  and flow velocity  $u$  to the rate of heat release  $w/t_r$ , are the simple extension of the usual characteristic equations (simple waves) to reacting gases. When (4.5) is used and when the reaction rate  $w(T, Y)/t_r$  is known, the four equations (4.3-4.4) and (4.16) form a closed set of equations for  $p$ ,  $u$ ,  $T$  and  $Y$ .

Considering the intrinsic dynamics of a Chapman-Jouguet wave, the flow in the burnt gas  $u = u_b$ ,  $p = p_b$ ,  $w = 0$ , the sonic condition for the unperturbed wave propagating at the constant CJ velocity  $\bar{D}$  and the radiation condition yield

$$\bar{D} + \bar{u}_b = \bar{a}_b, \quad \delta p_b + \bar{\rho}_b \bar{a}_b \delta u_b = 0, \quad (4.17)$$

where the overline denotes the unperturbed solution, and the decomposition  $z = \bar{z} + \delta z$  has been used.

Let's denote the position of the shock front in the laboratory frame by  $x_f$ , so that

$$x = x_f(t), \quad dx_f/dt = -\mathcal{D}(t) < 0, \quad u < 0. \quad (4.18)$$

Then, it is convenient to express the equations in the reference frame attached to the lead shock:

$$x \equiv x - x_f(t) \quad \Rightarrow \quad \partial/\partial x \rightarrow \partial/\partial x, \quad \partial/\partial t \rightarrow \partial/\partial t + \mathcal{D}(t)\partial/\partial x, \quad (4.19)$$

$\mathcal{D} + u > 0$  being the flow velocity relative to the shock. In this frame, the boundary conditions at the Neumann state take the form

$$x = 0: \quad Y = Y_u, \quad p = p_N(t), \quad T = T_N(t), \quad u = u_N(t) < 0, \quad (4.20)$$

where  $p_N(t)$ ,  $T_N(t)$ , and  $u_N(t)$  are given in terms of the instantaneous propagation velocity  $\mathcal{D}(t) = Ma_u$  by equations (4.8-4.10). Introducing the non-dimensional coordinate  $\xi$  attached to the moving front of the lead shock and reduced by the thickness of the unperturbed CJ detonation,

$$\xi \equiv \frac{x - x_f(t)}{\bar{U}_N t_r}, \quad \text{with} \quad \bar{U}_N \equiv \bar{D} + \bar{u}_N, \quad 0 < \bar{U}_N < \bar{a}_N, \quad (4.21)$$

equations (4.3-4.4) and (4.16) become

$$\begin{aligned} \left[ t_r \frac{\partial}{\partial t} + \frac{(u + \mathcal{D})}{\bar{U}_N} \frac{\partial}{\partial \xi} \right] \left[ \ln T - \frac{(\gamma - 1)}{\gamma} \ln p \right] &= \frac{q_m}{c_p T} w(T, Y), \\ \left[ t_r \frac{\partial}{\partial t} + \frac{(u + \mathcal{D})}{\bar{U}_N} \frac{\partial}{\partial \xi} \right] Y &= -w(T, Y), \end{aligned} \quad (4.22)$$

$$\left[ t_r \frac{\partial}{\partial t} + \frac{(\mathcal{D} + u \pm a)}{\bar{U}_N} \frac{\partial}{\partial \xi} \right] \ln p \pm \gamma \frac{a_u}{a} \left[ t_r \frac{\partial}{\partial t} + \frac{(\mathcal{D} + u \pm a)}{\bar{U}_N} \frac{\partial}{\partial \xi} \right] \frac{u}{a_u} = \gamma \frac{q_m}{c_p T} w(T, Y). \quad (4.23)$$

The boundary conditions (4.17) and (4.20) have to be used at  $\xi \rightarrow \infty$  and  $\xi = 0$ , respectively.

### 4.3 Asymptotic analysis

In this section, we revisit the linear analysis [23] in the limit of small heat release, with a particular attention to the Chapman-Jouguet wave and to the weakly nonlinear solutions just above the instability threshold.

### 4.3.1 Asymptotic limit and the two-timescale dynamics

The analysis is performed in the limit of small heat release  $\mathcal{Q} \equiv [(\gamma + 1)/2]q_m/c_p T_u \ll 1$  by introducing the small parameter  $\epsilon$  and using the following distinguished limit:

$$\epsilon \equiv \sqrt{\mathcal{Q}} \ll 1, \quad (\gamma - 1)/\epsilon \ll 1. \quad (4.24)$$

The propagation Mach number of the planar CJ wave  $\bar{M} = \sqrt{\mathcal{Q}} + \sqrt{\mathcal{Q} + 1}$  differs from unity by a small amount  $\bar{M} - 1 = \epsilon + \mathcal{O}(\epsilon^2)$ . For  $\bar{M} - 1 \ll 1$ , the lead shock is weak. Yet, it can be considered as a discontinuity in a flow governed by the Euler equations if the reaction rate  $1/t_r$  is much smaller than the elastic collision rate  $1/t_{coll}$  and if the detonation thickness  $a_u t_r$  is much larger than the thickness of the lead shock  $a_u t_{coll}/(\bar{M} - 1)$  [3]. This is still the case in the asymptotic limit  $\epsilon \rightarrow 0$ , provided that the following ordering is satisfied:  $t_r/t_{coll} \gg 1/\epsilon$ . Notice, however, that the entropy jump across the lead shock is negligible [3].

In the limit (4.24), the Rankine-Hugoniot conditions (4.10) read,

$$\frac{\bar{p}_N}{p_u} - 1 = 2\epsilon + \mathcal{O}(\epsilon^2), \quad (4.25)$$

$$\frac{\bar{T}_N}{T_u} - 1 = \mathcal{O}[(\gamma - 1)\epsilon], \quad (4.26)$$

$$\frac{a_u}{\bar{U}_N} = 1 + \mathcal{O}(\epsilon), \quad (4.27)$$

$$\frac{\bar{D} - a_u}{a_u} = \epsilon + \mathcal{O}(\epsilon^2), \quad (4.28)$$

$$\frac{\bar{u}_N + \bar{D} - a_u}{\bar{U}_N} = -\epsilon + \mathcal{O}(\epsilon^2), \quad (4.29)$$

$$\frac{\bar{u}_N + \bar{D} + a_u}{\bar{U}_N} = 2 - \epsilon + \mathcal{O}(\epsilon^2). \quad (4.30)$$

The attention is now focused on disturbances that are of the same order of magnitude as

$$\frac{\bar{D} - a_u}{a_u} = \mathcal{O}(\epsilon)$$

but, as we shall see, with a thermal sensitivity of the reaction rate sufficiently large to have variations which are of the order of unity. The non-dimensional flow velocity and the shock velocity, respectively,  $\mu$  and  $\dot{\alpha}_\tau$ , both of them of order unity, are introduced in the limit (4.24) as

$$\frac{\bar{D} + u}{a_u} \equiv 1 - \epsilon\mu, \quad \frac{\mathcal{D} - \bar{D}}{a_u} \equiv \epsilon\dot{\alpha}_\tau \quad (4.31)$$

$$\Rightarrow \frac{\mathcal{D} + u}{a_u} = 1 - \epsilon(\mu - \dot{\alpha}_\tau), \quad M - 1 = \epsilon + \epsilon\dot{\alpha}_\tau + \mathcal{O}(\epsilon^2), \quad (4.32)$$

$$\epsilon \rightarrow 0: \quad \mu = \mathcal{O}(1), \quad \dot{\alpha}_\tau = \mathcal{O}(1), \quad (4.33)$$

$$\frac{a}{a_u} = 1 + \mathcal{O}(\epsilon^2) \Rightarrow \frac{\mathcal{D} + u + a}{a_u} = 2 + \mathcal{O}(\epsilon), \quad \frac{\mathcal{D} + u - a}{a_u} = -\epsilon(\mu - \dot{\alpha}_\tau) + \mathcal{O}(\epsilon^2), \quad (4.34)$$

where the first relation in (4.34) comes from

$$q_m/c_p T_u = \mathcal{O}(\epsilon^2) \Rightarrow (T - T_N)/T_N = \mathcal{O}(\epsilon^2). \quad (4.35)$$

According to equation (4.27), the sound speed  $a_u$  in the denominator of the two last relations in (4.34) can be replaced by  $\bar{U}_N$  without modification of the leading order, showing the quasi-transonic character of the flow velocity  $u + \mathcal{D}$  in the frame attached to the lead shock. Substituting equation (4.32) into Rankine-Hugoniot conditions at the Neumann state (4.11-4.14), one obtains the boundary conditions at the shock as

$$\xi = 0 : \quad p_N/p_u = 1 + 2\epsilon(1 + \dot{\alpha}_\tau) + \mathcal{O}(\epsilon^2), \quad (4.36)$$

$$T_N/T_u = 1 + 2(\gamma - 1)[\epsilon(1 + \dot{\alpha}_\tau) + \mathcal{O}(\epsilon^2)], \quad (4.37)$$

$$\mu_N = 1 + 2\dot{\alpha}_\tau + \mathcal{O}(\epsilon), \quad (4.38)$$

and the boundary condition in the burnt gas (4.17) yields

$$\xi \rightarrow \infty : \quad w = 0, \quad \bar{\mu} = 0 \quad (\text{sonic condition}), \quad (4.39)$$

but no condition on  $\delta\mu$  is prescribed in the burnt gas to leading order in the limit  $\epsilon \rightarrow 0$ , since, according to the definition of  $\mu$  in (4.32),  $\epsilon\delta\mu_b = -\delta u_b/\bar{a}_b$ , which simply implies the order of magnitude of  $\delta u_b$ , namely,  $\delta u_b/\bar{a}_b = \mathcal{O}(\epsilon)$ . In relation with (4.36), it is convenient to introduce the reduced pressure, of order unity in the limit  $\epsilon \rightarrow 0$ ,

$$p/\bar{p}_N - 1 \equiv \epsilon\pi, \quad \pi = \mathcal{O}(1); \quad \xi = 0 : \quad \pi = \pi_N; \quad \pi_N = 2\dot{\alpha}_\tau + \mathcal{O}(\epsilon). \quad (4.40)$$

According to (4.34), equations (4.23) exhibit the two-timescale nature of the compressible waves; the upstream-running wave (propagating toward the lead shock) has a velocity smaller than the velocity of the downstream running one by a factor  $\epsilon$ . Equation (4.22) is the downstream-running entropy wave which is convected by the flow velocity  $u + \mathcal{D}$ . The dynamics is resulting from a continuous set of loops constituted by two downstream-running modes and an upstream-running one. Disturbances are generated at the shock by the fluctuations of the propagation velocity  $\mathcal{D}(t)$ . They are propagated through the detonation thickness by the downstream-running modes, perturbing the distribution of the reaction rate. Disturbances are then sent back to the lead shock by the upstream-running mode, closing the loop.

An instability develops if the retroaction on the shock velocity, delayed by the loops, is in phase with the emission. In the limit  $\epsilon \rightarrow 0$ , the downstream running modes are infinitely faster than the upstream-running one and they produce quasi-instantaneous disturbances. The dynamics of the lead shock is controlled by the upstream-running mode (the slowest in the loop) and, according to equations (4.31) and (4.34), the characteristic time of evolution is longer than the transit time  $t_r$  of a fluid particle across the inner structure of the detonation by a factor of order  $\epsilon$ . It is therefore useful to introduce the time variable of order unity  $\tau = \mathcal{O}(1)$  defined as

$$\tau \equiv \epsilon \frac{t}{t_r} = \mathcal{O}(1), \quad \frac{\partial}{\partial t} = \frac{\epsilon}{t_r} \frac{\partial}{\partial \tau}. \quad (4.41)$$

### 4.3.2 Unsteady distribution of heat release and scaling law

The differential operator on the left-hand side of equations (4.22) takes the form

$$\epsilon \frac{\partial}{\partial \tau} + [1 + \mathcal{O}(\epsilon)] \frac{\partial}{\partial \xi} \approx \frac{\partial}{\partial \xi}$$

so that, to leading order in the limit  $\epsilon \rightarrow 0$ , the equations of species and energy are in steady state.

Neglecting corrections of order smaller than  $\epsilon^2$ , the approximation  $q_m/c_p T_u \approx \epsilon^2$  can be applied to equations (4.22)–(4.23), showing that the relative variation of the energy is of order  $\epsilon^2$ . After dividing by  $\epsilon^2$ , the reduced energy on the left-hand side of the first equation in (4.22),

$$\frac{T - \bar{T}_N}{\epsilon^2 \bar{T}_N} + \left[ \frac{\gamma - 1}{\epsilon \gamma} \right] \pi,$$

varies in the order of unity and, to leading order in the limit (4.24),  $(\gamma - 1)/\epsilon \ll 1$ , compressional heating is negligible.

To leading order, the equations for conservation of species and energy reduce to

$$\frac{1}{\epsilon^2 \bar{T}_N} \frac{\partial T}{\partial \xi} = \frac{\partial Y}{\partial \xi} = w(T, Y), \quad (4.42)$$

with boundary conditions

$$\xi = 0 : T = T_N(\tau), Y = 0, \quad (4.43)$$

$$\xi = \xi_b \rightarrow \infty : Y = 1, w(T, 1) = 0. \quad (4.44)$$

Equation (4.42) allows us to define the reduced temperature of order unity as

$$\theta \equiv \frac{T - \bar{T}_N}{\epsilon^2 \bar{T}_N}.$$

The time dependence of problem (4.42)–(4.44) is through the Neumann temperature  $T_N(\tau)$  only and the instantaneous distribution of the unsteady heat release  $w[\xi, T_N(\tau)]$  is obtained by solving the steady-state problem (4.42)–(4.44) for a given value of  $T_N(\tau)$ , the solution of which is denoted by  $w_o[\xi, T_N(\tau)]$ , with  $\int_0^\infty w_o(\xi, T_N) d\xi = 1$ . According to (4.37), the Neumann temperature varies with the shock velocity as

$$\frac{T_N - \bar{T}_N}{\bar{T}_N} = 2(\gamma - 1)\epsilon \dot{\alpha}_\tau.$$

Thus, the thermal sensitivity of  $w(T, Y)$  should be strong enough to produce a non trivial effect in the limit  $\epsilon \rightarrow 0$ .

For simplicity, we will use a scaling law for the unsteady distribution of reaction rate. The chemical kinetics of ordinary combustible mixtures is constituted by initiation steps, chain-branching steps and recombination reactions. The corresponding spatial distribution of heat release rate in a detonation wave is constituted by an induction zone, followed by a zone of heat release. The thermal sensitivity of the induction length is described by an Arrhenius law,  $l_{ind}(T_N) \propto a_u t_r e^{E/(k_b T_N)}$ , where  $E$  is the activation energy of the chain-branching step [3],

$$l_{ind}(T_N)/l_{ind}(\bar{T}_N) = \exp \left[ \frac{E}{k_B \bar{T}_N} \left( \frac{\bar{T}_N}{T_N} - 1 \right) \right], \quad (4.45)$$

with

$$\bar{T}_N/T_N - 1 = -2(\gamma - 1)[\epsilon \dot{\alpha}_\tau + \mathcal{O}(\epsilon^2)] \quad (4.46)$$

as per (4.37). Introducing the reduced activation energy  $b$  of order unity, the induction length is expressed in terms of the propagation velocity  $\dot{\alpha}_\tau(\tau)$  in the form

$$b \equiv 2(E/k_B \bar{T}_N)(\gamma - 1)\epsilon = \mathcal{O}(1), \quad l_{ind}(T_N)/l_{ind}(\bar{T}_N) = e^{-b \dot{\alpha}_\tau(\tau)}. \quad (4.47)$$

Assuming that the strongest temperature dependence of the reaction rate comes from the induction reactions and neglecting all the other temperature dependence in the limit  $\epsilon \rightarrow 0$ , the unsteady distribution of heat release is approximated by a scaling law,

$$w_o^{(sl)}[\xi, T_N(\tau)] = \frac{l_{ind}(\bar{T}_N)}{l_{ind}(T_N)} \bar{w}_o \left[ \xi \frac{l_{ind}(\bar{T}_N)}{l_{ind}(T_N)} \right] = e^{b\dot{\alpha}_\tau(\tau)} \bar{w}_o \left[ \xi e^{b\dot{\alpha}_\tau(\tau)} \right], \quad (4.48)$$

where  $\bar{w}_o(\xi)$ ,  $\int_0^\infty \bar{w}_o(\xi) d\xi = 1$ , is the normalized distribution of the unperturbed CJ wave, the reference time  $t_r$  used in equation (4.21) being defined as  $\bar{U}_N t_r = l_{ind}(\bar{T}_N)$ . The effect of the scaling law on the reaction rate is illustrated in Figure 4.9. Depending on the sign of the velocity fluctuation  $\dot{\alpha}_\tau$ , the reaction rate will get stretched along the  $y$ -axis and contracted along the  $x$ -axis or vice-versa. In either case, the area under the curve remains constant,  $\int_0^\infty w_o^{(sl)}(\xi) d\xi = 1$ .

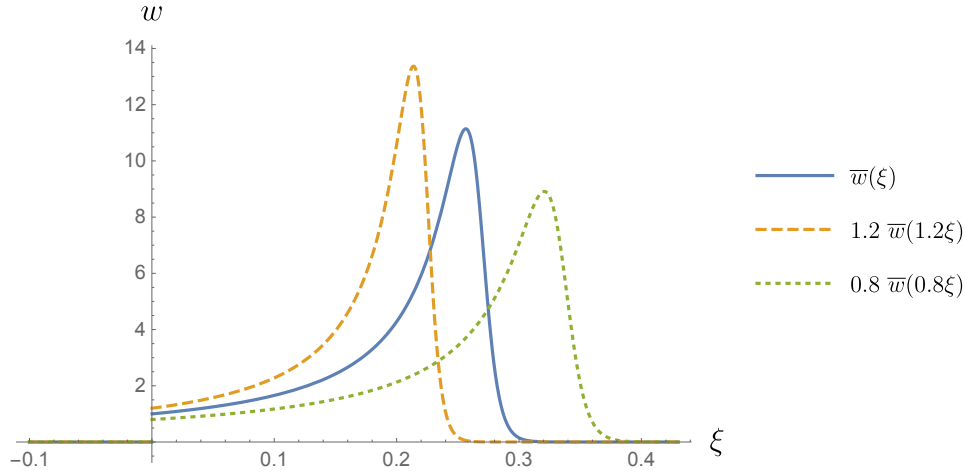


Figure 4.9: Effect of the scaling law on the reaction rate.

It turns out that the approximation (4.48) is satisfactory for hydrogen flames, see figure 2 in [22]. For a better quantitative accuracy, the distribution  $w_o[\xi, T_N(\tau)]$ , solution of the steady equations of energy and species in (4.42)–(4.44), could be used. From now on we will use the notation

$$y(\tau) \equiv b \dot{\alpha}_\tau(\tau) = O(1) \quad (4.49)$$

and write

$$w_o^{(sl)}[\xi, T_N(\tau)] = e^{y(\tau)} \bar{w}_o[\xi e^{y(\tau)}]. \quad (4.50)$$

### 4.3.3 Integral equation

Using (4.32)–(4.34) and (4.40)–(4.41), equations (4.23) divided by  $\epsilon^2$  yield

$$\left\{ \frac{\partial}{\partial \tau} + \left[ \frac{2}{\epsilon} + O(1) \right] \frac{\partial}{\partial \xi} \right\} (\pi - \mu) = w_o[\xi, y(\tau)], \quad (4.51)$$

$$\left\{ \frac{\partial}{\partial \tau} - [(\mu - y/b) + O(\epsilon)] \frac{\partial}{\partial \xi} \right\} (\pi + \mu) = w_o[\xi, y(\tau)], \quad (4.52)$$

where we have used the more transparent notation  $w_o[\xi, y(\tau)]$  in place of  $w_o[\xi, T_N(\tau)]$ . To leading order in the limit  $\epsilon \rightarrow 0$ , equation (4.51) shows that

$$\frac{\partial}{\partial \xi}(\pi - \mu) = 0. \quad (4.53)$$

In addition, from equations (4.38) and (4.40) we get

$$\mu_N = 1 + \pi_N. \quad (4.54)$$

Equations (4.53) and (4.54) then imply that

$$\pi(\xi, \tau) = \mu(\xi, \tau) - 1. \quad (4.55)$$

Substituting the above equation into (4.52), the problem reduces to solving a single hyperbolic equation for the reduced flow velocity  $\mu(\xi, \tau)$ , fed by the heat release  $w_o[\xi, y(\tau)]$ :

$$\frac{\partial \mu}{\partial \tau} - \left[ \mu - \frac{y(\tau)}{b} \right] \frac{\partial \mu}{\partial \xi} = \frac{1}{2} w_o[\xi, y(\tau)], \quad (4.56)$$

which is the simple wave corresponding to the upstream-running mode (propagating in the negative direction, i.e. from the reacting gas to the lead shock). The boundary conditions are (4.17) at infinity and (4.38) at  $\xi = 0$ . The flow of the unperturbed CJ detonation ( $\bar{y} = 0$ ) is  $\bar{\mu}(\xi) \in [0, 1]$ ,

$$\bar{\mu}(\xi) = \sqrt{1 - \int_0^\xi \bar{w}_o(\xi') d\xi'}, \quad \int_0^\infty \bar{w}_o(\xi') d\xi' = 1, \quad \bar{w}_o(\xi) = w_o(\xi, y = 0) > 0. \quad (4.57)$$

The time-dependent propagation velocity  $y(\tau)$  (with  $\bar{y} = 0$ ) is obtained as an eigenfunction of the problem (4.56) with, according to (4.38)–(4.39), the following boundary conditions for the solution  $\mu(\xi, \tau)$ :

$$\xi = 0 : \mu = 1 + 2y(\tau)/b, \quad \xi \rightarrow \infty : \bar{\mu} = 0, \quad \mu = \delta\mu_b \quad (4.58)$$

where  $\delta\mu_b$  is not known, see the text below (4.39). It turns out that the linear solution of (4.56)–(4.58) is obtained without any requirement concerning  $\delta\mu_b$ . Linearization of the flow field  $\mu = \bar{\mu}(\xi) + \delta\mu(\xi, \tau)$  on the left-hand side of (4.56) yields

$$\frac{\partial}{\partial \tau} \delta\mu - \frac{\partial}{\partial \xi} (\bar{\mu} \delta\mu) = \mathcal{G}[\xi, y(\tau)], \quad (4.59)$$

$$\frac{\partial}{\partial \tau} (\bar{\mu} \delta\mu) - \bar{\mu}(\xi) \frac{\partial}{\partial \xi} (\bar{\mu} \delta\mu) = \bar{\mu}(\xi) \mathcal{G}[\xi, y(\tau)], \quad (4.60)$$

where

$$\mathcal{G}[\xi, y(\tau)] \equiv \frac{1}{2} \{ w_o[\xi, y(\tau)] - \bar{w}_o(\xi) \} - \frac{1}{b} \frac{d\bar{\mu}}{d\xi} y. \quad (4.61)$$

It is useful to introduce the change of variable  $\zeta(\xi) \in [0, \infty)$ :

$$\zeta(\xi) = \int_0^\xi \frac{d\xi'}{\bar{\mu}(\xi')}, \quad \bar{\mu}(\xi) \frac{\partial}{\partial \xi} = \frac{\partial}{\partial \zeta}, \quad (4.62)$$

which is a one-to-one correspondence between  $\xi$  and  $\zeta$  inside the inner structure, since the function  $\bar{\mu}(\xi)$  remains positive (it decreases monotonically from 1, at  $\xi = 0$ , to 0 for  $\xi \rightarrow \infty$ ). Introducing the new functions  $F(\zeta, \tau)$  and  $Z(\zeta, \tau)$ ,

$$F(\zeta, \tau) \equiv \bar{\mu}[\xi(\zeta)] \mathcal{G}[\xi(\zeta), y(\tau)], \quad Z(\zeta, \tau) \equiv \bar{\mu}[\xi(\zeta)] \delta\mu[\xi(\zeta), \tau], \quad (4.63)$$

equation (4.60) and the boundary conditions (4.58) become:

$$\frac{\partial Z}{\partial \tau} - \frac{\partial Z}{\partial \zeta} = F(\zeta, \tau), \quad \zeta = 0 : Z = 2y(\tau)/b, \quad \zeta \rightarrow \infty : Z \rightarrow 0, \quad (4.64)$$

where the boundary condition at infinity comes from the limits  $\lim_{\xi \rightarrow \infty} \zeta(\xi) = \infty$  and  $\lim_{\xi \rightarrow \infty} \bar{\mu}(\xi) = 0$ , and one has  $\lim_{\zeta \rightarrow \infty} F(\zeta, \tau) = 0$ .

The general solution of the hyperbolic equation (4.64) is

$$Z(\zeta, \tau) - Z(0, \tau + \zeta) = - \int_0^\zeta F(\zeta', \zeta + \tau - \zeta') d\zeta'. \quad (4.65)$$

Hence, taking the limits  $\zeta \rightarrow \infty$  and  $\tau \rightarrow \infty$ , keeping  $\tau + \zeta$  constant and equal to  $\tau_o$ ,  $\tau + \zeta = \tau_o$ , the boundary condition  $\lim_{\zeta \rightarrow \infty} Z(\zeta, \tau) \rightarrow 0 \quad \forall \tau$  yields

$$Z(0, \tau_o) = \int_0^\infty F(\zeta', \tau_o - \zeta') d\zeta', \quad (4.66)$$

which, when using the boundary condition at the Neumann state in (4.64),  $\zeta = 0 : Z = 2y(\tau)/b$ , becomes an integral equation of the form

$$2y(\tau) = b \int_0^\infty F(\zeta, \tau - \zeta) d\zeta, \quad (4.67)$$

in which the subscript of  $\tau_o$  has been suppressed.

According to (4.59) and (4.63), the time dependence of  $F(\zeta, \tau)$  is through  $y(\tau)$ , so that equation (4.67) is an integral equation for the velocity of the lead shock,  $y(\tau) \equiv b\dot{\alpha}_\tau(\tau)$ , involving an integration on the time delay associated with the transit time of the upstream-propagating mode, from each point inside the inner-detonation-structure to the lead shock (continuous set of loops mentioned at the end of § 4.3.1).

#### 4.3.4 Instability threshold for the scaling law

When considering the stability limit, the function  $F(\zeta, \tau)$  has to be linearized. Using the scaling law (4.48), the linearization yields

$$b\delta F(\zeta, \tau) = g(\zeta)y(\tau), \quad g(\zeta) \equiv \bar{\mu}[\xi(\zeta)]G[\xi(\zeta)], \quad G(\xi) \equiv \frac{d}{d\xi} \left[ \frac{b}{2} \xi \bar{w}_o(\xi) - \bar{\mu}(\xi) \right], \quad (4.68)$$

so that, according to (4.67), the linear integral relation for the propagation velocity takes the form

$$2y(\tau) = \int_0^\infty g(\zeta)y(\tau - \zeta) d\zeta. \quad (4.69)$$

Using a normal mode analysis,  $y(\tau) \propto e^{\sigma\tau}$ , a transcendental equation is obtained for the complex linear growth rate  $\sigma$  in the form of an equation for a Laplace transform

$$2 = \int_0^\infty g(\zeta)e^{-\sigma\zeta} d\zeta, \quad 2 = \int_0^\infty G(\xi)e^{-\sigma \int_0^\xi d\xi'/\bar{\mu}(\xi')} d\xi, \quad (4.70)$$

which is an equation similar to that obtained previously for weakly overdriven detonations [23].

Setting  $\sigma = s + i\omega$ ,  $s = \text{Re}(\sigma)$ ,  $\omega = \text{Im}(\sigma)$ , two equations are obtained for determining the oscillatory frequency and the critical value of  $b$  at the instability threshold ( $s = 0$ :  $b = b^*$ ,  $\omega = \omega^*$ ),

$$2 = \int_0^\infty g(\zeta) \cos(\omega \zeta) d\zeta, \quad 0 = \int_0^\infty g(\zeta) \sin(\omega \zeta) d\zeta. \quad (4.71)$$

The solution is illustrated graphically in Figure 4.10. These relations are valid for any complex set of elementary chemical reactions controlling the combustion kinetics. The only chemical parameter is the distribution  $\bar{w}_o(\xi)$  of heat release in the unperturbed CJ wave. The stiffer the distribution  $\bar{w}_o(\xi)$  is, the more unstable the detonation is; as a result, the value of  $b^*$  gets smaller and the oscillatory frequency  $\omega^*$  gets larger. Therefore, the analysis is limited to chemical kinetics for which the distribution of heat release  $\bar{w}_o(\xi)$  is sufficiently smooth for  $\omega^*$  to be of order unity, such as to satisfy the two-timescale analysis. More precisely, the asymptotic analysis fails as soon as the distribution  $\bar{w}_o(\xi)$  becomes sufficiently stiff to generate a threshold frequency  $\omega^*$  of order  $2\pi/\epsilon$ .

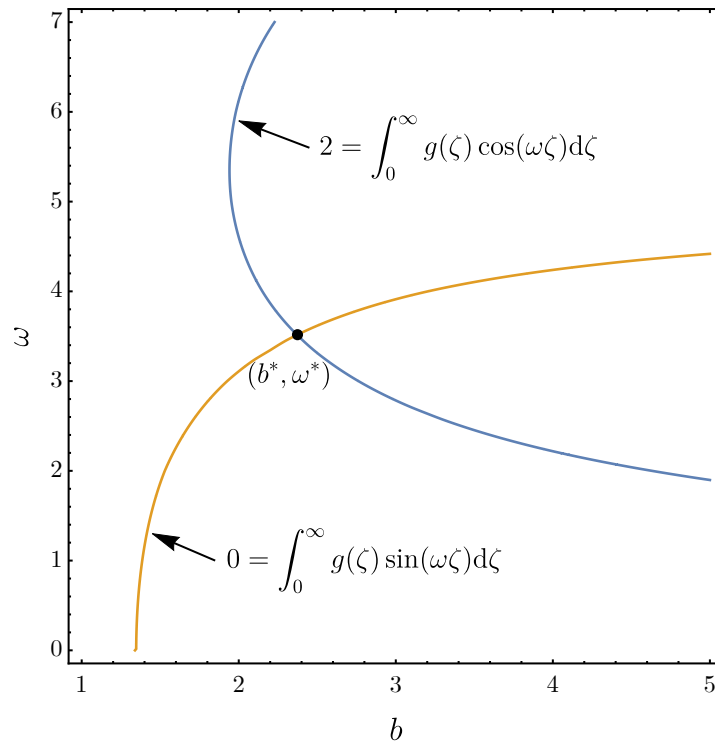


Figure 4.10: Sketch of the solution of the two integral equations for the stability threshold.

## 4.4 Framework for the parametric analysis

### 4.4.1 Model of reaction rate

To ease the parametric study using numerical simulations, we will use the following model of burning rate

$$W(Y, T) = B(1 - Y) \exp\left(-\frac{E}{k_B T_N}\right) \exp\left[\frac{E_T}{k_B T_N} \left(1 - \frac{T_N}{T}\right)\right], \quad (4.72)$$

where  $B$  is the pre-exponential factor with the dimension of an inverse time. The reaction time at the Neumann state  $t_r$  is then given by

$$t_r = t_r(T_N) = \frac{1}{B} \exp\left(\frac{E}{k_B T_N}\right), \quad (4.73)$$

and  $W(Y, T)$  can be rewritten as

$$W(Y, T) = \frac{w(Y, T)}{t_r} = \frac{1}{\bar{t}_r} (1 - Y) \exp\left[\frac{-E}{k_B} \left(\frac{1}{T_N} - \frac{1}{\bar{T}_N}\right)\right] \exp\left[\frac{-E_T}{k_B} \left(\frac{1}{T} - \frac{1}{T_N}\right)\right], \quad (4.74)$$

where  $\bar{t}_r = t_r(\bar{T}_N)$ . This model, first introduced by Clavin & He [22], includes two activation energies:  $E$ , which governs the temperature sensitivity of the induction period, and  $E_T$ , which drives the temperature sensitivity of the rate of heat release. Typically,  $E_T \ll E$  in order to clearly separate the induction zone from the reaction zone. The model aims to give a fair representation of the dynamics of real detonations, where small deviations in the temperature of the shocked gas  $T_N$  from the mean Neumann temperature  $\bar{T}_N$ , induce large variations in the rate of heat release.

However, for the model to be consistent with real detonations, the reaction rate should in addition stay negligible in the fresh gas. For this condition to be verified by equation (4.74) in the limit (4.24), the normalised activation energy  $E_T/(k_B T_N)$  has to be too large, lying outside the range of interest in the current parametric study. Therefore, following the approach of Clavin & Williams [23], a cutoff temperature  $T_c \in [T_u, T_N]$  is introduced so that the reaction rate is zero for temperatures below  $T_c$ , i.e.,

$$W(Y, T) = \begin{cases} 0 & \text{for } T \leq T_c, \\ w(Y, T)/t_r & \text{for } T > T_c, \end{cases} \quad (4.75)$$

where  $w(Y, T)/t_r$  is given by (4.74).

#### 4.4.2 Parameters formulation

First, it is observed that the burning rate in equation (4.74) may be recast in the form

$$W(Y, T) = \frac{w(Y, T)}{t_r} = \frac{1}{\bar{t}_r} (1 - Y) \exp\left[\frac{E - E_T}{k_B \bar{T}_N} \left(1 - \frac{\bar{T}_N}{T_N}\right)\right] \exp\left[\frac{E_T}{k_B \bar{T}_N} \left(1 - \frac{\bar{T}_N}{T}\right)\right]. \quad (4.76)$$

Then, the two reduced activation energies of order unity  $b$  and  $\beta$  are defined as

$$b \equiv 2(\gamma - 1)\epsilon \frac{E - E_T}{k_B \bar{T}_N}, \quad \beta \equiv \epsilon^2 \frac{E_T}{k_B \bar{T}_N}. \quad (4.77)$$

Using the reduced propagation velocity of the lead shock  $\dot{\alpha}_\tau(\tau)$  as given by equation (4.45), one obtains, for the reduced temperature of order unity,

$$\theta = \frac{T - T_N}{\epsilon^2 \bar{T}_N} = \frac{T - \bar{T}_N}{\epsilon^2 \bar{T}_N} - \frac{2(\gamma - 1)\epsilon \dot{\alpha}_\tau(\tau)}{\epsilon^2 \bar{T}_N} \approx \frac{T - \bar{T}_N}{\epsilon^2 \bar{T}_N}. \quad (4.78)$$

Then, using the above expression for  $\theta$ , along with the definitions of  $b$ ,  $\beta$  and  $\dot{\alpha}_\tau$ , the reaction rate takes the form

$$w(Y, T) = e^{b\dot{\alpha}_\tau(\tau)} (1 - Y) e^{\beta\theta}. \quad (4.79)$$

For steady Chapman-Jouguet waves, where, according to (4.32),  $\dot{\alpha}_\tau(\tau) = (\mathcal{D} - \bar{\mathcal{D}})/(a_u \epsilon) = 0$ , the burning rate is given by a set of profiles  $\bar{w}_{o\beta}(\xi)$ , all of them corresponding to the same propagation

velocity  $\bar{D}$ , whose stiffness increases with  $\beta$ . According to (4.42)–(4.44), these profiles are  $\bar{w}_{o\beta}(\xi) = [1 - \bar{Y}_\beta(\xi)]e^{\beta\bar{\theta}_\beta(\xi)}$ , where the functions  $\bar{Y}_\beta(\xi) = \bar{\theta}_\beta(\xi)$  are solutions of

$$\frac{d\bar{Y}_\beta}{d\xi} = (1 - \bar{Y}_\beta)e^{\beta\bar{Y}_\beta}; \quad \xi = 0 : \bar{Y}_\beta = 0, \quad \xi \rightarrow \infty : \bar{Y}_\beta = 1 \quad \text{and} \quad \bar{w}_{o\beta}(\xi) = \frac{d\bar{Y}_\beta(\xi)}{d\xi}. \quad (4.80)$$

Therefore, a parametric analysis of the dynamics is performed using the two scalars  $b$  and  $\beta$ . For every value of  $\beta$  there exists a threshold value  $b^*$  above which the detonation becomes unstable.

The function  $y(\tau) = b\dot{\alpha}_\tau(\tau)$  is obtained from (4.67) using (4.57), (4.59), (4.63) and (4.80) with  $w_o(\xi, y) \rightarrow w_{o\beta}(\xi, y)$  and  $w_{o\beta}[\xi, y(\tau)] \equiv e^{y(\tau)}\bar{w}_{o\beta}[\xi e^{y(\tau)}]$ , since the scaling law (4.48) is automatically satisfied for the reaction rate (4.75)–(4.79). The critical activation energy  $b^*$  and the corresponding oscillation frequency  $\omega^*$  at the instability threshold are obtained from (4.68)–(4.71) for  $\bar{w}_o(\xi) \rightarrow w_{o\beta}(\xi)$ .

## 4.5 Numerical analysis

### 4.5.1 Problem formulation

After using asymptotic developments to anticipate the one-dimensional dynamics of gaseous detonations, the primitive equations are now solved numerically to assess the validity of the theoretical results. For that end, the one-dimensional Euler equations (4.2) and (4.4) used above are cast in their conservative form

$$\frac{\partial \mathbf{U}}{\partial t} + \frac{\partial \mathbf{F}}{\partial x} = \mathbf{S}, \quad (4.81)$$

where the vector of conservative variables  $\mathbf{U}$ , the flux vector  $\mathbf{F}$  and the source vector  $\mathbf{S}$  are given respectively by

$$\mathbf{U} = \begin{pmatrix} \rho \\ \rho u \\ \rho E \\ \rho Y \end{pmatrix}, \quad \mathbf{F} = \begin{pmatrix} \rho u \\ \rho u^2 + p \\ \rho u E + pu \\ \rho u Y \end{pmatrix} \quad \text{and} \quad \mathbf{S} = \begin{pmatrix} 0 \\ 0 \\ \rho q_m W \\ \rho W \end{pmatrix}, \quad (4.82)$$

where  $E$  is the total energy (internal + kinetic) and  $W$  is given by equation (4.75). As previously, the system is closed with the equation of state (4.5).

For the numerical study, direct numerical simulations of one-dimensional CJ detonations are performed in the neighborhood of the double limit of small heat release and  $\gamma$  close to unity, equation (4.24). In practice, the ratio of heat capacities and the normalized heat release per unit mass are set to

$$\gamma = 1.005, \quad Q = \frac{\gamma + 1}{2} \frac{q_m}{c_p T_u} = 0.01 = \epsilon^2.$$

Then, as in the theoretical analysis, the numerical problem is fully characterized by the values of  $\gamma$ ,  $\epsilon$ ,  $b$ ,  $\beta$  and  $\bar{t}_r$ .

The numerical simulations are carried out in the reference frame of the steady CJ detonation, with the inlet flow velocity corresponding to the CJ Mach number given by equation (2.23)

$$\bar{M} = \sqrt{Q} + \sqrt{Q + 1}. \quad (4.83)$$

The outlet boundary condition corresponds to the sonic flow at the CJ state obtained via the Rankine-Hugoniot relations (2.31-2.33):

$$\frac{p_b}{p_u} = \frac{\gamma \overline{M}^2 + 1}{\gamma + 1}, \quad (4.84)$$

$$\frac{\rho_b}{\rho_u} = \frac{(\gamma + 1) \overline{M}^2}{\gamma \overline{M}^2 + 1}, \quad (4.85)$$

$$\frac{u_b}{u_u} = \frac{\rho_u}{\rho_b}. \quad (4.86)$$

## 4.5.2 Numerical implementation

The one-dimensional simulations are carried out using 5th-order SD method, with a mesh consisting of 400 cells. This corresponds to a total number of solution points equal to 2000 in the whole domain. The domain size for each simulation is set so that the detonation thickness is resolved over around 200 solution points. The computational domain extends downstream of the reaction zone for several times the detonation thickness (see Figure 4.11), allowing the sonic condition to be well established at the outlet. This is essential in order to prevent downstream disturbances from getting reflected back, influencing the instability of the detonation [71].

Boundary conditions are enforced weakly using the same approach adopted for the numerical flux at the interior interfaces. For high-order discontinuous finite elements methods, such as the SD used in the present work, this approach is optimal and is often the preferred choice. Furthermore, the use of an approximate Riemann solver for the inviscid fluxes, which is characteristic by construction, guarantees well-posedness. In particular, to compute the numerical flux at the sonic outflow, the pressure, the density and the momentum are extrapolated from the interior of the domain.

### 4.5.2.1 Measurement of $T_N$

The burning rate as defined by equation (4.76) requires precise measurement of the instantaneous value of  $T_N$ , the Neumann temperature.  $T_N$  may be measured making use of the ZND structure of the detonation. Downstream of shock, the ZND profile for temperature is a quasi-linear function of the progress variable in the limit (4.24) and is given in [23] as

$$\frac{T - T_N}{T_u} = \epsilon^2 Y + \mathcal{O}[(\gamma - 1)\epsilon]. \quad (4.87)$$

Therefore,  $T_N$  can be obtained by measuring the value of  $T$  at two different values of  $Y > 0$  downstream of the shock, and then by extrapolating linearly back to  $Y = 0$ . This approach is adopted in the current study with interpolation values for  $Y \sim 10^{-2}$  to  $10^{-1}$  depending on the mesh resolution. The process is repeated at each Runge-Kutta stage, and the method has been found to give sufficiently accurate measurements of  $T_N$  with a relative error in the order of  $10^{-6}$ .

## 4.5.3 Steady CJ detonation

A reference steady CJ detonation is first computed for  $\gamma = 1.005$ ,  $\epsilon = 0.1$ ,  $\beta = 5$ ,  $b = 0.9$  and  $\bar{t}_r = 0.048$ . The length of the computational domain is about  $4\bar{\ell}$ , with the characteristic length  $\bar{\ell} \equiv a_u \bar{t}_r$ . Density and pressure are normalized by their upstream values, and velocity is normalized by  $\sqrt{P_u/\rho_u}$ . The corresponding distributions of these normalized primitive variables versus  $\xi$ , the non-dimensional

coordinate defined by equation (4.21), are shown in figure 4.11a with a zoom within the detonation zone in figure 4.11b. The Neumann-state values of density, pressure and velocity exactly match those obtained from the ZND theory, equation (4.10), which hints to very low numerical dissipation at the shock.

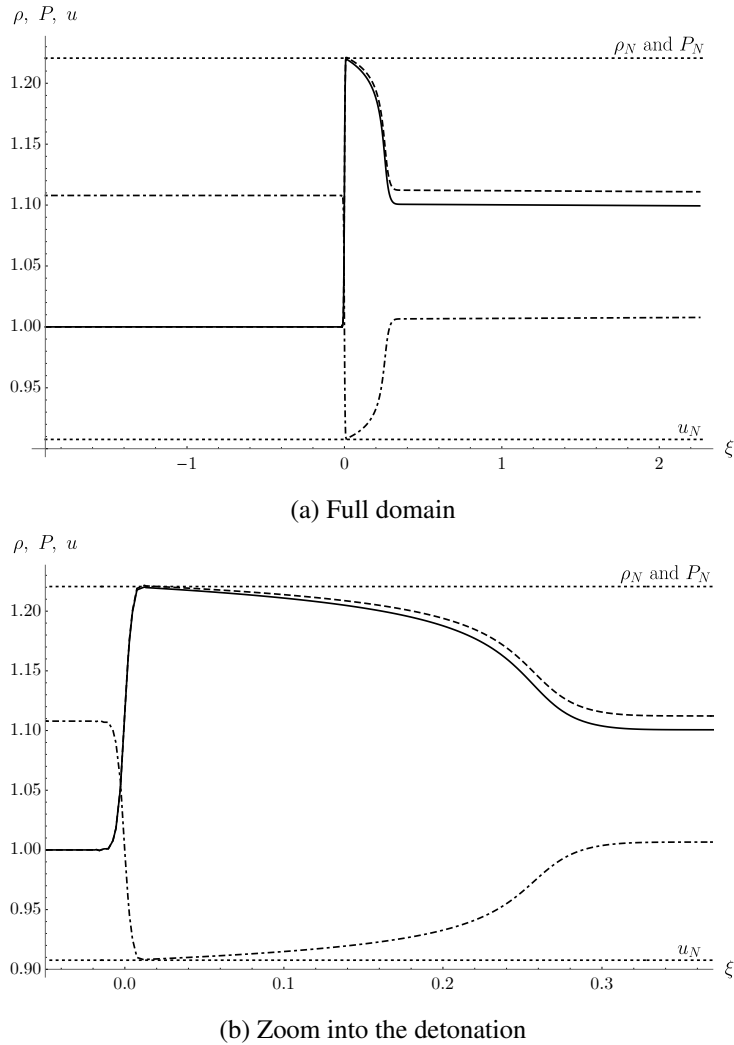


Figure 4.11: Distributions across CJ steady detonation for  $\gamma = 1.005$ ,  $\epsilon = 0.1$ ,  $\beta = 5$ ,  $b = 0.9$ : solid lines, normalized density; dashed lines, normalized pressure; dash-dotted lines, normalized flow velocity; dotted lines; Neumann conditions.

Figure 4.12a shows the progress variable and the heat release rate  $W$  featuring the cut-off towards fresh gases, equation (4.75). Looking at the zooms inside the detonation in figures 4.12b and 4.11b, it is confirmed that the combination of this cut-off temperature in the burning rate with the high-order shock capturing approach minimizes the spurious leaking of mass and heat within the leading shock (i.e., for  $\xi < 0$ ).

## 4.6 Comparison of theory against simulations

In order to compare the theoretical predictions from § 4.3 with the numerical counterparts, the stability of detonations is studied for different values of  $\beta \in [2, 8]$ . In particular, the transition activation

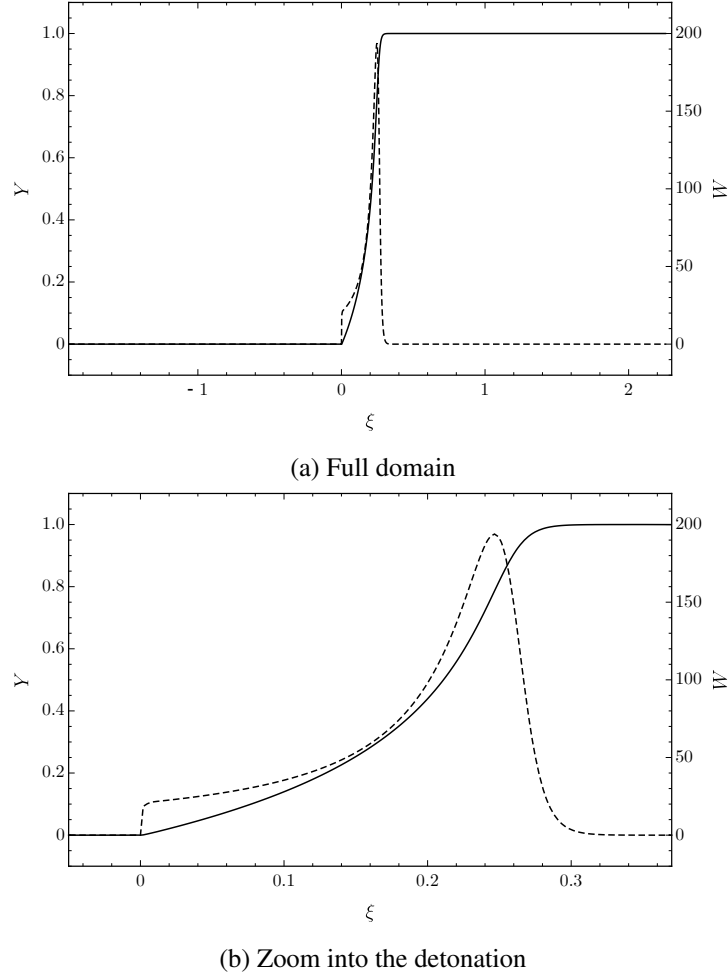


Figure 4.12: Distributions across a representative CJ steady detonation for  $\gamma = 1.005$ ,  $\epsilon = 0.1$ ,  $\beta = 5$ ,  $b = 0.9$ : solid lines, progress variable (left axis); dashed lines, heat release rate  $W$  (right axis).

energy,  $b^*$ , and the corresponding oscillation frequency,  $\omega^*$ , as a function of  $\beta$  are used to verify consistency in the results.

The theoretically expected values of these quantities can be obtained from the asymptotic stability analysis as follows: the evolution equation (4.80) is first integrated to obtain  $\bar{Y}_\beta(\xi)$ , which is used to calculate  $\bar{w}_{o\beta}(\xi) = [1 - \bar{Y}_\beta(\xi)]e^{\beta \bar{Y}_\beta(\xi)}$ . Hence, the reaction rate  $\bar{w}_{o\beta}(\xi)$  is used to calculate  $\bar{\mu}(\xi)$  from equation (4.57), such that  $\bar{w}_{o\beta}$  and  $\bar{\mu}$  can both be used to calculate  $g(\zeta)$  from equations (4.68) and (4.62). Finally,  $g(\zeta)$  is used to obtain the theoretically predicted values of  $b^*$  and  $\omega^*$  from equation (4.71).

To check consistency with numerical results issued from the integration of the Euler equations, two different procedures are adopted:

- Stable CJ detonations are computed numerically for different selected values of  $\beta$  within the range of interest. The reduced heat release rate profiles  $\bar{w}_o(\xi)$  are extracted from the relevant distribution of the progress variable (cf. equation 4.80). Figure 4.13 shows the reduced heat release rate profile  $\bar{w}_o(\xi)$  for stable detonations at various reduced activation energies  $\beta$ , as obtained from numerical simulations. The critical activation energy  $b^*$  and the corresponding oscillation frequency  $\omega^*$  at the instability threshold are then obtained from theory via equations (4.68)–(4.71) in the limit for  $\bar{w}_o(\xi) \rightarrow w_{o\beta}(\xi)$ . The relevant results from this procedure, which makes

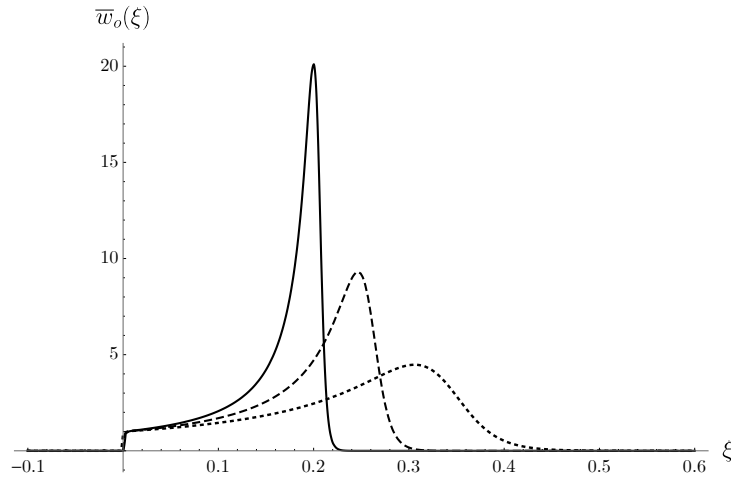


Figure 4.13: Profiles of the reduced heat release rate for stable CJ detonations for  $\beta = 6$  (solid line),  $\beta = 5$  (dashed line),  $\beta = 4$  (dotted line).

use of a blend of theory and numerics, will be hereafter referred to as “Theory, Numerical  $\bar{w}$ ” (TN $\bar{w}$ ).

- The second procedure relies solely on the numerical solution of the Euler equations. In particular, a reference CJ detonation for a given  $b$  is used to initialise subsequent simulations at different values of  $b$  and a fixed value of  $\beta$ . The Neumann temperature is collected versus time, restarting the simulation for  $b < b^*$  the solution evolves towards a steady CJ detonation, for  $b > b^*$  periodic oscillations are observed. As shown, for instance, in figure 4.14, for  $b$  approaching its threshold instability value, the simulation very slowly returns toward a steady CJ case (figure 4.14a), while for  $b$  above its threshold, the temperature oscillation is sustained (figure 4.14b). Accordingly, the values of  $b^*$  and  $\omega^*$  are determined by a trial-and-error procedure checking the onset of the instability on the time evolution of  $T_N$ . Since the oscillation period is expected to be of order of  $t_r/\epsilon$  with  $\epsilon = \sqrt{q_m/c_p T_u} = 0.1$ , the runtime for each of the simulations is set in the order of  $10^3 t_r$  to allow sufficient convergence of the results. This procedure will be referred to as “SIM”.

The transition activation energy  $b^*$  and the corresponding oscillation frequency  $\omega^*$  as obtained from the theory and the two numerical procedures SIM and TN $\bar{w}$  are plotted against the reaction-zone activation energy  $\beta$  in figures 4.15a and 4.15b, respectively. The results show that the transition activation energy  $b^*$  decreases with increasing  $\beta$ , consistent with the observation that the detonation becomes stiffer and thus more unstable with increasing  $\beta$  (cf. figure 4.13). Oscillation frequency on the other hand increases with increasing  $\beta$ .

The breaks in the  $b^*$  curve and the corresponding jumps in the  $\omega^*$  curve are due to the existence of multiple oscillation modes for the detonation. By fixing the value of  $b$  and solving equations (4.70) for the growth rate  $s$  and oscillation frequency  $\omega$ , a frequency spectrum of the detonation oscillations can be obtained. As shown in figure 4.16, different oscillation modes exist for a detonation, and for  $\beta = 5$ , the second mode is the most unstable one, transitioning to instability at some value of  $1.2 < b < 1.4$ . The third mode becomes unstable for some  $b$  slightly less than 2.3, while the first mode is still stable at  $b = 2.3$ . The most unstable mode changes with  $\beta$ , which leads to the jumps in  $\omega^*$  observed in figure 4.15b.

The results show a very good agreement between numerical and theoretical values for both  $b^*$  and  $\omega^*$ .

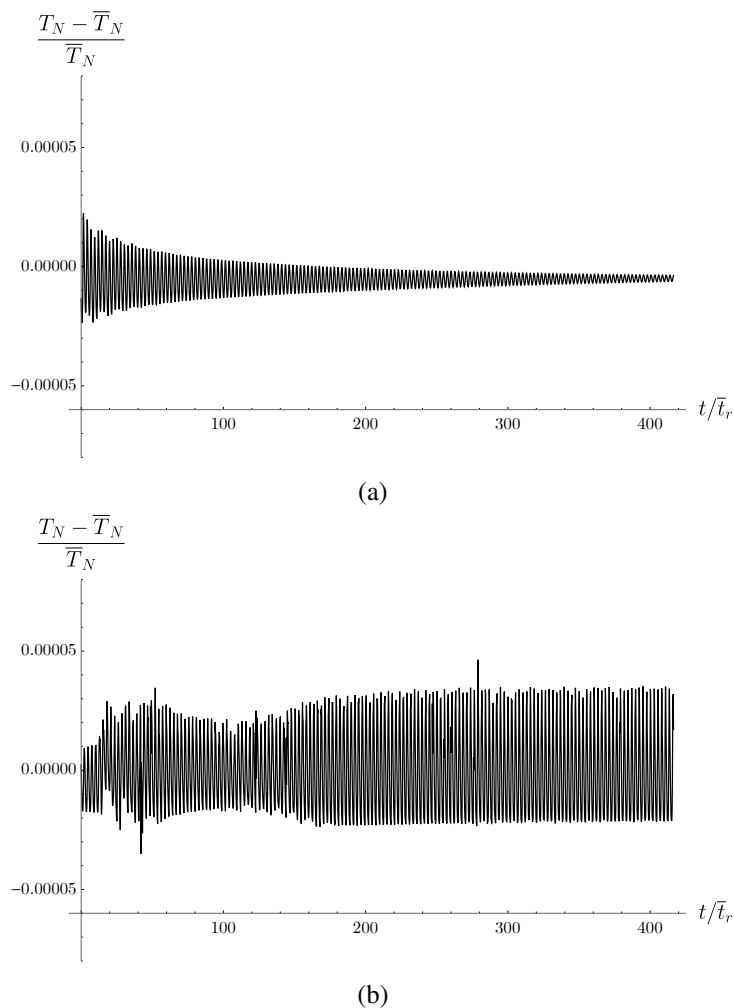


Figure 4.14: Normalized Neumann temperature versus time for detonations at  $\beta = 5$ , with stability threshold  $b^* = 1.21$  (a) return to a steady CJ; (b) unstable detonation.

For large values of  $\beta$ , the solution using the numerical burning rate is in better agreement with the theory than the simulation. Two reasons may be put forward to explain this observation. First, the asymptotic analysis assumes a frequency of order unity, thus the quality of the results may be expected to degrade when the frequency of the oscillation increases. Second, for large values of  $\beta$ , the transition to chaos occurs within a very small interval of the parameter  $b$  which makes the trial-and-error determination of  $b^*$  much less accurate.

## 4.7 Conclusion

High-order numerical simulations and asymptotic developments have been used to tackle the dynamics of one-dimensional gaseous detonations in the quasi Newtonian limit and with low heat release. The focus was on the stability thresholds in terms of activation energy controlling detonations in the Chapman-Jouguet regime. Simulations were performed using a 5th order accurate spectral difference discretization solving the inviscid Euler balance equations, combined with a recently developed high-order shock capturing approach based on characteristic waves sensors. This numerical strategy combined

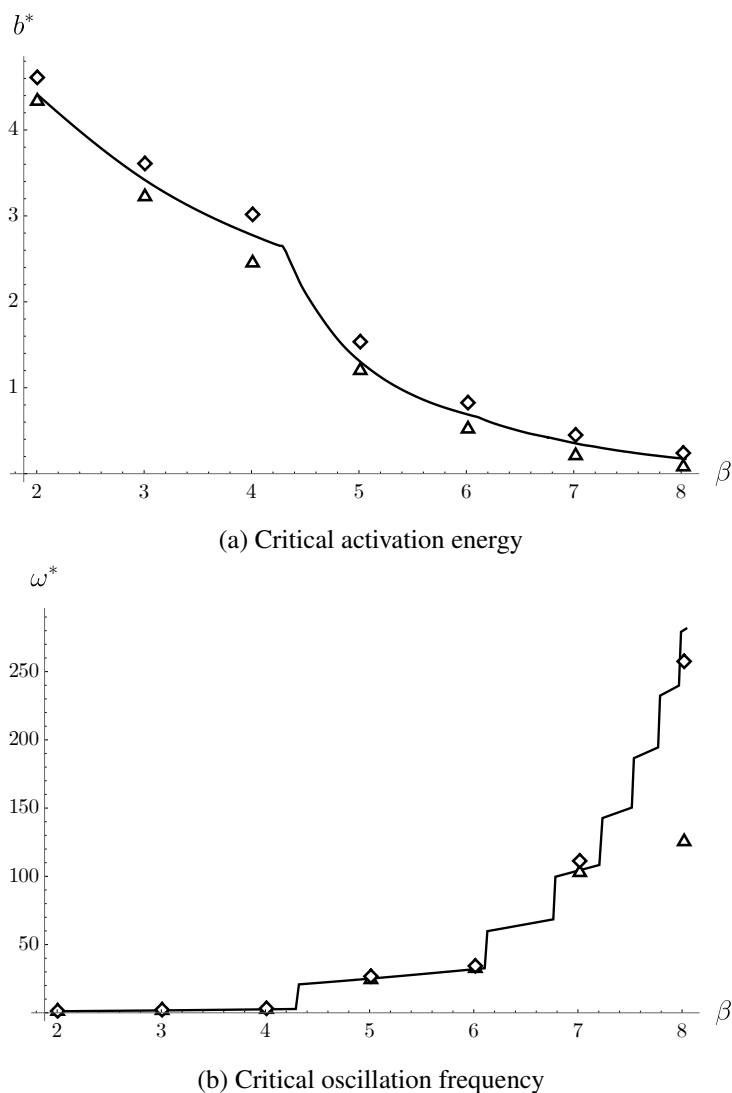


Figure 4.15: Comparison between theory and simulation: solid lines, theory; triangles, SIM; diamonds, TN $\bar{w}$ .

with a specific Arrhenius expression for chemistry allows for the separation of the leading shock from the downstream reaction zone, thus limiting the impact of spurious numerical diffusion of heat and mass ahead of the shock.

In the theoretical part, the time-dependent velocity of the shock appears as the eigenfunction of a single hyperbolic equation for the flow velocity, namely equation (4.56), and the solution is expressed in terms of an integral equation for the shock velocity. The threshold levels of activation energy at which the instability occurs obtained from the theory are in very good agreement with those obtained from numerical simulations.

The theory is grounded on the existence of fast downstream running waves and slow upstream running waves, both traveling between the reaction zone and the shock. The disturbances originating from the downstream running waves are considered to be quasi-instantaneous. An unstable detonation is observed for conditions at which the upstream running wave is in phase with the shock oscillations. The corresponding oscillation frequencies also agree well between theory and numerical predictions.

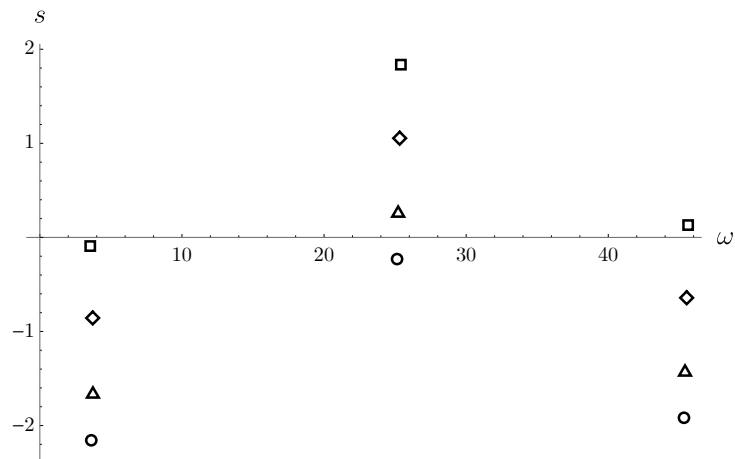


Figure 4.16: Growth rate  $s$  of the first three oscillation modes at different values of activation energy  $b$  for the detonation with  $\beta = 5$ : circles,  $b = 1.2$ ; triangles,  $b = 1.4$ ; diamonds,  $b = 1.8$ ; squares,  $b = 1.2$ . It can be seen that the second mode is the most unstable.

In order to further substantiate the generic character of the results reported in this study, future work shall focus on the validity of such theoretical predictions away from the Newtonian and low heat-release limits.



## Chapter 5

# Deflagration-to-detonation transition at the tip of an elongated flame

### Sommaire

---

<b>5.1</b>	<b>Introduction</b>	<b>82</b>
<b>5.2</b>	<b>Piston model for the back-flow of burned gas</b>	<b>84</b>
5.2.1	Self-accelerating flame	84
5.2.2	Thermal sensitivity of the flame speed in very energetic mixtures	87
<b>5.3</b>	<b>Self-similar solutions</b>	<b>89</b>
5.3.1	Quasi-steady approximation and nonlinear equation	89
5.3.2	Solution of the piston model using the DJ approximation	89
5.3.3	Critical condition for very energetic elongated flames	91
<b>5.4</b>	<b>Comparison with the experimental data</b>	<b>92</b>
<b>5.5</b>	<b>Finite-time singularity</b>	<b>93</b>
<b>5.6</b>	<b>Beyond self-similarity: formation of a shock on the flame front</b>	<b>94</b>
5.6.1	Theoretical analysis	95
5.6.2	Numerical validation	98
<b>5.7</b>	<b>Conclusion</b>	<b>98</b>

---

## 5.1 Introduction

Deflagration-to-detonation transition (DDT) remains a poorly understood problem in combustion. Despite more than a century of research, complete identification of the fundamental mechanisms of DDT, namely the abrupt transition from a reaction-diffusion wave (markedly subsonic and quasi-isobaric) to a supersonic reaction wave (a shock generating an exothermic reaction) has not yet been achieved. Ever since the pioneering experiments of Oppenheim and co-workers [72], DDT has been known to develop in various forms, and there is no mechanism of DDT that is generally agreed upon as being universal. Reviews are presented in relatively recent textbooks [2,3] and the state of knowledge in the mid-twentieth century can be found in a Russian book [73].

In the case of a flame propagating in an unobstructed tube, advanced multi-dimensional numerical simulations have emphasized the role of different mechanisms ranging from the compressible waves in the fresh gases, to the viscous dissipation in the boundary layers for DDT in micro-channels, to the flame

instabilities in macro-channels [74–76]. Recent experiments [30, 77–79] and numerical simulations by Liberman and coworkers [30, 74] shed new light on DDT of self-accelerating laminar flames propagating in tubes filled with very energetic mixtures (stoichiometric mixtures of hydrogen and oxygen or ethylene and oxygen). The flow ahead of the flame is laminar, and the transition to detonation occurs abruptly after an exponential acceleration of the tip (see Figure 5.1). The unsteady compression waves that are generated by the accelerating flame heat the reactive mixture and steepen the shock waves just ahead of the tip of the flame just before a sudden transition to detonation [30, 78]. The Mach numbers of these shocks are between 2 and 3, and the temperature of the compressed mixture does not exceed 850 K.

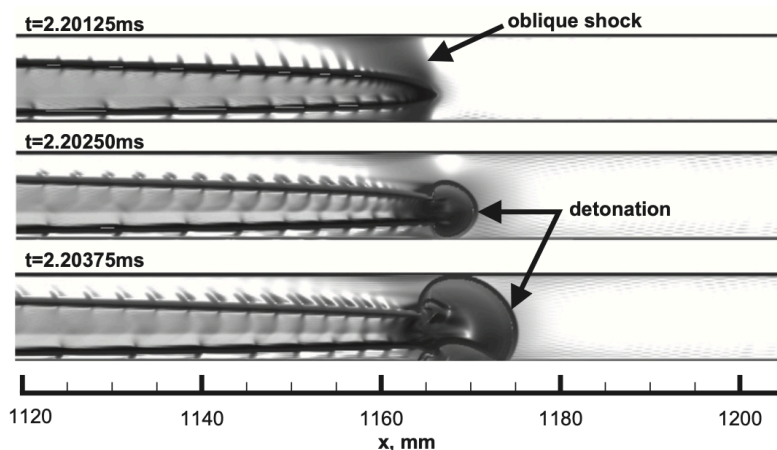


Figure 5.1: Density gradient at consecutive time instances showing the DDT of a hydrogen-air mixture flame in a two-dimensional numerical simulation performed by Liberman et al. [30]. DDT occurs at the flame tip when the equivalent Mach number of the shocks ahead of the flame is between 2 and 3.

Considering the double-discontinuity model of a planar shock wave generated by a turbulent flame, treated as a hydrodynamic discontinuity (self-propagating from the closed end of a tube), Schelkin and Troshin [73] conjectured that DDT is produced when the flame reaches a velocity large enough to generate a strong shock with a short induction time for igniting the compressed gas. This would require the Mach number of the lead shock  $M = \mathcal{D}/a_o$  to be no smaller than  $M \approx 5$ , necessitating a turbulent flame speed much larger than the laminar flame speed by two orders of magnitude for a typical density ratio in flames. Henceforth,  $\mathcal{D}$  denotes the shock velocity and  $a$  denotes the speed of sound, with the subscript  $o$  denoting conditions in the initial quiescent reactant mixture.

Therefore, the aforementioned studies by Liberman et al. rule out both the Shchelkin mechanism [73] and the Zeldovich gradient mechanism [29]. In this chapter, we demonstrate that a simple one-dimensional mechanism, independent of viscous effects, reproduces DDT of elongated flames in tubes for the same condition of temperature and velocity as in the experiments.

More than thirty years ago, Deshaies & Joulin [27] (DJ) published an enlightening theoretical analysis of DDT which was overlooked by the combustion community until 2015-2016, may be due to the fact that the analysis involved a weak lead shock. They derived self-similar solutions of the double-discontinuity model by taking into account the thermal feedback of the lead shock on the flame speed  $U_T$ , which for a turbulent flame in the wrinkled-flame-regime is equal to the laminar flame speed  $U_L$  multiplied by a constant folding parameter  $\sigma > 1$ ,  $U_T = \sigma U_L$ . Using the approximation of a small Mach number of the lead shock ( $M - 1 \ll 1$ ) and the distinguished limit of a high thermal sensitivity  $\beta \gg 1$  of the laminar flame speed  $U_L$ , such that  $\beta U_T/a_o = O(1)$  where  $a_o$  is the sound speed in the initial

mixture, DJ showed that self-similar solutions no longer exist (turning point) when  $\sigma$  is above a critical value, roughly  $\sigma \gtrsim 10$  for a typical density ratio in ordinary flames. If the sudden transition of a quasi-planar flame to a supersonic combustion wave occurs systematically at the loss of self-similarity (turning point), DDT could have been observed with weak shocks ( $M - 1 \ll 1$ ), contrary to experiments. Loss of self-similarity only means that the unsteady compressible effects cannot be neglected and not that DDT occurs systematically at the critical condition, as clearly mentioned by DJ.

In this study, a double-feedback mechanism for DDT of the elongated flame is proposed, in which the new ingredient is the back-flow of burnt-gas towards the flame tip (Figure 5.2). This flow has been observed in experiments [80] and also in numerics by Bychkov and coworkers [81,82] concerning flames in a tube before the formation of the tulip shape. This back-flow acting like a piston at the exit of the reaction zone of the quasi-planar flame at the tip is the key mechanism explaining that the critical condition can be reached with realistic reaction rates and usual laminar flame speeds. This is all the more true for flames in very energetic mixtures since the density ratio is as large as the non-dimensional activation energy (reduced by the enthalpy of the fresh mixture). The objectives of the current study can be listed as the following:

- The first objective is to set up a one-dimensional model for the DDT of the elongated flame, called the piston model. We then show that a self-similar flow described by the piston model exhibits a turning point at which the flame tip acceleration diverges.
- Next it will be shown that the turning point predicted by the piston model for such a flame corresponds accurately to the sudden transition observed in the experiments [30, 78].
- Finally, it will be shown that the divergence of the acceleration of the tip of a self-accelerating flame at the critical condition leads to the formation of a shock on the flame front, whatever is the growth rate of the elongated front. Depending on its intensity, such a shock could quasi-instantaneously blow up the inner structure of the laminar flame, even if the Mach number is not strong enough to produce self-ignition in the fresh mixture ahead of the flame. However, DDT is not expected to be produced if the shock is too weak.

## 5.2 Piston model for the back-flow of burned gas

Consider a flame which is ignited punctually at the center of the closed end of a tube. In connection with their revealing experimental investigation of the mechanism by which tulip flames are formed, Clanet and Searby [83] (CS) present a model for the acceleration of the tip of an elongated flame. The flow of burned gas inside the volume delimited by the elongated flame front is fed by the combustion of the lateral wing of the flame skirt, producing a back-flow of burned gas towards the flame tip which is the basic ingredient of the piston model, see Figure 5.3. As the length of the flame skirt increases, the back flow would cause further acceleration of the flame tip.

### 5.2.1 Self-accelerating flame

In a rough approximation, following CS, the flow of burned gas on the axis of the cylindrical tube is modeled by the solution of the one-dimensional equation for the conservation of mass with a source term describing the effect of the combustion of the lateral wings. Neglecting the curvature effect, the tip of the flame front is considered as a planar wave perpendicular to the axis. The flow  $u_b(x, t)$  of burned gas is delimited by the wall at  $x = 0$  ( $u_b = 0$ ) and the flame at the tip  $x = L$  ( $u_b = u_{bf}$ ). Denoting  $U_L$  and  $U_b$  the laminar flame speeds relative to the fresh mixture and the burned gas respectively,  $\rho_u U_L = \rho_b U_b$ ,

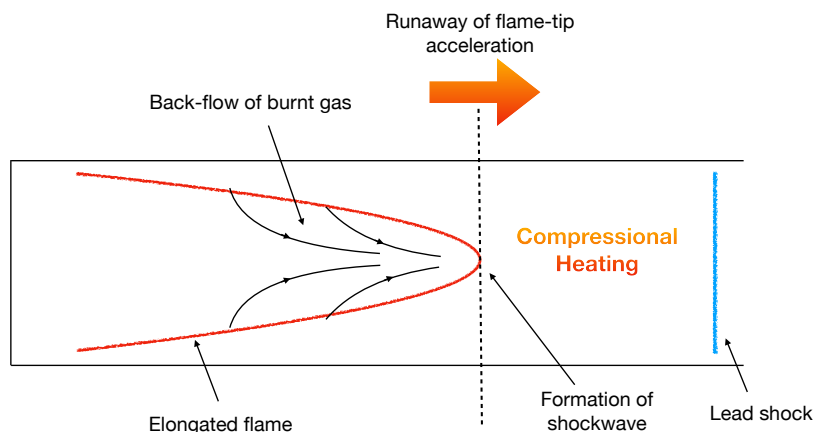


Figure 5.2: A sketch illustrating the double-feedback mechanism proposed in this study to be responsible for DDT. The flame is accelerated by the increase of the fresh gas temperature due to compression waves traveling ahead of the flame, and also by the back flow of burnt gas propagating from the lateral wings of the elongated flame towards the flame tip. We show that this mechanism leads to a blow-up of the flame tip acceleration and a formation of a shock wave on the flame tip for a Mach number of the leading shock consistent with the conditions for DDT observed in experiments [30, 77–79].

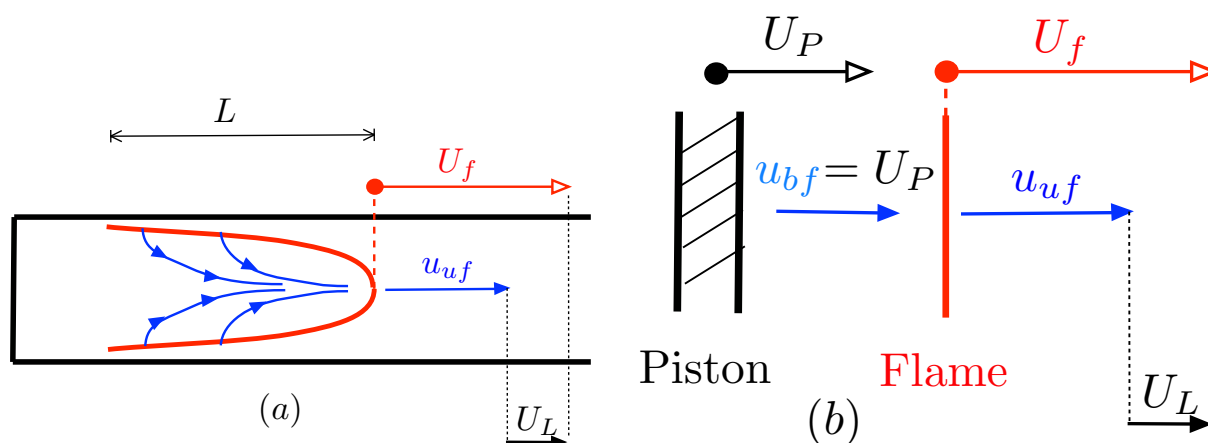


Figure 5.3: (a): Sketch of the self-accelerating elongated flame propagating in the laminar regime. The streamlines of the burnt-gas flow issuing from the lateral wings of the flame front and oriented towards the flame tip are shown in blue. This back-flow of burnt-gas towards the tip is essential to the occurrence of DDT of elongated flames. (b): One-dimensional piston model. The velocity of the piston  $U_p(t)$  increases with the extension of the flame front  $L(t)$  and also with the temperature of the burnt gas (through the laminar burning velocity measured in the burnt gas), see (5.1). This model defines the simplest configuration of the double-feedback mechanism upon the tip of an elongated flame leading to DDT: firstly the compressional heating by the upstream-running simple waves generated in the unburnt-gas flow by the flame acceleration,  $dU_f/dt > 0$ , and secondly the convective motion of the flame (at the tip) caused by the back-flow of burnt-gas,  $u_{bf} \gg U_L$  for very energetic mixtures  $\rho_u \gg \rho_b$ ,  $U_b \gg U_L$ .

$\rho_u$  and  $\rho_b$  being the corresponding densities, the rate of mass production per unit volume by the lateral wings of the elongated front is  $2\rho_b U_b/R$  where  $R$  is the tube radius.

If the rate of increase of the length of the elongated flame  $L(t)$  is slow at the scale of the transit time of a fluid particle across the flame, the inner flame structure is quasi-steady. If, in addition,  $dL/dt \ll a_b$ ,  $L/(dL/dt) \gg L/a_b$ , where  $a_b$  is the speed of sound in the burned gas, the unsteady compressible effects are negligible in the burned gas, such that the temperature and pressure of the fresh mixture on the lateral wings are the same as at the tip of the elongated flame, and the thermodynamic properties of the burnt gas are quasi-uniform and quasi-steady. The variation of density being negligible, the velocity of burned gas  $\bar{u}_b(x, t)$  in the laboratory frame increases linearly with the distance from the closed end of the tube ( $x = 0$ ) [83],

$$dL/dt \ll a_b \quad \Rightarrow \quad \frac{\partial \bar{u}_b}{\partial x} = 2 \frac{\bar{\rho}_{uf}}{\bar{\rho}_{bf}} \frac{U_L}{R} = 2 \frac{U_b}{R}, \quad \bar{u}_{bf} = 2U_b \frac{L}{R}. \quad (5.1)$$

Henceforth, the over-bar denotes the self-similar solutions, neglecting the unsteadiness of the compressible waves in the external gas flows (burnt and unburnt), and the subscript  $f$  refers to the tip of the elongated flame. The inner flame structure being in a quasi-steady state, the flow velocities of burned and unburned gas  $\bar{u}_{bf}$  and  $\bar{u}_{uf}$  respectively (just behind and ahead the tip of the flame) are related to the velocity of the tip of the flame in the laboratory frame  $U_f(t) = dL/dt$  by the isobaric conservation of mass  $\partial(\rho[\bar{u} - U_f])/\partial x = 0$ ,  $\bar{\rho}_{uf}(U_f - \bar{u}_{uf}) = \bar{\rho}_{bf}(U_f - \bar{u}_{bf})$

$$\frac{L}{dL/dt} \gg \tau_L \quad \Rightarrow \quad \bar{u}_{uf} = \frac{\bar{\rho}_{bf}}{\bar{\rho}_{uf}} \bar{u}_{bf} + \left(1 - \frac{\bar{\rho}_{bf}}{\bar{\rho}_{uf}}\right) U_f = 2U_L \frac{L}{R} + \left(1 - \frac{\bar{\rho}_{bf}}{\bar{\rho}_{uf}}\right) U_f. \quad (5.2)$$

Introducing the laminar flame speed  $U_L$  for a fresh gas at temperature  $\bar{T}_{uf}$

$$U_f = \bar{u}_{uf} + U_L \quad (5.3)$$

into (5.2) yields the expressions of  $\bar{u}_{uf}$  and  $U_f$  in terms of the laminar flame speed  $U_L$ , the density ratio  $\bar{\rho}_{uf}/\bar{\rho}_{bf} = \bar{T}_b/\bar{T}_u > 1$  and the length  $L$  of the elongated flame front:

$$\bar{u}_{uf} = U_L \frac{\bar{\rho}_{uf}}{\bar{\rho}_{bf}} \sigma - U_L, \quad \frac{U_f}{U_L} = \frac{\bar{\rho}_{uf}}{\bar{\rho}_{bf}} \sigma, \quad \frac{U_f}{U_b} = \sigma, \quad \text{where} \quad \sigma \equiv \left[2 \frac{L}{R} + 1\right]. \quad (5.4)$$

$\sigma$  characterizes the elongation of the flame (ratio of the flame surface area to the cross-section area of the tube). The classical expression of the flow velocity generated ahead of a planar flame when the burned gas is at rest  $u_u = (\rho_u/\rho_b - 1)U_L$ ,  $U_f = (\rho_u/\rho_b)U_L$  is recovered from the first equation in (5.4) for  $2L/R = 0$ . Equations (5.2) and (5.4) are relevant locally at the tip of the elongated flame. The overall conservation of mass between the closed end of the tube and a cross-section sufficiently ahead of the tip leads to the same flow velocity as in DJ [27]  $[(\bar{\rho}_{uf}/\bar{\rho}_{bf}) - 1]\sigma U_L$  where  $\sigma$  denoted the degree of folding of the turbulent wrinkled flame of DJ. Here, the local flow velocity  $\bar{u}_{uf}$  is much larger, as discussed now.

Equations (5.2-5.4) correspond to a one-dimensional piston model of a planar flame pushed by a moving piston whose velocity  $U_P$  is equal to  $\bar{u}_{bf} = (2L/R)(\bar{\rho}_{uf}/\bar{\rho}_{bf})U_L$ ,

$$U_P = (\sigma - 1)(\bar{\rho}_{uf}/\bar{\rho}_{bf})U_L = (\sigma - 1)U_b, \quad (5.5)$$

see Figure 5.3-b. The burnt-gas velocity  $\bar{u}_{bf}$  generated just behind the flame tip by the lateral wing of the elongated flame front (Figure 5.3-a) is the essential difference from the DJ model of wrinkled flame [27]. Because of the large density ratio  $\bar{\rho}_{uf}/\bar{\rho}_{bf} \approx 10$ ,  $U_b/U_L \approx 10$ , this velocity is large in very energetic mixtures, even when the flame length  $L$  is not much larger than the tube diameter. According to (5.1),  $\bar{u}_{bf}$  depends on the flame speed  $U_L$ . Therefore, the change in  $U_L$  due to the increase of fresh gas temperature

by the leading shock results in a double feedback mechanism acting on the flame tip, whose velocity is being affected by the both flame elongation and the upstream gas temperature.

After ignition and before the time at which the skirt of the elongated front leaves the closed end of the tube (namely the time  $R/U_b$  for the lateral wing of the flame to reach the lateral wall of the tube), the geometrical relation  $U_f(t) = dL/dt$ , combined with (5.4), leads to the CS exponential growth of the length of the elongated front [83]

$$\frac{d(L/R)}{dt} \equiv \frac{U_f}{R} = \frac{\bar{\rho}_{uf}}{\bar{\rho}_{bf}} \frac{U_L}{R} \left( 2 \frac{L}{R} + 1 \right) = \frac{U_b}{R} \left( 2 \frac{L}{R} + 1 \right) \quad (5.6)$$

involving the characteristic time scale

$$\tau_{ev} = R/2U_b = (U_{bo}/U_b)\tau_{evo} \quad \text{where} \quad \tau_{evo} = R/2U_{bo} \quad \text{with} \quad U_{bo} = (T_{bo}/T_o)U_{Lo}. \quad (5.7)$$

According to (5.6), the conditions for a quasi-steady approximation in the burned gas ( $dL/dt \ll a_b$ ) and inside the flame structure ( $d_L/U_b \ll \tau_{ev}$ , where  $d_L$  is the laminar flame thickness) read

$$2L/R \ll a_b/U_b = \sqrt{T_u/T_b} a_u/U_L \quad \text{and} \quad d_L/R \ll 1 \quad \text{respectively.} \quad (5.8)$$

However, the acceleration of the tip stops suddenly after a lapse of time of order  $R/U_L$  leading to the formation of a tulip flame (associated with the strong deceleration [3, 83]). This phenomenon usually occurs before DDT and is followed by a second stage of weaker acceleration in the DDT experiments [30, 78]. Taking into account the viscous effect, the two-dimensional numerical simulations of flames in a tube with no-slip condition at the wall, carried out by Bychkov and coworkers [81, 82], have shown that a curved flame accelerates during a longer period of time with a growth rate smaller than (5.7) by a factor depending on the Reynolds number. The streamlines of the back-flow of burned gas towards the flame tip, sketched in Figure 5.3-(a), are clearly exhibited in these numerical simulations and in experiments [80] as well. In the following, the expression (5.7) of the characteristic time for the growth rate of the flame length  $L$  has to be understood as a dimensional equation,  $\tau_{evo} \propto R/2U_{bo}$ . The forthcoming results are valid regardless of the numerical coefficient, see the end of § 5.5. The essential point is that the burnt-gas velocity  $\bar{u}_{bf}$  in (5.1) is much larger than the laminar flame speed  $U_L$  and is proportional to the value of  $U_L$  corresponding to the gas temperature just ahead of the flame, which drives the double feedback mechanism.

### 5.2.2 Thermal sensitivity of the flame speed in very energetic mixtures

Because of a large density ratio close to 10, the thermal sensitivity of the laminar flame-speed of very energetic mixtures is weaker than that for ordinary mixtures. This can be checked on the burning-velocity derived by Zeldovich and Frank-Kamenetskii [50] for a one-step kinetics scheme governed by an Arrhenius law in the limit of large Zeldovich number  $\beta_b \equiv [E_a/(k_B T_b)][q_m/(c_p T_b)] \gg 1$ , which we re-derived in §2.3.4 (equation (2.105)):

$$U_L = \frac{\rho_b}{\rho_u} \sqrt{2\nu! \text{Le}^\nu \frac{1}{\beta_b^{\nu+1}} \frac{D_{Tb}}{\tau_{rb}}}. \quad (5.9)$$

Using the expression of the reaction rate given by equation (2.55) as

$$\frac{1}{\tau_{rb}} = \left( \frac{\rho_b}{\rho_u} \right)^{\nu-1} b \frac{e^{-E_a/k_B T_b}}{(\tau_{coll})_b}, \quad (5.10)$$

equation (5.9) can be rewritten as

$$U_L = a_b \left( \frac{\rho_b}{\rho_u} \right)^{\frac{\nu+1}{2}} T_b^{\nu+1} K e^{-E_a/2k_B T_b} = a_b (T_b T_u)^{\frac{\nu+1}{2}} K e^{-E_a/2k_B T_b}, \quad (5.11)$$

where

$$K \equiv \sqrt{2b\nu! \text{Le}^\nu \left( \frac{k_B c_p}{E_a q_m} \right)^{\nu+1}}. \quad (5.12)$$

In the above equations,  $1/\tau_{coll}$  represents the elastic collision frequency, and the relation  $D_T/\tau_{coll} = a^2$  has been used in (5.11). In the one-step approximation, the reaction order determines the pressure dependence of the reaction rate. Flames, in general, have contributions from unimolecular, bimolecular, and three-body elementary steps affecting their effective one-step reaction order, but (largely computational) considerations of laminar burning velocities suggest that the bimolecular steps are dominant for highly energetic mixtures, leading to the effective reaction order being close to 2 and thus to a weak pressure dependence of the constant dimensional factor  $K$  (dimension  $1/\text{Kelvin}^{(\nu+1)/2}$ ) which is neglected in the following.

According to the kinetic theory of gas, the factor  $b$  in (5.10) is of order unity and cannot be large,  $b \approx 1$ . Therefore, the ratio

$$U_L/a_b \approx (\rho_b/\rho_u)^{\frac{\nu+1}{2}} e^{-E_a/2k_B T_b} / \beta_b^{\frac{\nu+1}{2}}$$

is a small number not larger than  $2 \times 10^{-2}$  in very energetic mixtures ( $\rho_b/\rho_u \ll 1$ ) and much smaller, typically  $1.5 \times 10^{-3}$ , in other mixtures ( $E_a/k_B T_b \gg 1$ ), so that the isobaric approximation  $\rho_b T_b = \rho_u T_u$  used in (5.11) is verified for flames in any premixed gas. Considering the reference state just ahead of the lead shock, denoted by the subscript  $o$ , and using the relations  $a_b/a_{bo} = \sqrt{T_b/T_{bo}}$ ,  $\rho_b T_b = \rho_u T_u$  and  $\rho_{bo} T_{bo} = \rho_{uo} T_{uo}$ , equation (5.11) yields

$$\frac{U_L}{U_{Lo}} = \left( \frac{T_b}{T_{bo}} \right)^{1+\nu/2} \left( \frac{T_u}{T_{uo}} \right)^{(\nu+1)/2} \exp \left[ -\frac{E_a}{2k_B} \left( \frac{1}{T_b} - \frac{1}{T_{bo}} \right) \right], \quad (5.13)$$

where  $T_b = T_u + q_m/c_p$  and  $U_{Lo}$  is the laminar flame speed in a fresh mixture at temperature  $T_{uo}$  and density  $\rho_{uo}$  ahead of the shock corresponding to the flame temperature  $T_{bo} = T_{uo} + q_m/c_p$ . It is more convenient in the self-similar solutions to express the Arrhenius factor of (5.13) in the form

$$\begin{aligned} \bar{T}_{bf} - \bar{T}_{uf} &= q_m/c_p = T_{bo} - T_o, \\ \Rightarrow e^{-\frac{E_a}{2k_B} \left( \frac{1}{T_b} - \frac{1}{T_{bo}} \right)} &= e^{\frac{1}{2} \frac{E_a}{k_B T_{bo}} \frac{\bar{T}_{bf} - T_{bo}}{\bar{T}_{bf}}} = e^{\frac{1}{2} \frac{E_a}{k_B T_{bo}} \frac{\bar{T}_{uf} - T_o}{T_o} \left[ \frac{T_{bo}}{T_o} + \frac{\bar{T}_{uf} - T_o}{T_o} \right]^{-1}}. \end{aligned} \quad (5.14)$$

For very energetic mixtures the temperature ratio  $T_b/T_u \approx 10$  is of the same order of magnitude as the activation energy reduced by the initial temperature  $E_a/k_B T_{uo} \approx 20$ , the latter insuring that the initial mixture is frozen far from the chemical equilibrium. Therefore the activation energy reduced by the enthalpy of the burned gas  $E_a/k_B T_b$  is of order unity, and the exponential factor in (5.13) does not represent a strong variation of the laminar flame-speed with the flame temperature. With the Zeldovich number being of order unity  $\beta_b \approx 2$ , equations (5.9-5.13) might be questionable (since the ZFK analysis was done in the limit of large  $\beta_b$ ), but they can still be employed with reasonable accuracy. The precise functional dependence of  $U_L$  on the burnt-gas temperature  $T_b$  is indeed not essential in our analysis, see the discussion below (5.31). For example, equation (5.13) can be replaced by the  $T_b$ -dependence of  $U_L$  issued from the numerical study of the steady flame-structure. It turns out that (5.13) provides a good fit with the DDT experiments [30, 78], see §5.4.

### 5.3 Self-similar solutions

According to the experimental results [30, 77–79], the abrupt transition to detonation occurs for Mach numbers of the lead shock of order unity  $M \in [2.5, 3.5]$  which are too small for self ignition of the fresh mixture. For the purpose of comparison with the experimental data, we determine in this section the turning of the self-similar solutions obtained with the one-dimensional piston model of Figure 5.3.

#### 5.3.1 Quasi-steady approximation and nonlinear equation

Consider the self-similar solution of the double discontinuity model when the acceleration of the tip of the elongated flame is neglected,  $U_f \approx \text{cst}$ ,  $\bar{u}_{uf} \approx \text{cst}$ . More precisely, according to (5.8), the change of the flame velocity is assumed to be sufficiently slow for making the unsteady compressible effects ahead of the flame front negligible. The flow of fresh mixture is considered as quasi-uniform and quasi-steady in the region delimited by the planar flame and the lead-shock propagating upstream with a constant supersonic velocity  $\mathcal{D}$ ,  $M \equiv \mathcal{D}/a_o > 1$ , the subscript  $o$  denoting the fresh gas ahead of the shock wave. In other words the interaction between the flame and the lead shock is considered as instantaneous in the self-similar solutions. This cannot be the case in the vicinity of the turning point where the flame acceleration involves timescales shorter than the transit time of the acoustic waves between the two fronts, see §5.5 and §5.6.

The feedback of the lead shock on the flame is obtained by the Rankine-Hugoniot relations (2.28–2.30) at the Neumann state (denoted by the subscript  $N$ ), expressing the density and temperature of the fresh mixture ahead the flame  $\bar{\rho}_{uf} = \rho_N$ ,  $\bar{T}_{uf} = T_N$  in terms of the Mach number  $M$  of the shock:

$$\begin{aligned} \frac{\rho_o}{\rho_N} &= \frac{(\gamma - 1)M^2 + 2}{(\gamma + 1)M^2}, \\ \frac{u_N}{a_o} &= \frac{2}{\gamma + 1} \left[ M - \frac{1}{M} \right], \\ \frac{T_N}{T_o} &= \frac{2\gamma}{(\gamma + 1)^2} \left[ 1 - \frac{\gamma - 1}{2\gamma M^2} \right] [2 + (\gamma - 1)M^2], \end{aligned} \quad (5.15)$$

showing that the temperature jump  $T_N/T_o - 1$  increases with the flow velocity  $u_N$ . The laminar flame speed  $U_L(\bar{\rho}_{uf}, \bar{T}_{uf})$  in (5.13) can then be expressed in terms of  $M$ . For a given length of the elongated flame  $L/R$ , according to the second relation in (5.15) and (5.4) in which the quasi-isobaric approximation of the flame structure  $\bar{\rho}_{uf}/\bar{\rho}_{bf} = (\bar{T}_{uf} + q_m/c_p)/\bar{T}_{uf}$  is used, the intensity of the shock is found to depend in turn on the flame velocity through the flow of fresh mixture  $\bar{u}_{uf} = u_N$ , leading to a nonlinear equation for  $M$  characterized by a turning point.

#### 5.3.2 Solution of the piston model using the DJ approximation

Although the approximations used by DJ [27] are not valid at the critical condition of elongated flames in tubes filled with an energetic mixture, as a first step it is worth considering the problem in the DJ limit. This simplified approach provides instructive physical insight, showing the relevance of the piston model and explaining why the DJ approximation is not accurate. For a weak shock  $M - 1 \ll 1$ , neglecting the terms of order  $(M - 1)^2$  in (5.15), the temperature  $\bar{T}_{uf}$  and the flow velocity  $\bar{u}_{uf}$  ahead

of the flame are linearly related. This is the key simplification of the DJ analysis

$$0 < M - 1 \ll 1 : \quad \begin{aligned} \frac{\bar{p}_{uf}}{p_o} - 1 &\approx \gamma \frac{\bar{u}_{uf}}{a_o} = \frac{4\gamma}{\gamma + 1} (M - 1) + \dots, \\ \frac{\bar{T}_{uf}}{T_o} - 1 &= (\gamma - 1) \frac{\bar{u}_{uf}}{a_o} + \dots, \end{aligned} \quad (5.16)$$

the only non-linearity left in the problem being the high sensitivity of the flame speed to the flame temperature, which is not the case for very energetic mixtures as explained in §5.2.2. For a large reduced activation energy, the Arrhenius factor (5.14) takes the form

$$\begin{aligned} E_a/k_B T_{bo} \gg 1 : \quad & \frac{E_a}{k_B T_{bo}} \frac{\bar{T}_{uf} - T_o}{T_{bo}} = O(1) \\ \Rightarrow & e^{-\frac{E_a}{k_B} \left( \frac{1}{T_b} - \frac{1}{T_{bo}} \right)} \approx e^{\frac{1}{2} \frac{E_a}{k_B T_{bo}} \frac{T_o}{T_{bo}} \frac{\bar{T}_{uf} - T_o}{T_o}}. \end{aligned} \quad (5.17)$$

On the one hand, introducing the last equation (5.16) into (5.17), equation (5.13) then gives an expression of the laminar flame speed in terms of the flow velocity  $\bar{u}_{uf}$

$$0 < M - 1 \ll 1 : \quad U_L/U_{Lo} = e^{\frac{1}{2} \frac{E_a}{k_B T_{bo}} \frac{T_o}{T_{bo}} (\gamma - 1) \frac{\bar{u}_{uf}}{a_o}}. \quad (5.18)$$

On the other hand, in the piston model, the flow velocity  $\bar{u}_{uf}$  is expressed in terms of the laminar flame speed  $U_L$  and the length  $L$  of the elongated flame by the first equation in (5.4) in which the density ratio is approximated by  $\bar{\rho}_{uf}/\bar{\rho}_{bf} \approx T_{bo}/T_o$  in agreement with the approximation  $M - 1 \ll 1$

$$\frac{\bar{u}_{uf}}{U_L} \approx \frac{T_{bo}}{T_o} \left[ 2 \frac{L}{R} + \frac{T_{bo} - T_o}{T_{bo}} \right]. \quad (5.19)$$

Introducing (5.19) into (5.18) yields a nonlinear equation for  $U_L/U_{Lo}$  in terms of  $L/R$

$$0 < M - 1 \ll 1 : \quad U_L/U_{Lo} = e^{\frac{1}{2} \frac{E_a}{k_B T_{bo}} (\gamma - 1) \frac{U_{Lo}}{a_o} \left[ (2L/R + 1) - \frac{T_o}{T_{bo}} \right] \frac{U_L}{U_{Lo}}}, \quad (5.20)$$

which, using the notation  $m \equiv U_L/U_{Lo}$ , can be written in a form similar to (19) and (20) in [27]

$$m = e^{Sm} \quad \text{where} \quad S \equiv b \left[ 2 \frac{L}{R} + \frac{T_{bo} - T_o}{T_{bo}} \right] \quad \text{and} \quad b \equiv \frac{(\gamma - 1)}{2} \frac{E_a}{k_B T_{bo}} \frac{U_{Lo}}{a_o} \ll 1. \quad (5.21)$$

The relation  $b \ll 1$  comes from the fact that the laminar flame speed is substantially subsonic  $U_{Lo}/a_o \ll 1$ , see (5.9). Using a similar distinguished limit as in the DJ analysis of turbulent flame  $S = O(1)$ , the same turning point is exhibited by (5.21) for the piston model; there is no solution for an elongation  $S$  above a critical value  $S^* = 1/e$ ,  $m^* = e$ , while two solutions exist below, for  $m < m^*$ ,  $S < S^* = 1/e$ , the physical solution being the one for which the unperturbed velocity  $U_{Lo}$  is recovered when the thermal effect (5.16) vanishes  $\bar{T}_{uf} \rightarrow T_o$ ,  $\bar{u}_{uf} \rightarrow 0$ ,  $\lim_{S \rightarrow 0} U_L/U_{Lo} = 1$ . The laminar flame velocity  $U_L$  of the physical solutions  $m \leq m^*$  is still markedly subsonic,  $U_L^* = e U_{Lo}$ . According to (5.21), the critical length of the elongated flame  $L^*$  is substantially larger than the radius of the tube  $L^*/R \approx 1/(2eb)$ , the first condition in (5.8) requiring  $(E_a/k_B T_{bo}) \sqrt{T_o/T_{bo}} (\gamma - 1)/2 \gg 1/e$ .

Two main conclusions can be drawn from this simple calculation. Firstly, the back flow of the elongated flame is essential to reach a critical condition at the tip; this follows from (5.21) showing that the critical condition can never be attained by a planar flame propagating from the closed end of a tube when the burnt gas is at rest  $\bar{u}_{bf} = 0$ , the scalar  $S$  being well below the critical value  $1/e$  for

$L = 0$ ,  $S = b(T_{bo} - T_o)/T_{bo}$ , still too small by a factor  $10^{-1}$  for  $U_{Lo}/a_o \approx 1.6 \cdot 10^{-2}$ ,  $T_{bo}/T_o = 10$ ,  $E_a/k_B T_b \approx 10$ ,  $\gamma = 1.4 \Rightarrow b \approx 0.032$ . However, for such a energetic mixture, according to (5.21), the critical elongation of the flame front is not very large,  $2L^*/R + (T_{bo} - T_o)/T_{bo} = 1/(be) \approx 10.5$ ,  $L^*/R \approx 5$ . Secondly, according to (5.16), the critical flow  $\bar{u}_{fu}^* \approx 1.76 a_o$  is supersonic yielding a Mach number of the lead shock close to 2, in contradiction with the assumption  $M - 1 \ll 1$ . Therefore, the weak shock approximation (5.16) cannot be used near the critical condition, and one has to be back to the full Rankine-Hugoniot conditions (5.15).

### 5.3.3 Critical condition for very energetic elongated flames

A nonlinear equation for  $M$  is obtained by the method explained at the end of §5.3.1. Assuming that the heat release and the specific heat capacity are constant,  $\bar{T}_{bf} - \bar{T}_{uf} = T_{bo} - T_o = q_m/c_p$ , the density and temperature ratios  $\bar{\rho}_{uf}/\bar{\rho}_{bf}$  and  $\bar{T}_{bf}/T_{bo}$  to be introduced into (5.4) and (5.13), respectively, are expressed in terms of  $\bar{T}_{uf}/T_o$

$$\frac{\bar{\rho}_{uf}}{\bar{\rho}_{bf}} = \frac{\bar{T}_{bf}}{\bar{T}_{uf}} = 1 + \frac{\bar{T}_{bf} - \bar{T}_{uf}}{\bar{T}_{uf}} = 1 + \frac{(T_{bo} - T_o)}{\bar{T}_{uf}} = 1 + \frac{q_m/c_p T_o}{\bar{T}_{uf}/T_o}, \quad (5.22)$$

$$\frac{\bar{T}_{bf}}{T_{bo}} = \frac{\bar{T}_{uf} + q_m/c_p}{T_o + q_m/c_p} = \frac{\bar{T}_{uf}/T_o + q_m/(c_p T_o)}{1 + q_m/(c_p T_o)}, \quad (5.23)$$

which can be written by using the short notation  $y \equiv \bar{T}_{uf}/T_o > 0$  and  $q \equiv q_m/c_p T_o > 1$  as

$$\frac{\bar{\rho}_{uf}}{\bar{\rho}_{bf}} = 1 + \frac{q}{y}, \quad \frac{\bar{T}_{bf}}{T_{bo}} = \frac{y + q}{1 + q}, \quad \text{where } y \equiv \frac{\bar{T}_{uf}}{T_o} \quad \text{and} \quad q \equiv \frac{q_m}{c_p T_o} = \frac{T_{bo} - T_o}{T_o}. \quad (5.24)$$

According to the Rankine-Hugoniot equation in (5.15) for  $T_N/T_o$  and using the relation  $\bar{T}_{uf} = T_N$ , the scalar  $y$  in (5.24) is a function of  $M^2$ . The algebra in (5.15) simplifies by anticipating that  $\gamma - 1 \approx 0.3 - 0.4$  is negligible in comparison to  $2\gamma M^2$  near criticality, which is the case as soon as  $M^* \gtrsim 2$ ,

$$\begin{aligned} \frac{2\gamma M^2}{\gamma - 1} \gg 1 : \quad \frac{\bar{T}_{uf}}{T_o} &\approx \frac{2\gamma}{(\gamma + 1)^2} [2 + (\gamma - 1)M^2], \\ y(M^2) &= \frac{2\gamma}{(\gamma + 1)^2} [2 + (\gamma - 1)M^2]. \end{aligned} \quad (5.25)$$

The flow velocity  $\bar{u}_{uf}$  generated ahead of the flame by the piston effect (5.4),

$$\frac{\bar{u}_{uf}}{a_o} \approx \frac{U_L}{U_{Lo}} \frac{U_{Lo}}{a_o} \left[ \left(1 + \frac{q}{y}\right) \sigma - 1 \right] \quad \text{where} \quad \sigma \equiv \frac{2L}{R} + 1, \quad (5.26)$$

then takes the form of a function of  $M^2$  when the ratio  $U_L/U_{Lo}$  is expressed in terms of  $y$  ( $M^2$ ) by using (5.13) in which, according to (5.24),  $1/\bar{T}_{bf} - 1/T_o = (1/T_o)(1 - y)/(y + q)$

$$\frac{\bar{u}_{uf}}{a_o} = \frac{U_{Lo}}{a_o} \left[ \left(1 + \frac{q}{y}\right) \sigma - 1 \right] \left( \frac{y + q}{1 + q} \right)^{1+\nu/2} y^{(1+\nu)/2} \exp \left[ \frac{\beta_o(y - 1)}{(y + q)} \right] \quad (5.27)$$

where

$$\beta_o \equiv \frac{E_a}{2k_B T_{bo}} = O(1). \quad (5.28)$$

For a given reactive mixture characterized by the set of parameters ( $U_{Lo}/a_o$ ,  $q$ ,  $\beta_o$  and  $\gamma$ ), the first Rankine-Hugoniot relation (5.15)  $u_N/a_o = \bar{u}_{uf}/a_o = 2(M - 1/M)/(\gamma + 1)$ , combined with (5.27),

leads to a nonlinear equation for  $M$  parametrized by the parameter  $\sigma$  characterizing the elongation  $L/R$ . This equation takes a simpler form if  $(1 + q/y)\sigma \gg 1$  which is the case for a large heat release  $q \approx 10$  (very energetic mixture) so that the elongation of the flame  $\sigma = 2L/R + 1$  appears as a factor in the right-hand side of (5.27). The equation for  $M$  then takes the form

$$\Lambda^{-1}\mathcal{L}(M) = \mathcal{R}(M), \quad (5.29)$$

where

$$\mathcal{L}(M) \equiv \frac{M - 1/M}{1 + q/y}, \quad \Lambda \equiv \frac{\gamma + 1}{2} \frac{U_{Lo}}{a_o} \sigma, \quad (5.30)$$

and

$$\mathcal{R}(M) \equiv \frac{U_L}{U_{Lo}} = \left( \frac{y + q}{1 + q} \right)^{1+\nu/2} y^{(1+\nu)/2} \exp \left[ \frac{\beta_o(y - 1)}{y + q} \right], \quad (5.31)$$

where the elongation  $\sigma$  appears only in the coefficient  $\Lambda$  and the laminar flame-speed  $U_L$  only in  $\mathcal{R}(M)$ . According to (5.25),  $\mathcal{L}(M)$  and  $\mathcal{R}(M)$  are increasing functions of  $M$  in the range  $M > 1$ , involving two parameters (in addition to the ratio of specific heats  $\gamma$ ), the reduced heat release  $q \approx 10$  and the reduced activation energy  $\beta_o \approx 2$  for very energetic mixtures.

The roots of (5.29) correspond to the intersection of the two curves  $\Lambda^{-1}\mathcal{L}(M)$  and  $\mathcal{R}(M)$ . For  $M - 1 \rightarrow 0^+$  the function  $\mathcal{L}(M)$  goes to zero while  $\mathcal{R}(M)$  approaches unity. The key point is that the function  $\mathcal{R}(M)$  increases more rapidly than  $\mathcal{L}(M)$  when  $M$  increases. This is true for the laminar flame-speed of any energetic mixture, so that the method is not limited to the particular expression (5.13) of  $U_L/U_{Lo}$  used in (5.31). When the parameter  $\Lambda$  is too large, namely for either a large elongation  $\sigma$  or a large flame-speed  $U_{Lo}/a_o$ , the function  $\Lambda^{-1}\mathcal{L}(M)$  is smaller than  $\mathcal{R}(M)$  everywhere  $\forall M \geq 1$  so that equation (5.29) has no roots and there is no self-similar solution of the complex flame-shock, see Figure 5.4.

Decreasing  $\Lambda$ , a critical value  $\Lambda^*$  is obtained when the two curves become tangent at a critical value  $M^*$  corresponding to a turning point of the self-similar solution like in §5.3.2. For a small elongation  $\Lambda < \Lambda^*$  there are two solutions and the physical one belongs to the branch for which the elongation  $L/R$  decreases with  $M - 1$ . The critical elongation corresponding to  $\Lambda^*$  is easily obtained as follows. For typical values of the parameters ( $\Lambda$ ,  $q$ ,  $\beta_o$ ,  $\gamma$ ), the ratio  $\mathcal{R}(M)/\mathcal{L}(M)$  goes through a minimum when  $M$  increases from  $M = 1$ , it first decreases and then increases. This is because the function  $\mathcal{R}(M)$  increases more strongly than  $\mathcal{L}(M)$  for large  $M$ , but  $\mathcal{L}(M)$  goes to zero in the opposite limit  $M - 1 \rightarrow 0^+$  while  $\mathcal{R}(M)$  goes to a number close to unity. The minimum of  $\mathcal{R}(M)/\mathcal{L}(M)$  corresponds to the critical Mach number  $M = M^*$  yielding the critical elongation  $\Lambda^*$  given by the ratio  $\mathcal{R}(M^*)/\mathcal{L}(M^*) = 1/\Lambda^*$ .

## 5.4 Comparison with the experimental data

In this section, the critical condition obtained from (5.29-5.31) is compared with the DDT experiments [30, 78] in which DDT is observed for  $M \in [2, 3]$ . Using a set of parameters corresponding to very energetic mixtures similar to those used in these experiments,  $U_{Lo} = 8.54$  m/s ( $U_{Lo}/a_o = 0.016$ ),  $T_b/T_o = 10$  ( $q = 9$ ),  $E_a/k_B T_o = 25$  ( $\beta_o = 1.25$ ),  $\nu = 2$  and  $\gamma = 1.4$ , the critical condition for the loss of self-similarity obtained from (5.29-5.31) is  $M^* = 2.44$  and  $\Lambda^* = 0.089$  (see Figure 5.4), that is  $\sigma^* = 4.63$ . The corresponding critical values of the temperature ratio  $\bar{T}_{uf}^*/T_o$  and the flame velocity in the laboratory frame  $U_f$  are  $\bar{T}_{uf}^*/T_o = 2.19$  and  $U_f^* = 928$  m/s respectively. These values are in good agreement with  $M$  and  $U_f$  measured just before the abrupt transition observed in the experiments [30, 78], the DDT occurring near the tip of the curved flame front at the end of a second stage of

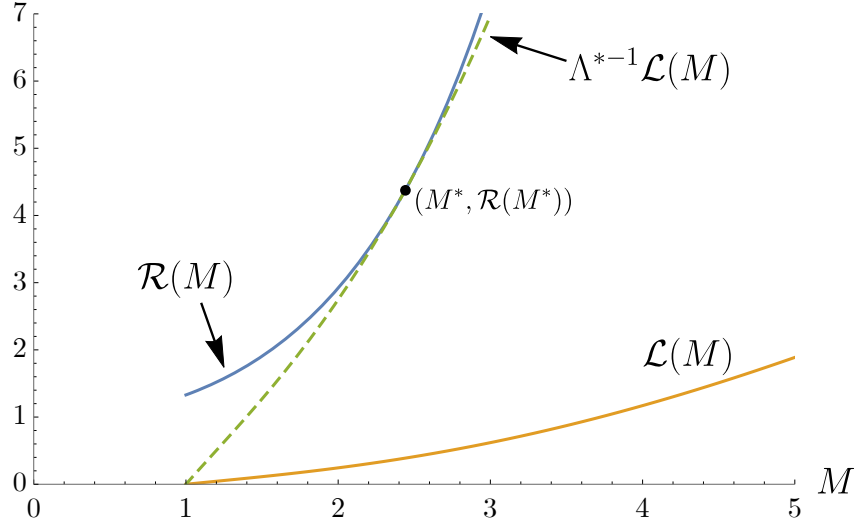


Figure 5.4: Plots of  $\mathcal{L}(M)$  in (5.29) and  $\mathcal{R}(M)$  in (5.31) for  $\gamma = 1.4$ ,  $q = 9$  and  $\beta_o = 1.25$ . The turning point of the self-similar solution is  $M^* = 2.44$ ,  $\Lambda^* = 0.089$ .

flame acceleration (sometimes after the transient formation of a tulip shape). Moreover  $\sigma^* = 4.63$  leads to a small elongation  $L^*/R \approx 2$  which is in relatively good agreement with the curved flame front at the transition visualized by shadow photographs. Interesting enough is the large flow velocity of gas ahead of the flame  $\bar{u}_{u_f}^* = 891$  m/s which is supersonic  $\bar{u}_{u_f}^*/\bar{a}_{u_f}^* = 1.13$  ( $\bar{a}_{u_f}^*/a_o = 1.48$ ) but subsonic relatively to the lead shock at it should be  $(\mathcal{D}^* - \bar{u}_{u_f}^*)/\bar{a}_{u_f}^* \approx 0.5$ . Moreover the laminar flame velocity at the transition  $U_L^*/U_{L_o} = 4.62$  is still markedly subsonic  $U_L^* = 39$  m/s,  $U_L^*/\bar{a}_{u_f}^* \approx 0.05$ . All these values are in good agreement with the experiments. The large ratio  $\bar{u}_{u_f}^*/U_L^* \approx 23.6$  is due to the large density ratio across the laminar flame in a very energetic mixture  $\bar{\rho}_u/\bar{\rho}_b \approx 10$ .

To conclude, the sudden DDT of self-accelerating elongated flames propagating in tubes filled with very energetic mixtures seems to occur near the critical condition corresponding to the turning point of the self-similar solutions obtained with the planar piston model. Notice that the latter is independent of the rate of elongation of the finger flame, the critical condition concerning the elongation not its rate. A tentative explanation is provided in the next sections.

## 5.5 Finite-time singularity

A runaway of the acceleration of the flame front (not of its speed) in the self-similar solutions occurs systematically at the turning point when the elongation increases with the time  $\sigma(t)$ . Introducing the notations  $\mathcal{L}'(M)$  and  $\mathcal{R}'(M)$  for  $d\mathcal{L}(M)/dM$  and  $d\mathcal{R}(M)/dM$  respectively, the time derivative of equation (5.29) where  $\Lambda(t)$  is proportional to  $\sigma(t)$ ,

$$[\mathcal{L}'(M) - \Lambda \mathcal{R}'(M)] \frac{dM}{dt} = \mathcal{R}(M) \frac{d\Lambda}{dt} \quad (5.32)$$

shows that the derivative  $dM/dt$  increases when the critical value  $M^*$  is approached from below and diverges at  $M = M^*$ ,  $\lim_{M \rightarrow M^*} dM/dt = \infty$ . The tangency of the two curves at the critical root  $M^*$  of  $\mathcal{L}(M) = \Lambda(t) \mathcal{R}(M)$  corresponds to  $\mathcal{L}'(M^*) = \Lambda^* \mathcal{R}'(M^*)$  so that the factor of  $dM/dt$  on the left-hand side of (5.32) vanishes while the left-hand side is finite. Expanding the factor on the left-hand side in

powers of  $M - M^*$ , equation (5.32) takes the form

$$(M - M^*) \frac{dM}{dt} = k_{M^*} \left( \frac{d\Lambda}{dt} \right)_{\Lambda=\Lambda^*} \quad (5.33)$$

where  $k_{M^*}$  is a constant proportional to the inverse of the difference between the second derivatives at the turning point  $d^2\mathcal{L}/dM^2|_{M=M^*} - \Lambda^* d^2\mathcal{R}/dM^2|_{M=M^*}$ . The flame velocity in the laboratory frame  $U_f(t)$  satisfies a similar equation near the critical condition

$$U_f \leq U_f^*, \quad \frac{(U_f - U_f^*)}{U_f^*} \frac{dU_f}{dt} = \text{constant} \quad (5.34)$$

where, according to the expression of  $\Lambda$  in (5.29), the constant is proportional to  $U_{Lo}/a_o$  and to the growth rate of the elongation at criticality  $1/t_e^* \equiv (1/\sigma^*) d\sigma/dt|_{\sigma=\sigma^*}$ . This growth rate appears here for the first time in the analysis. Introducing the time  $t^*$  at which the critical speed is reached  $M(t^*) = M^*$ ,  $U_f(t^*) = U_f^*$ ,  $\bar{u}_{uf}(t^*) = \bar{u}_{uf}^*$ , integrating (5.34) yields

$$t - t^* \rightarrow 0^- : \quad \frac{(U_f^* - U_f)}{U_f^*} \propto \sqrt{\frac{t^* - t}{t_e^*}}, \quad \frac{\tau^*}{U_f^*} \frac{dU_f}{dt} \propto \sqrt{\frac{t_e^*}{t^* - t}}, \quad (5.35)$$

$$\frac{(\bar{u}_{uf}^* - \bar{u}_{uf})}{\bar{u}_{uf}^*} \propto \sqrt{\frac{t^* - t}{t_e^*}}, \quad \frac{\tau^*}{\bar{u}_{uf}^*} \frac{d\bar{u}_{uf}}{dt} \propto \sqrt{\frac{t_e^*}{t^* - t}}, \quad (5.36)$$

showing the runaway of the accelerations of the flame front  $dU_f/dt$  and of the gas-flow  $d\bar{u}_{uf}/dt$  when the critical condition is approached. Notice that the runaway is always produced regardless of the elongation rate  $1/t_e^* \equiv \sigma^{-1}(d\sigma/dt)|_{\sigma=\sigma^*}$ , the square-root scaling law taking a universal form (free from parameters) when using the reduced time  $\tau \equiv t/t_e^*$ . The acceleration of the laminar flame speed  $dU_L/dt$  and/or  $dU_b/dt$  also diverges according to the same scaling laws as (5.35-5.36), the critical values  $U_L^*$  and  $U_b^*$  being markedly subsonic.

## 5.6 Beyond self-similarity: formation of a shock on the flame front

For the self-similar solutions to be valid, the compressible waves should be fast to make the flow quasi-uniform and quasi-steady. More precisely the transit time of acoustic waves in both directions between the flame and the lead shock should be shorter than the time scale of the modifications of the flame velocity. This assumption is no longer valid for large accelerations of the flame, in particular near the turning point where the acceleration diverges. The two-dimensional numerical simulations of Liberman and coworkers [30, 74] show a succession of compression waves steepening into shocks ahead of the flame in close proximity to its front. A shock seems to sit at the tip of the elongated flame just before DDT. The flame propagating with a subsonic speed (relative to the upstream gas) while the shock is supersonic, a shock is more likely to be formed spontaneously inside the inner flame structure producing quasi-instantaneously the blow-up of the flame structure before escaping into the unreacted gas. A thorough understanding of the abrupt DDT of a self-accelerating flame near the turning point requires the full solution of the unsteady problem, including the inner structure of the laminar flame. Unfortunately unsteadiness of the inner structure can be solved analytically only for much milder situations [84]. The study should be performed numerically in a one-dimensional geometry within the framework of the piston model using the high-order spectral difference flow solver. This might be the

subject of future studies, though here we limit our attention to the simple waves that are generated in the fresh gas by the large acceleration of a piston approaching the critical velocity of the turning point. The objective is to show that the unsteady compressible waves lead to the formation of a singularity of the flow on the piston when the piston velocity reaches the critical value.

### 5.6.1 Theoretical analysis

Using the characteristics method of Riemann [85], an analytical solution of the isentropic Euler equations can be obtained for the simple waves issued from a piston starting to move in an inert gas initially at rest. Following the presentation in [42], the flow  $u(x, t)$  of a simple compression wave propagating from right to left in a perfect gas, written in a Galilean frame where  $\lim_{x \rightarrow \infty} u = 0$ , is solution of the equation

$$x = \left[ \frac{\gamma + 1}{2} u + a_\infty \right] t + F(u) \quad (5.37)$$

where  $a_\infty$  is the initial sound speed of the gas at rest and  $F(u)$  is a function of the flow velocity given by the condition at the piston

$$x = X_p(t) : \quad u(X_p(t), t) = U_p(t) = dX_p/dt. \quad (5.38)$$

Limited to isentropic conditions, this solution is no longer valid after the apparition of a singularity in the flow gradient. The known function  $X_p(t)$  increasing monotonously with the time, the function  $F(u)$  is obtained through the inverse functions  $t = t_p(U_p)$  and  $x = X_p(u_p)$ , corresponding to  $U_p(t)$  and  $X_p(t)$  respectively. For a power law  $X_p(t) \propto t^{n+1}$  with  $n > 1$  for  $t \geq 0$  and  $dX_p/dt = 0$  for  $t < 0$ , the initial acceleration is zero  $d^2 X_p/dt^2|_{t=0^+} = 0$ . Then, the flow gradient  $\partial u/\partial x$  diverges at a finite distance ahead the piston after a finite time, indicating the place and time of formation of the shock wave.

This is no longer the case for  $n < 1$  since the singularity of the initial acceleration of the piston velocity  $d^2 X_p/dt^2|_{t=0^+} = \infty$  causes the shock to be formed instantaneously on the piston. None of these cases correspond to an accelerating flame approaching the critical velocity of a turning point, but the divergence of the acceleration suggests that a shock will be formed on the piston when the piston velocity reaches the critical value.

In order to check this possibility, consider a piston propagating in an inert gas with a velocity  $U_P(t)$  following the scaling law (5.35) written, using the non-dimensional time  $\tau = t/t_e^*$ ,  $\tau^* \equiv t^*/t_e^*$ , in the form

$$0 < \tau \leq \tau^* : \quad \frac{U_P^* - U_P}{U_P^*} = \sqrt{\tau^* - \tau}, \quad \frac{1}{U_P^*} \frac{dU_P}{d\tau} = \frac{1}{2} \frac{1}{\sqrt{\tau^* - \tau}}, \quad (5.39)$$

with typically  $U_P^* = 1.2 a_\infty$  as in the flame problem considered in §5.4. In order to stress the effect of the divergence of the acceleration at the turning point, consider the scaling law (5.39) for  $\tau \geq 0$  with a constant velocity of the piston for  $\tau \leq 0$  :  $U_P(\tau) = U_P(0)$ , the flow being constant and uniform  $\tau \leq 0$  :  $u(x, \tau) = U_P(0)$ . The piston starting to accelerate at  $\tau = 0^+$ , the boundary condition of the flow at infinity is  $u_\infty \equiv \lim_{x \rightarrow \infty} u(x, \tau) = U_P(0) \forall \tau$ . According to (5.39)

$$\tau \leq 0 : \quad U_P(\tau) = U_P(0) \Rightarrow \frac{U_P^* - U_P(0)}{U_P^*} = \sqrt{\tau^*}. \quad (5.40)$$

so that, in the Galilean frame moving with the initial flow, equation (5.39) takes the form

$$0 < \tau \leq \tau^* : \quad 0 \leq \frac{U_P(\tau) - U_P(0)}{U_P^*} = \sqrt{\tau^*} - \sqrt{\tau^* - \tau}. \quad (5.41)$$

For  $\gamma$  fixed, there are only two free non-dimensional parameters in this problem

$$\tau^* \equiv t^*/t_e^* \quad \text{and} \quad m^* \equiv U_P^*/a_\infty. \quad (5.42)$$

The only length scale in the problem being  $l \equiv a_\infty t_e^*$ , one introduces the non-dimensional coordinate  $\xi$  and the non-dimensional position of the piston  $\xi_P(\tau)$

$$\xi \equiv x/(a_\infty t_e^*), \quad \xi_P(\tau) = X_P(t)/(a_\infty t_e^*) \quad (5.43)$$

so that, choosing the origin of the  $x$ -axis at the initial position of the piston, the trajectory of the piston, obtained by integrating the first equation in (5.39), takes the non dimensional form

$$0 < \tau \leq \tau^* : \quad \xi_P(\tau) = \left[ \tau\sqrt{\tau^*} + \frac{2}{3}(\tau^* - \tau)^{3/2} - \frac{2}{3}\tau^{*3/2} \right] m^*, \quad (5.44)$$

$$\xi_P(\tau) - \xi_P^* = \left[ -(\tau^* - \tau)\sqrt{\tau^*} + \frac{2}{3}(\tau^* - \tau)^{3/2} \right], \quad (5.45)$$

where

$$\xi_P^* \equiv \frac{X_P^*}{a_\infty t_e^*} = \frac{1}{3}\tau^{*3/2}m^*, \quad (5.46)$$

$X_P^* \equiv X_P(t^*)$  being the distance separating the final position of the piston at  $t = t^*$  from its initial position ( $t = 0$ ). Introducing the notations

$$\dot{\xi}_P(\tau) \equiv d\xi_P/d\tau = [U_P(t) - U_P(0)]/a_\infty, \quad \ddot{\xi}_P(\tau) \equiv d^2\xi_P/d\tau^2 = t_e^*(dU_P(t)/dt)/a_\infty \quad (5.47)$$

for the reduced velocity and acceleration of the piston in the Galilean frame, (5.41-5.45) read

$$0 < \tau \leq \tau^* : \quad \dot{\xi}_P(\tau) = \left[ \sqrt{\tau^*} - (\tau^* - \tau)^{1/2} \right] m^*, \quad \ddot{\xi}_P(\tau) = \frac{m^*}{2(\tau^* - \tau)^{1/2}}, \quad (5.48)$$

$$\tau = \tau^* : \quad \xi_P(\tau^*) = \frac{1}{3}\tau^{*3/2}m^*, \quad \dot{\xi}_P(\tau^*) = m^*\sqrt{\tau^*}, \quad (5.49)$$

$$\lim_{\tau \rightarrow \tau^*} \ddot{\xi}_P(\tau) = \frac{m^*}{2(\tau^* - \tau)^{1/2}},$$

$$\tau = 0^+ : \quad \xi_P(0) = 0, \quad \dot{\xi}_P(0) = 0, \quad \ddot{\xi}_P(0^+) = \frac{m^*}{2\tau^{*1/2}}, \quad (5.50)$$

$$\tau^* \leq 0 : \quad \xi_P(0) = 0, \quad \dot{\xi}_P(\tau) = 0, \quad \ddot{\xi}_P(\tau) = 0. \quad (5.51)$$

For a situation similar to the flame in §5.4, the piston is subsonic at the initial condition  $U_P(0)/a_\infty < 1$  and supersonic at criticality  $U_P(t^*)/a_\infty = m^* > 1$ . Introducing the non-dimensional flow velocity  $\nu(\xi, \tau)$  in the Galilean frame moving with  $U(0)$ ,

$$\nu(\xi, \tau) \equiv [u - U_P(0)]/a_\infty, \quad \xi \equiv x/(a_\infty t_e^*); \quad \tau \leq 0 : \nu = 0, \quad (5.52)$$

the boundary conditions at the piston and at infinity yield

$$0 < \tau \leq \tau^* : \quad \nu_P(\tau) \equiv \nu(\xi_P(\tau), \tau) = \dot{\xi}_P(\tau) - \dot{\xi}_P(0) = \left[ \tau^{*1/2} - (\tau^* - \tau)^{1/2} \right] m^* \quad (5.53)$$

$$\tau = \tau^* : \quad \nu_P^* \equiv \nu(\xi_P(\tau^*), \tau^*) = \tau^{*1/2}m^*, \quad \xi \rightarrow \infty : \nu = 0 \quad \forall \tau. \quad (5.54)$$

In this frame, the non-dimensional velocity of the piston  $\dot{\xi}_P(\tau)$  in (5.47), is initially null  $\dot{\xi}_P(0) = 0$  and, according to (5.49), becomes supersonic at  $\tau = \tau^*$ ,

$$\frac{U_P^* - U_P(0)}{a_\infty} > 1 \quad \text{if} \quad \frac{1}{m^*} < \tau^{*1/2} \quad \Rightarrow \quad \dot{\xi}_P(\tau^*) > 1, \quad (5.55)$$

but the piston velocity is systematically smaller than the sound speed on the piston  $a_P(\tau) \equiv a(\xi_P, \tau)$  which is larger than  $a_\infty$ ,  $a_P(\tau) > a_\infty$ , the sound speed decreasing monotonously with the temperature in the compression wave from  $\xi = \xi_P$  to infinity,  $\lim_{\xi \rightarrow \infty} a(\xi, \tau) = a_\infty$ .

Formation of a shock in a finite time  $\tau = \tau_s$  is produced by the acceleration of the piston which presents a jump  $m^*/(2\sqrt{\tau^*})$  at the initial condition, see (5.50-5.51). An analytical expression of  $\tau_s$  can be obtained following the method in [42]. Introducing the constant term  $\xi_P^*$ , the reduced form of (5.37) takes the form

$$\xi - \xi_P^* = \left[ \left( \frac{\gamma+1}{2} \right) (\nu_P^* - \nu) - \left( \frac{\gamma+1}{2} \right) \nu_P^* - 1 \right] [(\tau^* - \tau) - \tau^*] + f(\nu). \quad (5.56)$$

The function  $f(\nu_P)$  is computed by the boundary condition at the piston  $\xi = \xi_P(\tau)$ :  $\nu = \nu_P(\tau)$  after eliminating  $\tau$  in favor of  $\nu_P(\tau)$  using (5.53-5.54),  $(\tau^* - \tau) = (\nu_P^* - \nu_P)^2/m^{*2}$  and (5.45) in the form

$$\xi_P - \xi_P^* = \left[ -\frac{(\nu_P^* - \nu_P)^2}{m^2} \sqrt{\tau^*} + \frac{2}{3} \frac{(\nu_P^* - \nu_P)^3}{m^3} \right] m. \quad (5.57)$$

Introducing the expressions  $(\tau^* - \tau) = (\nu_P^* - \nu_P)^2/m^{*2}$  and (5.57) respectively into the right-hand side and the left-hand side of (5.56) yields the expression of  $f(\nu_P)$  leading to

$$f(\nu) = \left( \frac{2}{3} - \frac{\gamma+1}{2} \right) \frac{(\nu_P^* - \nu)^3}{m^{*2}} + \left( \frac{\gamma+1}{2} \nu_P^* + 1 - m^* \sqrt{\tau^*} \right) \frac{(\nu_P^* - \nu)^2}{m^{*2}} - \frac{\gamma+1}{2} \tau^* \nu - \tau^*. \quad (5.58)$$

The relation  $f(0) = -m^* \tau^{*3/2} = -\xi_P^*$  which is obtained from (5.58) by using (5.54)  $\nu_P^* = \tau^{*1/2} m^*$ , confirms that, according to (5.56), the trajectory in the medium at rest ( $\nu = 0$ ) of the leading edge of the compression wave is effectively  $\xi = \tau + \text{constant}$ , corresponding to a propagation velocity equal to the sound speed  $a_\infty$ . Using the notation  $f'(\nu) \equiv df/d\nu$ ,

$$f'(\nu) = -3 \left( \frac{2}{3} - \frac{\gamma+1}{2} \right) \frac{(\nu_P^* - \nu)^2}{m^{*2}} - 2 \left( \frac{\gamma+1}{2} \nu_P^* + 1 - m^* \sqrt{\tau^*} \right) \frac{(\nu_P^* - \nu)}{m^{*2}} - \frac{\gamma+1}{2} \tau^*, \quad (5.59)$$

the partial derivative of (5.56) with respect to  $\xi$

$$1 = \left[ \frac{\gamma+1}{2} t + f'(\nu) \right] \frac{\partial \nu}{\partial \xi} \quad (5.60)$$

shows that the time  $\tau = \tau_s$  and the velocity  $\nu = \nu_s$  at which the flow gradient diverges  $|\partial \nu / \partial \xi| = \infty$ , are linked by the relation

$$\tau_s = -\frac{2}{\gamma+1} f'(\nu_s). \quad (5.61)$$

According to (5.59), equation (5.61) is verified for  $\tau_s = \tau^*$ ,  $\nu = \nu^*$  and, according to (5.56), the place of formation of the singularity is the critical position of the piston  $\xi_s = \xi_P^*$ . This shows that a singularity of the flow is systematically formed on the piston at the critical time  $\tau = \tau^*$ .

However equation (5.56) is limited to isentropic flows and one has to check whether or not another singularity can be formed before  $\tau^*$ . It turns out that this is possible at the leading edge of the compression wave,  $\nu = 0$ . Substituting  $\xi_P^* = m^* \tau^{*3/2}$  and  $\nu = 0$  into (5.59) leads to  $f'(0) = -2\sqrt{\tau^*}/m^*$ . Therefore, according to (5.61), a singularity can be formed ahead of the piston ( $\nu = 0$ ) at time

$$\tau_s = \frac{4}{\gamma+1} \frac{\sqrt{\tau^*}}{m^*}, \quad (5.62)$$

which is earlier than  $\tau^*$  if

$$\frac{4}{\gamma + 1} \frac{1}{m^*} < \sqrt{\tau^*}. \quad (5.63)$$

This corresponds to a time  $t^*$  sufficiently long for reaching the critical velocity of the piston after the piston started to accelerate,  $t^*/t_e^* > [4/(\gamma + 1)]^2 a_\infty/U_P^*$ , which also corresponds to a sufficiently long distance separating the initial and final positions of the piston  $X_P^*/(a_\infty t^*) > 4/(\gamma + 1)$ . No other singularity can be formed for  $0 \leq \tau < \tau^*$  since no inflection of the flow field can be produced in the rarefaction wave simultaneously with  $|d\nu/d\xi| = \infty$ ,  $d^2f/d\xi^2 \neq 0$ . Therefore, the relation (5.63) corresponds to a first singularity formed ahead of the piston. The opposite condition

$$\sqrt{\tau^*} < \frac{4}{\gamma + 1} \frac{1}{m^*} \quad (5.64)$$

corresponds to a first singularity formed on the piston. Notice the difference between the two singularities, the latter being formed at the maximum flow velocity in the compression wave  $u = U_P^*$  while the other is formed at the minimum  $u = U_P(0)$  ( $\nu = 0$ ).

### 5.6.2 Numerical validation

These results are verified with an excellent accuracy by the direct numerical simulation (DNS) of the Euler equations using the high-order spectral difference solver with an adiabatic condition on the piston. The numerical implementation was discussed in §3.2. When, according to (5.63), a first singularity is formed ahead of the piston, the DNS shows that a second singularity of the flow gradient is systematically formed on the piston at the critical condition  $t = t^*$  (cf. Figure 5.5). If the piston velocity is kept fixed after the critical condition  $t > t^* : U_P = U_P^*$ , the supersonic velocity of the singularity on the piston being larger than  $U_P^*$ , this singularity leaves the piston to form the final shock wave corresponding to the self-similar solution, after a time proportional to  $t_e^*$ .

These results suggest that a shock is formed inside the inner flame structure on the tip of a self-accelerating elongated flame-front as soon as its velocity reaches the critical value of the turning point of the self-similar solutions<sup>1</sup>. However, for an abrupt DDT at the critical velocity of the self-similar solutions, the shock should be sufficiently strong to blow up the inner flame structure quasi-instantaneously before the shock escapes from the subsonic flame structure. This looks possible for gaseous mixtures that are sufficiently energetic even though an increasing flow inside the inner flame structure in the propagation direction (from the burnt to the unburnt gas side) is not in favor of shock formation. Therefore, the shock is expected to be formed at a point inside the premixed zone near the cold side where the initial gradient of the flow is not so large but the increase of temperature sufficiently large for producing fast self-ignition, which was not possible outside the flame structure where the temperature is too low. This fundamental problem of DDT shall be investigated numerically in future studies using the one-dimensional piston-model presented in §5.2.

## 5.7 Conclusion

The comparison of the theoretical results obtained with the one-dimensional piston-model in §5.2 for very energetic mixtures with the 2010 experiments [30, 78] shows that the sudden DDT at the tip of a

1. It could seem questionable to work beyond self-similarity near the critical condition using the scaling laws of the self-similar solutions. This is not so because the feedback of simple waves on the flame is similar to that of the lead shock in the self-similar solutions.

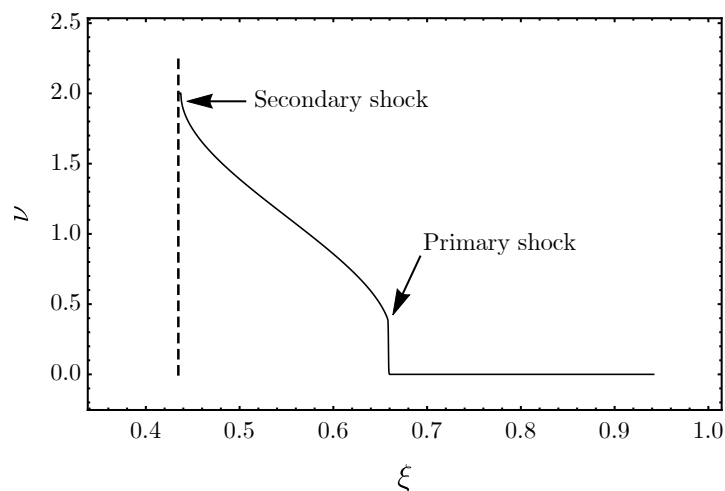
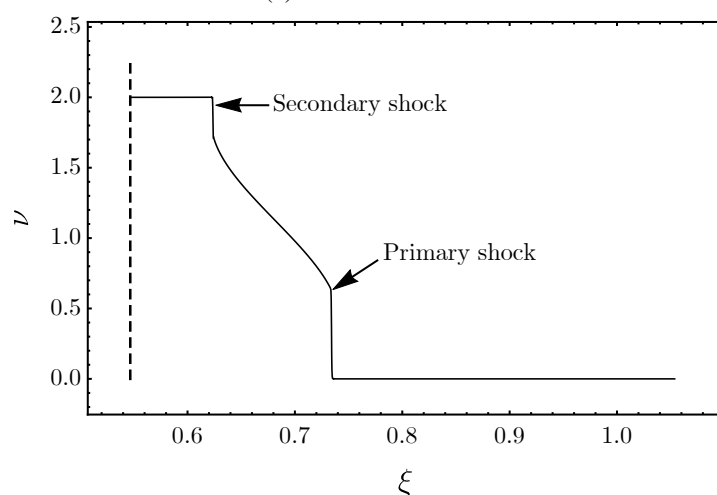
(a)  $\tau = \tau^* = 0.64$ (b)  $\tau = 0.7 > \tau^*$ 

Figure 5.5: Velocity profiles for the problem of shock formation by an accelerating piston (5.39), as obtained from DNS, with  $m^* = 2.5$  and  $\tau^* = 0.64$ . The dashed line represents the position of the piston, which is moving from right to left. (a) At  $\tau = \tau^*$ , the primary shock formed earlier at the tip of the compression wave can be observed, as well as the secondary shock forming at the piston. (b) The piston continues to move with a constant velocity after  $\tau^*$ , while the secondary shock is catching up with the primary one.

self-accelerating elongated flame occurs when the flame velocity reaches the critical value corresponding to the turning point of the self-similar solutions. This suggests that the double feedback mechanism presented here is involved in these experiments. An essential role is played by the back-flow of burnt gas towards the flame tip, all the more since the density ratio across laminar flames of very energetic mixtures is large and the thermal sensitivity of the laminar flame speed is weak.

In addition, the solutions of the upstream-running simple waves that are generated in an inert gas by an accelerating piston have shown that, due to the singularity of the acceleration at the turning point, a shock is formed on the piston when the critical velocity is reached. This suggests the formation of a shock wave inside the inner structure of the flame, in agreement with the multi-dimensional numerical

simulations [30, 74] performed by Liberman and co-authors in the experimental conditions. A detailed analysis of the sudden transition when a shock is formed inside the flame structure is left for future one-dimensional numerical simulations of DDT using the piston-model described in §5.2.

The small elongation of the flame at the critical condition, of the order of the tube diameter in §5.4, suggests that strongly cellular flames of very energetic mixtures could also experience DDT in free space.



# Chapter 6

## Conclusions and perspectives

### Sommaire

---

6.1 One-dimensional dynamics of detonations . . . . .	102
6.2 Deflagration-to-detonation transition of an elongated flame . . . . .	103

---

In this chapter, we summarize the main conclusions of the work and give some general perspectives for future studies.

### 6.1 One-dimensional dynamics of detonations

In Chapter 4, we revisited the one-dimensional model for detonation instability that was proposed by Clavin and Williams back 2002 [23]. The model, grounded on the existence of a feedback loop between the leading shock wave and the reaction zone, was analyzed in the asymptotic limit of low heat release coupled with the Newtonian approximation (ratio of heat capacities close to unity). The asymptotic analysis allowed us to simplify the problem so that the dynamics was only controlled by the upstream-running acoustic mode traveling from the reaction zone towards the shock. We then obtained an integral equation describing the fluctuation in the shock velocity  $y(\tau)$  as a result of the superposition of acoustic waves traveling from each point in the reaction zone towards the shock (equation (4.67)):

$$2y(\tau) = b \int_0^\infty F(\zeta, \tau - \zeta) d\zeta. \quad (6.1)$$

Stability analysis performed on this equation then allowed us to predict the stability threshold of one-dimensional detonations in the asymptotic limit under consideration. The theoretical findings were validated against a set of direct numerical simulations performed using the high-order spectral difference method, whose results came in accordance with the theory.

Future studies might focus on substantiating the theory for more realistic detonations far away from the asymptotic limits. In addition, an extension of the current work into the multi-dimensional case might be feasible by performing a similar study based on the work performed by Clavin and Williams in 2009 [86].

## 6.2 Deflagration-to-detonation transition of an elongated flame

In Chapter 5, we visited the problem of deflagration-to-detonation transition at the tip of an elongated laminar flame propagating in a very energetic mixture. A double-feedback mechanism was proposed for the DDT of such a flame, where the flame acceleration is driven by compressive heating of fresh gases and the back-flow of burnt gas into the flame tip. A one-dimensional piston model for the flow was constructed, and it was shown that a self-similar solution for the piston model exhibited a turning point described by the tangency solution of equation (5.29)

$$\Lambda^{-1}\mathcal{L}(M) = \mathcal{R}(M). \quad (6.2)$$

We demonstrated the divergence of the flame-tip acceleration at the turning point of the self-similar solution, which leads to the formation of a shock wave on the flame tip. This divergence is observed for a Mach number of the leading shock between 2 and 3, which is consistent with conditions of DDT observed in previous experimental studies [30, 78, 79].

Future studies might focus on the fully numerical resolution of the piston model, by considering a one-dimensional flame pushed by an accelerating piston in the burnt gas (Figure 5.3). Preliminary analysis performed by the team has revealed that a simple implementation of this problem would consistently lead to a rapid divergence of the piston velocity due to acoustic instabilities in the burnt gas. Such instabilities, which are not present in the physical problem, need to be mitigated in any future numerical study of the piston model.





# Bibliography

- [1] M Berthelot and P Vieille. L'oude explosive. *Ann. Chem. Phys*, 28(5):283–332, 1883.
- [2] John HS Lee. *The detonation phenomenon*. Cambridge University Press, Cambridge, 2008.
- [3] Paul Clavin and Geoff Searby. *Combustion waves and fronts in flows: flames, shocks, detonations, ablation fronts and explosion of stars*. Cambridge University Press, 2016.
- [4] Yuan Gao, Peng Dai, and Zheng Chen. Numerical studies on autoignition and detonation development from a hot spot in hydrogen/air mixtures. *Combustion Theory and Modelling*, 24(2):245–261, 2020.
- [5] Han Xu, Xiaodong Ni, Xiaojie Su, Bowen Xiao, Yongchen Luo, Feng Zhang, Chunsheng Weng, and Chunde Yao. Experimental and numerical investigation on effects of pre-ignition positions on knock intensity of hydrogen fuel. *International Journal of Hydrogen Energy*, 46(52):26631–26645, 2021.
- [6] Yuliang Qi, Xin He, Zhi Wang, Jianxin Wang, Huiqiang Zhang, and Yizhou Jiang. An experimental investigation of super knock combustion mode using a one-dimensional constant volume bomb. *international journal of hydrogen energy*, 40(5):2377–2385, 2015.
- [7] Z. Rui, W. Dan, and W. Jianping. Progress of continuously rotating detonation engines. *Chinese Journal of Aeronautics*, 29(1):15–29, 2016.
- [8] Yuho Uemura, A. Koichi Hayashi, Makoto Asahara, Nobuyuki Tsuboi, and Eisuke Yamada. Transverse wave generation mechanism in rotating detonation. *Proceedings of the Combustion Institute*, 34(2):1981 – 1989, 2013.
- [9] Zhenhua Pan, Baochun Fan, Xudong Zhang, Mingyue Gui, and Gang Dong. Wavelet pattern and self-sustained mechanism of gaseous detonation rotating in a coaxial cylinder. *Combustion and Flame*, 158(11):2220 – 2228, 2011.
- [10] Eric M. Braun, Frank K. Lu, Donald R. Wilson, and José A. Camberos. Airbreathing rotating detonation wave engine cycle analysis. *Aerospace Science and Technology*, 27(1):201 – 208, 2013.
- [11] Vijay Anand and Ephraim Gutmark. Rotating detonation combustors and their similarities to rocket instabilities. *Progress in Energy and Combustion Science*, 73:182 – 234, 2019.
- [12] Ken Matsuoka, Masaya Tanaka, Tomoyuki Noda, Akira Kawasaki, and Jiro Kasahara. Experimental investigation on a rotating detonation cycle with burned gas backflow. *Combustion and Flame*, 225:13–19, 2021.
- [13] CA COMAH. Buncefield: Why did it happen, 2011.
- [14] NASA Jet Propulsion Laboratory (JPL). Most detailed image of the crab nebula. <https://www.jpl.nasa.gov/images/pia03606-most-detailed-image-of-the-crab-nebula>, 2005.

- [15] F Ciaraldi-Schoolmann, IR Seitzzahl, and FK Röpke. A subgrid-scale model for deflagration-to-detonation transitions in type ia supernova explosion simulations-numerical implementation. *Astronomy & Astrophysics*, 559:A117, 2013.
- [16] Alexei Y Poludnenko, Jessica Chambers, Kareem Ahmed, Vadim N Gamezo, and Brian D Taylor. A unified mechanism for unconfined deflagration-to-detonation transition in terrestrial chemical systems and type ia supernovae. *Science*, 366(6465):eaau7365, 2019.
- [17] E Brooker, T Plewa, and D Fenn. Type Ia supernovae deflagration-to-detonation transition explosions powered by the Zel'dovich reactivity gradient mechanism. *Monthly Notices of the Royal Astronomical Society: Letters*, 501(1):L23–L27, 2021.
- [18] Jerome J Erpenbeck. Stability of steady-state equilibrium detonations. *Physics of Fluids*, 5(5):604–614, 1962.
- [19] Wildon Fickett and William W Wood. Flow calculations for pulsating one-dimensional detonations. *Physics of Fluids*, 9(5):903–916, 1966.
- [20] James A Fay. Stability of detonation waves at low pressures. In *Detonation and Two-Phase Flow*, pages 3–16. Elsevier, 1962.
- [21] Jerome J Erpenbeck. Stability of idealized one-reaction detonations. *Physics of Fluids*, 7(5):684–696, 1964.
- [22] Paul Clavin and Longting He. Stability and nonlinear dynamics of one-dimensional overdriven detonations in gases. *Journal of Fluid Mechanics*, 306:353–378, 1996.
- [23] Paul Clavin and Forman A Williams. Dynamics of planar gaseous detonations near Chapman-Jouguet conditions for small heat release. *Combustion Theory and Modelling*, 6(1):127–139, 2002.
- [24] Paul Clavin, Raúl Hernández-Sánchez, and Bruno Denet. Asymptotic analysis of the critical dynamics of spherical gaseous detonations. *Journal of Fluid Mechanics*, 915:A122, 2021.
- [25] Paul Clavin. Dynamics of combustion fronts in premixed gases: from flames to detonations. *Proc. Combust. Inst.*, 28(1):569–585, 2000.
- [26] Elaine S Oran. Understanding explosions – From catastrophic accidents to creation of the universe. *Proc. Combust. Inst.*, 35(1):1–35, 2015.
- [27] B Deshaies and G Joulin. Flame-speed sensitivity to temperature changes and the deflagration-to-detonation transition. *Combustion and flame*, 77(2):201–212, 1989.
- [28] G.B. Goodwin, R.W. Houim, and E.S. Oran. Shock transition to detonation in channels with obstacles. *Proc. Combust. Inst.*, 36(2):2717–2724, 2017.
- [29] Ya B Zeldovich. Regime classification of an exothermic reaction with nonuniform initial conditions. *Combustion and Flame*, 39(2):211–214, 1980.
- [30] MA Liberman, MF Ivanov, AD Kiverin, MS Kuznetsov, AA Chukalovsky, and TV Rakhimova. Deflagration-to-detonation transition in highly reactive combustible mixtures. *Acta Astronautica*, 67(7-8):688–701, 2010.
- [31] Jan S. Hesthaven and Tim Warburton. *Nodal Discontinuous Galerkin Methods: Algorithms, Analysis, and Applications*. Springer Science+Business Media, LLC, 2008.
- [32] Z.J. Wang, K. Fidkowski, R. Abgrall, F. Bassi, D. Caraeni, A. Cary, H. Deconinck, R. Hartmann, K. Hillewaert, H.T. Huynh, N. Kroll, G. May, P.O. Persson, B. van Leer, and M. Visbal. High-order CFD methods: current status and perspective. *Int. J. Numer. Meth. Fl.*, 72(8):811–845, 2013.

- [33] B. Cockburn, S. Hou, and C.W. Shu. The Runge-Kutta local projection discontinuous Galerkin finite element method for conservation laws IV: the multidimensional case. *Math. Comput.*, 54(190):545–581, 1990.
- [34] G. Karniadakis and S.J. Sherwin. *Spectral/hp element methods for CFD*. Oxford University Press, USA, 1999.
- [35] David A Kopriva and John H Koliass. A conservative staggered-grid chebyshev multidomain method for compressible flows. *Journal of Computational Physics*, 125(1):244–261, 1996.
- [36] Y. Sun, Z.J. Wang, and Y. Liu. High-order multidomain spectral difference method for the Navier-Stokes equations on unstructured hexahedral grids. *Commun. Comput. Phys.*, 2(2):310–333, 2007.
- [37] Antony Jameson. A proof of the stability of the spectral difference method for all orders of accuracy. *Journal of Scientific Computing*, 45(1-3):348–358, 2010.
- [38] H.T. Huynh. A flux reconstruction approach to high-order schemes including discontinuous Galerkin methods. *AIAA P.*, 2007-4079:1–42, 2007.
- [39] H.T. Huynh. A reconstruction approach to high-order schemes including discontinuous Galerkin for diffusion. *AIAA P.*, 2009-403:1–34, 2009.
- [40] P.E. Vincent, P. Castonguay, and A. Jameson. A new class of high-order energy stable flux reconstruction schemes. *J. Sci. Comput.*, 47(1):1–23, 2010.
- [41] Forman A Williams. *Combustion theory*. CRC Press, 2018.
- [42] Lev Davidovich Landau and Evgenii Mikhailovich Lifshitz. *Fluid Mechanics: Landau and Lifshitz: Course of Theoretical Physics*, volume 6. Elsevier, 2013.
- [43] Roger Prud’Homme. *Flows and Chemical Reactions*. John Wiley & Sons, 2013.
- [44] VA Mikhelson. On the normal ignition velocity of explosive gaseous mixtures. *Scientific Transactions of Imperial Moscow University on Mathematics and Physics*, 10:1–93, 1893.
- [45] David Leonard Chapman. VI. on the rate of explosion in gases. *The London, Edinburgh, and Dublin Philosophical Magazine and Journal of Science*, 47(284):90–104, 1899.
- [46] Emile Jouguet. Remarques sur la propagation des percussions dans les gaz. *CR Acad. Sci. Paris*, 138:1685–1688, 1904.
- [47] John Von Neuman. Theory of detonation waves. Technical report, Institute for Advanced Study Princeton NJ, 1942.
- [48] Gary J Sharpe and SAEG Falle. One-dimensional nonlinear stability of pathological detonations. *Journal of Fluid Mechanics*, 414:339–366, 2000.
- [49] JP Dionne, R Duquette, A Yoshinaka, and JHS Lee. Pathological detonations in  $H_2-Cl_2$ . *Combustion science and technology*, 158(1):5–14, 2000.
- [50] Ya B Zeldovich and DA Frank-Kamenetskii. Thermal theory of flame propagation. *Zh. Fiz. Khim.*, 12(1):100–105, 1938.
- [51] Yuzhi Sun, Zhi Jian Wang, and Yen Liu. High-order multidomain spectral difference method for the navier-stokes equations. In *44th AIAA Aerospace Sciences Meeting and Exhibit*, page 301, 2006.
- [52] Y. Sun, Z.J. Wang, and Y. Liu. High-order multidomain spectral difference method for the Navier-Stokes equations on unstructured hexahedral grids. *Communication in Computational Physics*, 2(2):310–333, 2007.

- [53] Philip L Roe. Approximate riemann solvers, parameter vectors, and difference schemes. *Journal of Computational Physics*, 43(2):357–372, 1981.
- [54] Eleuterio F Toro. *Riemann Solvers and Numerical Methods for Fluid Dynamics: A Practical Introduction*. Springer Science & Business Media, 2009.
- [55] Raymond J Spiteri and Steven J Ruuth. A new class of optimal high-order strong-stability-preserving time discretization methods. *SIAM Journal on Numerical Analysis*, 40(2):469–491, 2002.
- [56] Niccolò Tonicello, Guido Lodato, and Luc Vervisch. Entropy preserving low dissipative shock capturing with wave-characteristic based sensor for high-order methods. *Computers & Fluids*, 197:104357, 2020.
- [57] Guido Lodato. Characteristic modal shock detection for discontinuous finite element methods. *Computers & Fluids*, 179:309–333, 2019. Corrected in: *Computers & Fluids*, 193:104245 (2019).
- [58] Per-Olof Persson. Shock capturing for high-order discontinuous galerkin simulation of transient flow problems. In *21st AIAA computational fluid dynamics conference*, page 3061, 2013.
- [59] Xiangxiong Zhang and Chi-Wang Shu. On positivity-preserving high order discontinuous galerkin schemes for compressible euler equations on rectangular meshes. *Journal of Computational Physics*, 229(23):8918–8934, 2010.
- [60] E. S. Oran. Understanding explosions – from catastrophic accidents to creation of the universe. *Proceedings of the Combustion Institute*, 35(1):1–35, 2015.
- [61] Stephen W. Grib, Christopher A. Fugger, Paul S. Hsu, Naibo Jiang, Sukesh Roy, and S. Alexander Schumaker. Two-dimensional temperature in a detonation channel using two-color OH planar laser-induced fluorescence thermometry. *Combustion and Flame*, 228:259–276, 2021.
- [62] Praveen Honhar, Carolyn R. Kaplan, Ryan W. Houim, and Elaine S. Oran. Role of reactivity gradients in the survival, decay and reignition of methane-air detonations in large channels. *Combustion and Flame*, 222:152–169, 2020.
- [63] J. Melguizo-Gavilanes, V. Rodriguez, P. Vidal, and R. Zitoun. Dynamics of detonation transmission and propagation in a curved chamber: a numerical and experimental analysis. *Combustion and Flame*, 223:460–473, 2021.
- [64] Colin A.Z. Towery, Alexei Y. Poludnenko, and Peter E. Hamlington. Detonation initiation by compressible turbulence thermodynamic fluctuations. *Combustion and Flame*, 213:172–183, 2020.
- [65] J. C. Schulz, K. C. Gottiparthi, and S. Menon. Ionization in gaseous detonation waves. *Shock Waves*, 22:579–590, 2012.
- [66] Youhi Morii, Ajit K. Dubey, Hisashi Nakamura, and Kaoru Maruta. Two-dimensional laboratory-scale dns for knocking experiment using n-heptane at engine-like condition. *Combustion and Flame*, 223:330–336, 2021.
- [67] Sh Taki and T Fujiwara. Numerical analysis of two-dimensional nonsteady detonations. *Aiaa Journal*, 16(1):73–77, 1978.
- [68] HD Ng, MI Radulescu, AJ Higgins, N Nikiforakis, and JHS Lee. Numerical investigation of the instability for one-dimensional Chapman–Jouguet detonations with chain-branching kinetics. *Combustion Theory and Modelling*, 9(3):385–401, 2005.

- [69] Paul Clavin. Nonlinear dynamics of shock and detonation waves in gases. *Combustion Science and Technology*, 189(5):747–775, 2017.
- [70] Paul Clavin and Bruno Denet. Analytical study of the direct initiation of gaseous detonations for small heat release. *Journal of Fluid Mechanics*, 897:A30, 2020.
- [71] P Hwang, RP Fedkiw, B Merriman, TD Aslam, AR Karagozian, and SJ Osher. Numerical resolution of pulsating detonation waves. *Combustion Theory and Modelling*, 4(3):217, 2000.
- [72] JW Meyer, PA Urtiew, and AK Oppenheim. On the inadequacy of gasdynamic processes for triggering the transition to detonation. *Combustion and Flame*, 14(1):13–20, 1970.
- [73] Kirill Ivanovich Shchelkin and Ya K Troshin. *Gasdynamics of combustion*, volume 231. National Aeronautics and Space Administration, 1964.
- [74] MF Ivanov, AD Kiverin, and MA Liberman. Hydrogen-oxygen flame acceleration and transition to detonation in channels with no-slip walls for a detailed chemical reaction model. *Physical Review E*, 83(5):056313, 2011.
- [75] Ryan W Houim, Alp Ozgen, and Elaine S Oran. The role of spontaneous waves in the deflagration-to-detonation transition in submillimetre channels. *Combustion Theory and Modelling*, 20(6):1068–1087, 2016.
- [76] Wenhui Han, Yang Gao, and Chung K Law. Flame acceleration and deflagration-to-detonation transition in micro-and macro-channels: An integrated mechanistic study. *Combustion and Flame*, 176:285–298, 2017.
- [77] Ming-hsun Wu, MP Burke, S Ff Son, and RA Yetter. Flame acceleration and the transition to detonation of stoichiometric ethylene/oxygen in microscale tubes. *Proceedings of the Combustion Institute*, 31(2):2429–2436, 2007.
- [78] M Kuznetsov, M Liberman, and I Matsukov. Experimental study of the preheat zone formation and deflagration to detonation transition. *Combustion science and technology*, 182(11-12):1628–1644, 2010.
- [79] Ming-Hsun Wu and Chan-Yu Wang. Reaction propagation modes in millimeter-scale tubes for ethylene/oxygen mixtures. *Proceedings of the Combustion Institute*, 33(2):2287–2293, 2011.
- [80] Bogdan Ponizy, Alain Claverie, and Bernard Veysseyre. Tulip flame-the mechanism of flame front inversion. *Combustion and flame*, 161(12):3051–3062, 2014.
- [81] Vitaly Bychkov, Arkady Petchenko, V'yacheslav Akkerman, and Lars-Erik Eriksson. Theory and modeling of accelerating flames in tubes. *Physical Review E*, 72(4):046307, 2005.
- [82] Damir M Valiev, Vitaly Bychkov, V'yacheslav Akkerman, and Lars-Erik Eriksson. Different stages of flame acceleration from slow burning to Chapman-Jouguet deflagration. *Physical Review E*, 80(3):036317, 2009.
- [83] Christophe Clanet and Geoffrey Searby. On the “tulip flame” phenomenon. *Combustion and flame*, 105(1-2):225–238, 1996.
- [84] Paul Clavin, Pierre Pelcé, and Longting He. One-dimensional vibratory instability of planar flames propagating in tubes. *Journal of Fluid Mechanics*, 216:299–322, 1990.
- [85] Richard Courant and Kurt Otto Friedrichs. *Supersonic flow and shock waves*, volume 21. Springer Science & Business Media, 1999.

- 
- [86] Paul Clavin and Forman A Williams. Multidimensional stability analysis of gaseous detonations near Chapman–Jouguet conditions for small heat release. *Journal of fluid mechanics*, 624:125–150, 2009.



# French summary

## Résumé du chapitre 1

Ce chapitre introductif présente la motivation de l'étude et ses principaux objectifs. Il présente également les deux problèmes abordés dans l'étude: la stabilité de la détonation et la transition déflagration-détonation, et nous discutons des méthodes théoriques et numériques utilisées.

## Résumé du chapitre 2

Ce chapitre fournit une brève introduction à la théorie des ondes de détonation et de déflagration. Nous commençons par présenter une description phénoménologique des détonations et déflagrations, puis nous discutons la théorie de la dynamique gazeuse des détonations et déflagrations, et enfin nous présentons la théorie de la flamme ZFK.

## Résumé du chapitre 3

Ce chapitre présente la méthode de différence spectrale d'ordre élevé utilisée dans les simulations numériques effectuées tout au long de cette étude. L'implémentation est présentée dans une dimension spatiale, et des modifications de la méthode pour les simulations dans des référentiels non inertiels sont discutées.

## Résumé du chapitre 4

Ce chapitre présente l'étude de la dynamique unidimensionnelle des détonations. Une théorie asymptotique est développée dans laquelle l'instabilité de la vitesse du choc est liée à l'effet des ondes acoustiques arrivant au choc depuis la zone de réaction. La théorie est ensuite validée à l'aide d'un DNS d'ordre élevé.

## Résumé du chapitre 5

Ce chapitre présente un nouveau mécanisme DDT pour les flammes laminaires allongées. Nous montrons qu'un mécanisme à double rétroaction pour l'accélération de la flamme, dans lequel la flamme est accélérée par le reflux de gaz brûlés et par le chauffage par compression de gaz frais conduit à un moment donné à un emballement de l'accélération de la flamme et à la formation d'un choc sur la flamme. Ces résultats s'avèrent cohérents avec les expériences et les simulations disponibles dans la littérature.

## Résumé des perspectives

Enfin, un résumé des principaux résultats et des perspectives générales sont présentés. Une extension possible de l'analyse de la stabilité de la détonation au cas multidimensionnel est suggérée, ainsi que des pistes futures possibles pour l'étude numérique du problème du DDT.